Politecnico di Torino

Master's Degree Programme in Energy and Nuclear Engineering

Academic Year 2025/2026

Graduation Session – July 2026

Techno-Economic Assessment of Building-Integrated Bifacial Photovoltaic Systems in Nordic Climatic Conditions

Supervisors:

Prof. Vittorio Verda

Prof. Andrea Ferrantelli

Co-supervisor:

Dr. Amin Khodakaram-Tafti

Candidate:

Federico Antonio D'Oria

Abstract

The decarbonisation of the building sector requires the large-scale deployment of renewable energy technologies that can be integrated into the built environment. Among these, Building-Integrated Photovoltaics (BIPV) offer a promising solution by generating electricity while utilising existing building surfaces without additional land use. In Northern European countries, where rooftop areas may be limited and solar irradiation differs significantly from lower latitudes, facade-integrated photovoltaics have gained increasing attention. In this context, bifacial photovoltaic technology can enhance energy production by harvesting solar radiation on both sides of the module. This thesis presents a techno-economic framework for assessing building-integrated bifacial photovoltaic systems installed on south-facing vertical facades in Helsinki, Finland. The methodology combines optical, electrical, thermal and economic analyses to evaluate the performance and feasibility of bifacial facade-integrated photovoltaics under Nordic climatic conditions. The work is structured into three phases. First, an optical-electrical model is developed to calculate the irradiance incident on both sides of bifacial glass-glass Tunnel Oxide Passivated Contact (TOPCon) modules installed at different heights along a facade. The model uses measured meteorological data from the FMI Helsinki Kumpula station for the year 2021 and accounts for urban integration effects. A view-factor approach is adopted to quantify rear-side irradiance contributions from the sky, ground and building wall. The resulting irradiance values are used to estimate electrical power output and bifacial gain under different seasonal conditions. Second, a Computational Fluid Dynamics (CFD) model is developed in ANSYS Fluent to investigate the thermal behaviour of the BIPV system. Particular attention is given to the naturally ventilated air gap between the photovoltaic modules and the building wall, whose geometry affects module temperature and electrical performance. Conjugate heat transfer simulations are performed for different air-gap thicknesses using four representative days selected to capture seasonal variability. The simulations provide detailed information on airflow and heat transfer mechanisms, enabling the determination of convective heat transfer coefficients that are used to refine the thermal boundary conditions of the optical-electrical model. Finally, a techno-economic analysis is conducted for two case studies: the TUAS building at Aalto University in Espoo and a residential apartment building. The assessment follows the extra-cost methodology proposed by Corti et al. (2024), complemented by Net Present Value and sensitivity analyses. Hourly electricity consumption profiles are used to evaluate self-consumption and the economic benefits of on-site generation. A comparison between bifacial and monofacial configurations is also performed to assess the economic value of bifaciality under nordic conditions. Results are evaluated in terms of payback period, internal rate of return, net present value and levelised cost of energy. Overall, this work pro-

vides an integrated methodology combining optical, thermal and economic modelling for bifacial BIPV facade systems, offering a replicable framework for the design and assessment of facade-integrated photovoltaics in Nordic climates. The techno-economic analysis of Chapter 4 was developed by Sara Monticelli as part of this joint thesis work.

Contents

List of Tables

List of Figures

Chapter 1

Literature Review and Research Context

1.1 Global Energy Transition and the Role of Solar Photovoltaics

The global energy landscape is currently at a critical turning point. The accelerating effects of climate change, combined with growing energy demand driven by population growth, urbanization, and economic development, have placed the transition towards clean and sustainable energy systems at the top of the international political agenda. The growing awareness of the environmental consequences of fossil fuel dependence has led to a progressive shift in energy policies and technological development towards more sustainable and low-carbon energy systems.

1.1.1 Decarbonization and Building-Sector Targets

The global energy system is undergoing an unprecedented transformation driven by the urgent need to limit climate change and achieve net-zero greenhouse gas emissions by mid-century. Over the past decades, the increasing concentration of atmospheric CO_2 and other greenhouse gases has been identified as the primary cause of global warming, leading to significant environmental, economic, and social consequences. Despite recent signs of deceleration, total energy-related CO_2 emissions reached a new high of nearly 38.4 billion tonnes in 2025, approximately 5% above 2019 levels, coinciding with record atmospheric CO_2 concentrations of about 427 parts per million , roughly 50% above pre-industrial levels [5].

In this context, international agreements and policy frameworks have played a crucial role in defining decarbonization pathways. The Paris Agreement (2015) established the long-term goal of limiting global average temperature increase to well below 2°C above pre-industrial levels, with efforts to limit it to 1.5°C. At the European level, the European Green Deal and the Fit for 55 package translate this ambition into concrete legislative measures, setting a binding target of reducing net greenhouse gas emissions by at least 55% below 1990 levels by 2030, with the long-term vision of achieving climate neutrality by 2050 [2]. These strategies highlight the need for a systemic transformation of the energy sector, requiring not only the deployment of clean energy technologies but also the rethinking of energy consumption patterns and infrastructure.

Among the different sectors contributing to global emissions, the building sector plays a central role. Buildings are responsible for approximately 30% of global final energy consumption and have contributed nearly 20% of the growth in total energy demand since 2019 [4]. In the European Union, buildings account for 40% of total energy consumption and 35% of greenhouse gas emissions, making the building sector a central target of climate policy [10]. Improving the energy performance of buildings has therefore become a key priority in achieving climate targets , involving not only the reduction of energy demand through efficient design and materials, but also the integration of on-site renewable energy generation systems. In line with this, the European Green Deal sets an ambitious target to renovate 35 million buildings across the EU by 2030, highlighting the strategic importance of the building sector in the decarbonization process [2].

At the building level, the recast Energy Performance of Buildings Directive (EPBD, EU/2024/1275), which entered into force on 28 May 2024, establishes zero-emission buildings as the new standard for all new construction [7]. The revised directive requires all new buildings to be designed to optimise their solar energy generation potential, and mandates the deployment of solar energy installations on new public and non-residential buildings with a useful floor area larger than 250 m^2 by 31 December 2026, and on all new residential buildings by 31 December 2029 [7]. Furthermore, Member States must reduce the average primary energy use of residential buildings by 16% by 2030 and by 20/22% by 2035. These regulatory milestones create a strong and binding framework that places building-integrated renewable energy systems at the centre of the European decarbonization strategy.

1.1.2 Role of Solar PV in the Energy Transition

The transition towards renewable energy sources has gained significant momentum in recent years. Among the various renewable energy sources, solar energy stands out due to its abundance, wide availability, and long-term sustainability. The amount of solar radiation reaching the Earth's surface is several orders of magnitude higher than current global energy demand, making it a particularly attractive resource for large-scale energy production. This potential, combined with the modularity and scalability of photovoltaic technology, has positioned solar PV as a cornerstone of the global energy transition.

Photovoltaic (PV) technology, which enables the direct conversion of solar radiation into electricity, has emerged as one of the most promising and rapidly growing renewable energy technologies. Continuous improvements in materials, manufacturing processes, and system design have led to significant reductions in costs and increases in efficiency, facilitating the widespread adoption of PV systems. Solar PV capacity additions surpassed 600 GW for the first time in 2025, with cumulative solar PV capacity reaching around 2,800 GW , making it the technology with the largest installed capacity globally [3]. By 2024, solar PV accounted for 7% of global electricity generation, up from 5.4% in 2023, and renewables as a whole supplied 32% of the world's electricity for the first time [5]. Thirty countries installed over 1 GW of solar PV in a single year in 2025, almost twice as many as in 2020, confirming the transition of photovoltaics from a niche technology to a mainstream component of modern energy systems [3].

The rapid cost reduction of solar PV is one of the most remarkable technological achievements of the past decade. According to IRENA, average utility-scale solar PV installed costs have fallen by around 85/90% since 2010, making solar the cheapest source of new electricity generation in most parts of the world [8]. Looking ahead, global renewable capacity is expected to grow by 2.7 times by 2030, with annual additions reaching almost 940 GW, 70% more than the record levels recorded in 2023 [3]. In the IEA's Net Zero Emissions by 2050 Scenario, solar PV becomes the single largest source of electricity generation globally before 2030, requiring annual average generation growth of approximately 28% during 2024-2030 to reach 9,200 TWh [6]. This cost trajectory, combined with strong policy support, has stimulated the growth of distributed PV applications , including residential, commercial, and building-integrated systems , which are expected to represent almost 40% of the overall PV expansion to 2030 [3].

A key advantage of photovoltaic technology lies in its flexibility of deployment. PV systems can be installed at different scales, ranging from large utility-scale power plants to small distributed systems integrated within the built environment. This versatility enables a shift from centralised energy production towards more decentralised energy systems, where energy is generated closer to the point of consumption , contributing to reduced transmission losses, increased energy resilience, and greater energy independence.

1.1.3 Urban Constraints and the Need for Building-Integrated Solutions

Despite the remarkable growth of utility-scale solar installations, the increasing urbanisation of the global population poses a fundamental challenge: land availability for large-scale ground-mounted PV systems is severely constrained in dense urban environments. As of 2023, more than 56% of the world's population lives in urban areas, a share projected to reach 68% by 2050 [11]. In densely built areas, these constraints are further exacerbated by shading from surrounding buildings, complex urban geometries, and the scarcity of available open land.

At the same time, buildings represent an enormous untapped surface area for solar energy harvesting: rooftops, facades, windows, and other building envelope elements offer a distributed generation potential that could significantly contribute to urban energy demand without requiring additional land. Rather than considering buildings solely as energy consumers, recent research and design approaches increasingly view them as active components of the energy system, capable of producing energy while fulfilling their primary architectural and functional roles.

Building-Integrated Photovoltaics (BIPV) have emerged as a key technology to exploit this potential, by replacing conventional building envelope elements , such as cladding panels, glazing, or roofing materials , with photovoltaic modules that simultaneously serve structural and energy-generating functions. Unlike Building-Applied Photovoltaics (BAPV), where PV modules are added on top of existing building elements, BIPV systems are designed as integral components of the building envelope from the outset, offering additional benefits in terms of aesthetics, thermal insulation, and multifunctionality. The regulatory framework reinforces this direction: the recast EPBD explicitly requires new buildings to be "solar-ready", meaning they must be architecturally designed to accommodate PV installations from the design stage, without requiring costly structural interventions at a later time [7].

From a technological perspective, the integration of PV systems into buildings requires careful consideration of multiple factors, including orientation, inclination, shading conditions, and interaction with surrounding surfaces. Furthermore, the performance of photovoltaic systems is strongly influenced by thermal effects: the operating temperature of PV modules directly affects their efficiency, and this is particularly relevant in building-integrated configurations where heat dissipation mechanisms may differ significantly from conventional installations. The interaction between solar radiation, building components, and airflow around the modules introduces additional complexity that must be taken into account in the design and analysis of these systems [19].

The combination of falling PV module costs, tightening building energy regulations, and the growing demand for multifunctional building envelopes is creating a rapidly expanding market for BIPV solutions. Within this context, bifacial PV modules , capable of harvesting solar irradiance from both the front and rear surfaces , represent a particularly promising technology for building facade applications, where reflected radiation from surrounding surfaces and the building wall itself can significantly enhance the energy yield compared to conventional monofacial modules [14]. The present thesis focuses on this specific configuration: a building-integrated bifacial PV facade in the Nordic climate of Helsinki, Finland, where the combination of high-latitude solar conditions, seasonal snow cover, and the need for thermally efficient ventilated facades creates both unique challenges and significant research opportunities, as discussed in the following sections.

In summary, the global energy transition requires a significant increase in the deployment of renewable energy technologies, with solar photovoltaics playing a central role due to their versatility, scalability, and rapidly declining costs. At the same time, the constraints associated with urban environments call for innovative solutions that enable the effective integration of PV systems into buildings. This context provides the foundation for the development of building-integrated bifacial photovoltaic technologies, which will be discussed in detail in the following sections.

1.2 Building-Integrated Photovoltaics (BIPV)

Building-Integrated Photovoltaics (BIPV) represent a paradigm shift in the way buildings interact with the energy system. Rather than treating solar panels as external additions to completed structures, BIPV systems embed photovoltaic functionality directly into the building envelope, transforming surfaces that would otherwise be passive construction elements into active generators of renewable electricity. This section provides a structured overview of the BIPV concept, its main configurations, its architectural and functional benefits, and the current status of its deployment, including the barriers that still limit its widespread adoption.

1.2.1 Definition of BIPV and Distinction from BAPV

The term Building-Integrated Photovoltaics refers to photovoltaic systems in which the PV modules are incorporated into the building envelope as a functional construction element, replacing conventional materials such as roofing tiles, façade cladding, glazing, or shading devices [23]. This definition distinguishes BIPV from Building-Applied Photovoltaics (BAPV), in which PV modules are mounted onto existing structures as an additional layer without substituting any primary building material [24]. The distinction is not merely terminological: it has significant implications for system design, cost accounting, regulatory compliance, and architectural integration.

In a BAPV system, the photovoltaic array is structurally and functionally independent of the building envelope – it can be removed or replaced without affecting the building's weatherproofing, structural integrity, or thermal performance. In a BIPV system, by contrast, the photovoltaic module fulfils a dual role: it simultaneously acts as a construction product and an electricity generator [26]. This dual nature means that the cost of the PV component must be assessed net of the cost of the conventional material it replaces, making the economic comparison with standard PV more favourable than often perceived [23].

The first documented installation of a building-integrated photovoltaic system was realised in Aachen, Germany, in 1991, where PV elements were integrated into a curtain wall façade [23]. Since then, BIPV technology has evolved considerably, encompassing a wide variety of configurations, materials, and integration strategies, from opaque crystalline silicon modules on rooftops and façades to semi-transparent thin-film glazing and coloured panels designed to match architectural requirements [25].

1.2.2 Main BIPV Configurations

BIPV systems can be classified according to the building element they are integrated into, the orientation and inclination of the surface, and the degree of transparency of the module. The main configurations investigated in the literature are summarised below.

Roof-integrated systems.

Rooftop integration is the most widespread BIPV configuration, accounting for approximately 66.9% of the global BIPV market by revenue in 2023 [27]. In these systems, PV modules replace conventional roofing materials such as tiles or metal sheeting. The south-facing roof orientation, common in the northern hemisphere, is generally optimal for maximising annual solar irradiance on the front surface. Roof-integrated systems are typically monofacial, since the rear surface faces the roof structure and receives no significant irradiance.

Façade systems.

Vertical façade integration represents one of the most promising and technically challenging BIPV configurations. Façade panels are exposed to a lower annual solar irradiance than roof systems due to their vertical orientation, but they offer significant architectural integration potential and, in the case of bifacial modules, can harvest reflected radiation from the ground and surrounding surfaces [19]. Ventilated façade configurations, in which an air cavity is maintained between the PV modules and the building wall, are of particular interest: the airflow within the cavity enhances convective cooling of the modules, improving their electrical efficiency and providing additional thermal benefits to the building . Double Skin Façades (DSF) with integrated PV are a further evolution of this concept, combining solar generation with dynamic solar shading and natural ventilation[28].

Glazing and semi-transparent systems.

Semi-transparent BIPV modules integrated into windows, skylights, or curtain walls allow daylight to pass through while generating electricity. These systems involve a trade-off between transparency, aesthetics, and electrical output: increasing the packing factor of solar cells improves energy yield but reduces light transmittance and visual comfort. Recent advances in thin-film technologies and perovskite solar cells are expanding the range of achievable colours and transparency levels, opening new possibilities for architectural integration [13].

Shading and solar control systems.

BIPV modules can also be deployed as external shading devices – horizontal brise-soleils, vertical fins, or adjustable louvres – that simultaneously reduce solar heat gain inside the building and generate electricity. This configuration is particularly effective in warm climates, where solar shading is a primary architectural requirement, and in building retrofits where the existing façade cannot easily accommodate integrated modules [24].

Other configurations.

Additional BIPV configurations include balcony railings, car park canopies, noise barriers, and agrivoltaic installations. The diversity of available configurations reflects the versatility of BIPV technology and its ability to adapt to a wide range of architectural contexts and functional requirements [25].

1.2.3 Architectural and Functional Benefits

Beyond electricity generation, BIPV systems offer a range of architectural and functional benefits that distinguish them from conventional PV installations and contribute to their value in the built environment.

Material substitution and cost offset.

Since BIPV modules replace conventional building materials, part of their cost can be attributed to the building envelope function rather than the energy system. This material substitution effect is particularly significant for high-value applications such as glazing or premium cladding, where the cost differential between the BIPV module and the replaced conventional material may be small [23].

Thermal insulation and energy performance.

BIPV façade systems, and ventilated BIPV façades in particular, contribute to the thermal performance of the building envelope by acting as a second skin that reduces the direct solar load on the primary wall. Studies have shown that BIPV systems can achieve energy savings of up to 37% in building operational energy when properly designed and oriented [26]. In addition, the air cavity in ventilated façades promotes natural convection, which can be exploited for passive cooling in summer or pre-heating of ventilation air in winter [28].

Aesthetic integration and architectural identity.

One of the key advantages of BIPV over BAPV is the possibility of seamlessly integrating PV functionality into the architectural design of a building, without the visual impact of externally mounted frames and panels. The availability of modules in different colours, shapes, transparency levels, and surface textures enables architects to use BIPV as a design element that contributes to the visual identity of the building [24]. This aesthetic dimension is increasingly recognised as a critical factor in public acceptance and architectural adoption of solar technology in urban environments.

Noise reduction and weather protection.

BIPV façade panels provide additional weather protection by shielding the primary building wall from wind-driven rain, temperature cycling, and UV radiation. The outer glass layer of glass-glass bifacial modules, which are commonly used in BIPV façade applications, also provides a degree of acoustic insulation, reducing noise transmission from the exterior [13].

1.2.4 Current Status and Barriers of BIPV Deployment

Despite its considerable technical and architectural potential, BIPV remains a niche segment within the broader PV market. According to Constantinou et al. [24], BIPV currently accounts for only approximately 1% of total global PV installations – a share that is disproportionately small given the theoretical potential of building surfaces for solar energy harvesting. The global BIPV market was valued at approximately USD 23.7 billion in 2023 and is projected to grow at a compound annual growth rate (CAGR) of approximately 21% to reach USD 89.8 billion by 2030, driven by tightening building energy codes, falling PV module costs, and increasing demand for net-zero energy buildings [27].

A scientometric analysis of 467 BIPV-related studies published between 2019 and 2023 by Shu et al. [25] confirms that research interest in BIPV has grown significantly in recent years, with key themes including energy performance, thermal behaviour, economic analysis, and architectural integration. However, the same analysis highlights that translation from research output to market deployment remains limited, pointing to a range of persistent barriers.

Economic barriers.

The most frequently cited barrier to BIPV adoption is the higher upfront cost compared to both conventional building materials and standard BAPV systems [23]. Initial installation costs for BIPV systems can be up to 20% higher than equivalent conventional construction methods [23]. Long payback periods, uncertain energy price trajectories, and limited awareness of the material substitution cost offset further discourage investment. The BIPV Market Development analysis by Saretta et al. [26] identifies cost as the primary barrier in all six countries studied, noting that BAPV is often preferred by building owners precisely because of its lower upfront investment.

Technical and standardisation barriers.

BIPV systems face a range of technical challenges related to their dual nature as both a photovoltaic and a building product. These include the need to meet simultaneously the electrical performance requirements of PV standards and the structural, thermal, and fire safety requirements of building product standards [26]. The lack of unified international standards for BIPV products and the absence of a harmonised testing and certification framework create uncertainty for manufacturers, architects, and clients alike. Additionally, the integration of PV into building envelopes introduces thermal management challenges: reduced airflow compared to free-standing installations leads to higher operating temperatures and lower electrical efficiency [24].

Market and knowledge barriers.

A fundamental challenge lies in the interdisciplinary nature of BIPV, which requires close collaboration between the photovoltaic industry and the construction sector –

two fields with different languages, design processes, and regulatory environments [26]. Architects often have limited knowledge of PV technology, while PV engineers may lack expertise in building design and construction practice [25]. This knowledge gap is compounded by insufficient product availability, limited databases of BIPV case studies, and a lack of dedicated design software tools that would allow architects to assess the performance and cost of BIPV options at the early design stage [23].

Regulatory and policy barriers.

While the recast EPBD (2024) and the European Green Deal provide a strong policy impetus for BIPV deployment, the implementation of specific financial incentives and regulatory frameworks for BIPV – as distinct from conventional rooftop PV – remains inconsistent across EU Member States [26]. Feed-in tariff schemes, building energy performance certificates, and green building rating systems do not always fully recognise the dual value of BIPV as both an energy system and a building component [23].

Notwithstanding these barriers, the outlook for BIPV is positive. The combination of falling module costs, increasingly stringent building energy regulations, and growing architectural demand for sustainable and multifunctional building envelopes is expected to accelerate market growth over the coming decade. The integration of bifacial PV modules into façade systems represents a particularly promising direction, as it adds a further dimension of energy harvesting – from the rear surface – that is uniquely suited to the built environment context, as discussed in the following sections.

1.3 Bifacial photovoltaic technology

Bifacial photovoltaic (bPV) technology represents a significant advancement over conventional monofacial PV systems, enabling the conversion of solar irradiance from both the front and rear surfaces of the module. Unlike traditional monofacial modules, which are limited to front-side radiation, bifacial modules are designed to exploit additional reflected and diffuse radiation from the surrounding environment, resulting in an increased overall energy yield. This dual-sided energy harvesting capability has attracted growing attention in recent years, positioning bifacial PV as a promising technology for enhancing the efficiency and economic performance of solar energy systems [1].

1.3.1 Operating principle of bifacial PV

The operating principle of bifacial photovoltaic modules is based on a modified cell structure that allows light to be absorbed from both sides. In conventional monofacial cells, the rear surface is typically covered by a continuous metallic electrode, preventing light transmission. In contrast, bifacial cells employ a partially transparent or passivated rear structure, enabling incident radiation to reach the active semiconductor region from the back side.

The total irradiance received by a bifacial module can be decomposed into three main components: direct irradiance, diffuse sky irradiance, and reflected irradiance (albedo). While the front surface primarily captures direct and diffuse radiation, the rear surface mainly receives reflected radiation from the ground and surrounding surfaces, as well as a portion of diffuse radiation. The interaction between these components leads to an additional generation of electron-hole pairs on the rear side, increasing the total photocurrent and, consequently, the power output of the module [1].

This characteristic makes bifacial systems particularly sensitive to the surrounding environment. Unlike monofacial modules, whose performance depends mainly on solar geometry, bifacial modules are strongly influenced by the optical properties of nearby surfaces, geometrical configuration, and installation conditions.

1.3.2 Main cell technologies

Bifacial photovoltaic technology can be implemented using a variety of cell architectures, each characterised by specific design features aimed at enabling rear-side light absorption and improving overall efficiency. The key difference with respect to monofacial technologies lies in the rear-side structure, which must allow light transmission and minimise recombination losses. The main bifacial cell technologies are summarised below, following the classification reported in the literature [1].

- **PERC (Passivated Emitter Rear Contact):** PERC cells are based on a partially passivated rear surface with local openings that allow charge collection. In bifacial configurations, the rear layer is modified to allow partial light transmission, enabling rear-side absorption. The passivation layer reduces recombination losses, improving efficiency compared to conventional cells.
- **PERL (Passivated Emitter Rear Locally Diffused):** PERL cells improve upon PERC by introducing a more advanced rear surface passivation and locally diffused regions. This reduces carrier recombination at the rear interface and enhances both voltage and overall efficiency, making them suitable for high-performance bifacial applications.
- **PERT (Passivated Emitter Rear Totally Diffused):** In PERT cells, the rear surface is fully diffused rather than locally processed. This configuration provides improved electrical conductivity and lower recombination losses, resulting in higher open-circuit voltage and enhanced bifacial response.

- **IBC (Interdigitated Back Contact):** IBC cells feature all electrical contacts located on the rear surface in an interdigitated pattern. This eliminates front-side shading losses and maximises light absorption. The absence of front metallisation, combined with advanced light-trapping structures, makes IBC cells particularly effective for high-efficiency bifacial operation.
- **HIT (Heterojunction with Intrinsic Thin Layer):** HIT cells combine crystalline silicon wafers with thin amorphous silicon layers. The heterojunction structure provides excellent surface passivation, leading to high efficiency and strong bifacial performance. These cells are known for their high bifaciality factor and good temperature behaviour.
- **TOPCon (Tunnel Oxide Passivated Contact):** TOPCon technology uses an ultra-thin oxide layer combined with a doped polysilicon contact to achieve carrier selectivity. This structure reduces recombination and improves charge transport, making it one of the most promising technologies for next-generation high-efficiency bifacial modules.
- **CIGS (Copper Indium Gallium Selenide):** CIGS thin-film cells are based on a semiconductor absorber layer that allows flexible and lightweight module designs. Their structure enables bifacial operation with relatively simple manufacturing processes. These cells are particularly attractive for building-integrated applications, although their large-scale deployment is limited by material availability and cost.

Recent developments in bifacial photovoltaic technology have focused on improving both material properties and device architectures in order to enhance light utilisation from a broader spectral range. In particular, advances in passivation techniques and novel cell structures have contributed to increasing conversion efficiency and bifaciality.

Emerging technologies, such as perovskite-based solar cells, show significant potential due to their high absorption coefficients and compatibility with tandem configurations, which could further improve overall device performance. However, challenges related to long-term stability, environmental impact, and large-scale manufacturability still limit their widespread adoption [1].

The choice of cell technology plays a crucial role in determining bifacial performance, particularly in terms of efficiency, bifaciality factor, and compatibility with specific applications. In building-integrated systems, additional aspects such as weight, transparency, and thermal behaviour must also be considered, further influencing the selection of the most appropriate technology.

Technology	Structure	Efficiency	Bifaciality	Fill Factor	Performance
PERC	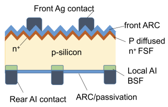	19.4–21.2% (front) 16.7–18.1% (rear) [30]	∼80% [30]	–	Rear-side passivation improves backside absorption.[1]
PERL	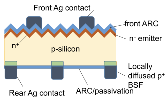	19.8% (front) [31]	≥89% [31]	82.8%[31]	Reduced recombination at rear interface due to passivation layer.[1]
PERT	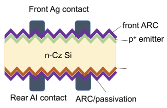	19.5–22% (front) 17–19% (rear) [32, 33]	≥85% [34]	–	High conductivity and reduced recombination improve voltage and FF.[1]
IBC	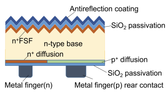	23.2% [35]	75% [36]	82.81% [36]	Rear-side contacts avoid front shading; enhanced light trapping.[1]
HIT	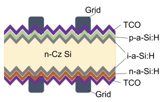	24.7% [37]	≥95% [38]	83.5% [1]	Heterojunction enables higher efficiency and voltage.[1]
TOPCon	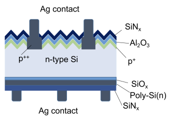	–	–	83.3% [1]	Ultra-thin oxide layer provides carrier selectivity.[1]
CGIS	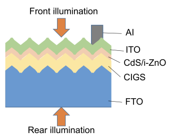	≥21% [39]	–	68.74% [40]	Low cost, simple process, but uses rare elements. [1]

Table 1.1: Summary of different BPV cell technologies. Structure schematics adapted from literature [1].

1.3.3 Bifacial gain: definition and influencing factors

The performance advantage of bifacial modules is commonly quantified through the bifacial gain, defined as the relative increase in energy yield compared to an equivalent monofacial system:

$$\text{Bifacial gain} = \frac{Y_{\text{bi}} - Y_{\text{mono}}}{Y_{\text{mono}}} \tag{1.1}$$

where Y_{bi} and Y_{mono} represent the energy yield of bifacial and monofacial modules, respectively [1].

Bifacial gain is not a fixed parameter but depends strongly on environmental and geometrical factors. Among these, ground albedo plays a dominant role: higher reflectivity surfaces significantly increase the irradiance received on the rear side. For example, highly reflective conditions such as snow-covered surfaces can substantially enhance rear-side irradiance, leading to considerable increases in energy production. Other important factors include installation height, tilt angle, row spacing, and shading conditions, all of which affect the magnitude and distribution of reflected radiation.

In addition, non-uniform rear irradiance represents a critical challenge for bifacial systems. Variations in reflected radiation caused by surrounding objects or heterogeneous surface properties can lead to current mismatch between cells, local overheating, and reduced system efficiency. These effects are particularly relevant in complex environments, such as urban contexts, where multiple surfaces contribute to irregular reflection patterns [1].

1.3.4 Current development and market relevance of bifacial PV

Bifacial photovoltaic technology has experienced rapid growth in recent years, driven by its potential to increase energy yield while improving the economic performance of photovoltaic systems. The additional energy production enabled by rear-side irradiance enhances land-use efficiency and contributes to a reduction in the levelized cost of electricity (LCOE). In particular, comparative studies have shown that bifacial modules can reduce LCOE by approximately 2–6% compared to conventional monofacial systems, depending on installation conditions and site characteristics [29].

From a market perspective, bifacial PV has transitioned from a niche technology to a rapidly expanding segment of the photovoltaic industry. Although its market share was below 5% in the late 2010s, projections indicate a significant increase in adoption in the coming years, supported by continuous technological improvements and cost reductions [1].

However, despite these advantages, the performance of bifacial systems remains highly context-dependent. Factors such as ground albedo, surrounding geometry, and installation configuration introduce additional complexity compared to monofacial systems, making accurate performance prediction more challenging. This aspect is particularly critical in building-integrated applications, where nearby surfaces and architectural elements strongly influence the magnitude and spatial distribution of rear-side irradiance.

For this reason, the integration of bifacial technology into buildings requires dedicated modelling approaches capable of capturing the interaction between solar radiation, geometry, and material properties. These aspects are explored in the following section, which focuses on building-integrated bifacial photovoltaic systems.

1.4 Building-integrated bifacial photovoltaic systems

Building-Integrated Photovoltaics (BIPV) represent a key strategy for the deployment of solar energy in urban environments, where available roof space is often limited and façades become an essential resource for energy generation. However, conventional BIPV systems are typically based on monofacial photovoltaic modules, whose performance is strongly dependent on direct solar irradiance and optimal orientation conditions. In vertical or near-vertical installations, such as building façades, the contribution of direct radiation is significantly reduced, leading to lower energy yields compared to optimally tilted rooftop systems.

In this context, bifacial photovoltaic technology offers a promising solution to overcome some of the inherent limitations of traditional BIPV systems. As discussed in the previous section, bifacial modules are capable of converting not only direct and diffuse irradiance on the front surface, but also reflected and scattered radiation incident on the rear side. This additional energy contribution reduces the dependence on optimal orientation and allows for improved performance under non-ideal conditions, which are typical in urban environments.

1.4.1 Rationale for combining BIPV and bifacial technology

The built environment provides particularly favourable conditions for bifacial operation. Unlike ground-mounted systems, buildings are characterised by the presence of multiple surrounding surfaces, such as façades, pavements, and adjacent structures, which can reflect solar radiation towards the rear side of the modules. This reflected component, commonly associated with surface albedo, can represent a significant fraction of the total irradiance received by bifacial systems. Moreover, urban geometries can enhance multiple reflections and increase the diffuse radiation component, further contributing to rear-side energy generation [1].

These characteristics make bifacial technology especially attractive for façade-integrated applications, where rear-side irradiance can partially compensate for the reduced direct solar exposure. At the same time, however, the performance of bifacial BIPV systems becomes strongly dependent on contextual factors such as surface reflectivity, geometric configuration, module spacing, and the presence of surrounding obstructions. This introduces additional complexity compared to conventional monofacial systems and requires a more detailed analysis of the interaction between solar radiation and the built environment.

For this reason, the effective implementation of bifacial BIPV systems cannot rely solely on conventional design approaches, but requires a careful assessment of system configuration and environmental conditions. In the following subsection, the main configurations of building-integrated bifacial photovoltaic systems investigated in the literature are presented, with particular attention to their influence on rear-side irradiance and overall system performance.

1.4.2 Role of rear-side irradiance in the built environment

The performance of bifacial photovoltaic systems is strongly influenced by the availability and distribution of rear-side irradiance, which represents the radiation incident on the rear surface of the module.

Rear-side irradiance can be expressed as the sum of three main components, namely diffuse, reflected, and beam radiation [41]:

$$G_{\text{rear}} = G_{\text{diffuse,r}} + G_{\text{reflected,r}} + G_{\text{beam,r}} \tag{1.2}$$

The diffuse component originates from the sky dome and contributes significantly under overcast or partially cloudy conditions. The reflected component is associated with radiation reflected by surrounding surfaces, and is strongly dependent on surface reflectivity, commonly described by the albedo. The beam component, although typically less significant on the rear side, may arise from direct or reflected solar radiation reaching the module depending on the system geometry.

Among these contributions, reflected radiation plays a particularly important role in bifacial systems. As shown in the literature, the rear irradiance increases with surface albedo, with highly reflective materials such as white membranes or snow-covered surfaces leading to significantly higher rear-side contributions compared to darker materials such as asphalt or soil [41]. This aspect is especially relevant in the built environment, where a variety of materials and surfaces can influence the magnitude of reflected radiation.

In urban contexts, the presence of surrounding buildings, façades, and ground surfaces introduces additional complexity in the distribution of rear irradiance. Multiple reflections between surfaces, as well as the geometric arrangement of the built environment, can enhance or reduce the amount of radiation reaching the rear side of the modules [1]. As a result, rear irradiance is highly site-specific and depends not only on climatic conditions but also on the local urban morphology.

The contribution of the different irradiance components also varies with surface orientation. In particular, vertical or near-vertical surfaces receive a reduced fraction of direct solar radiation compared to optimally tilted systems, while diffuse and reflected components become relatively more significant. This shift in irradiance composition is particularly relevant for building-integrated applications, where façades represent a major deployment surface.

In addition to its magnitude, rear irradiance is characterised by a non-uniform spatial distribution across the module surface. Effects such as self-shading, obstruction by nearby elements, and variations in ground reflectance can lead to significant differences in irradiance levels along the rear side of the module [41]. This non-uniformity can affect the electrical performance of bifacial systems and should be carefully considered in system design and modelling.

Overall, rear-side irradiance in the built environment is governed by a combination of radiative, geometric, and material factors, including albedo, system configuration, orientation, and the presence of surrounding structures. These aspects highlight the importance of considering the interaction between solar radiation and the built environment when analysing bifacial photovoltaic systems. Based on these considerations, the following subsection examines the main building-integrated configurations and their ability to exploit rear-side irradiance.

1.4.3 Main configurations investigated in the literature

Building-integrated bifacial photovoltaic (BIPV) systems can be implemented through a wide range of configurations, whose performance is strongly influenced by their interaction with the surrounding environment. Unlike conventional monofacial systems, bifacial modules are capable of harvesting solar irradiance from both the front and rear surfaces, making their energy yield highly dependent on the availability, magnitude, and spatial distribution of rear-side irradiance. This, in turn, is governed not only by solar geometry, but also by the system configuration, surrounding surfaces, and material properties [1].

To systematically analyse this complexity, bifacial BIPV configurations can be classified according to three complementary criteria: (i) integration within the building envelope, (ii) geometrical arrangement of the system, and (iii) rear-irradiance mechanisms. This classification enables a comprehensive understanding of how architectural design choices translate into physical effects on system performance.

(i) Integration-based configurations

This level describes how photovoltaic modules are incorporated into the building envelope, determining both their functional role and their exposure to environmental conditions.

Façade-integrated systems

- Flush-mounted façades: in this configuration, PV modules are directly attached to the building wall, with no intermediate air cavity. While this solution ensures structural simplicity and aesthetic integration, it effectively blocks the rear surface from receiving any significant irradiance. As a result, the system operates under conditions similar to monofacial modules, with negligible bifacial gain. Moreover, the absence of ventilation leads to higher operating temperatures, further reducing electrical efficiency.

- Ventilated façades: the introduction of an air cavity between the module and the wall represents a key improvement over flush-mounted systems. The gap allows air circulation, which enhances convective heat dissipation and reduces module temperature. At the same time, the cavity enables the rear surface to receive reflected radiation from the wall and surrounding surfaces, as well as a portion of diffuse sky irradiance. The size of the cavity and the optical properties of the wall become critical parameters in determining the magnitude of rear-side irradiance [19, 23].

- Double-skin façades (DSF): these systems consist of two building skins separated by a ventilated or mechanically controlled cavity. When bifacial modules are integrated into such systems, complex radiative exchanges occur between multiple surfaces, including reflections between the inner and outer skins. This configuration can enhance rear irradiance but also introduces significant complexity in both thermal and radiative behaviour, requiring careful design to avoid overheating or non-uniform irradiance distribution [45].

Glazing and curtain wall systems

In these configurations, semi-transparent or transparent bifacial modules are integrated into glazed façades. The presence of gaps between cells (low packing factor) allows partial transmission of light, enabling daylighting while generating electricity. Rear-side irradiance may originate not only from external reflections but also from interior surfaces, depending on building usage and lighting conditions. This dual interaction introduces additional complexity, as the optical and thermal behaviour of the system becomes strongly coupled with indoor environmental conditions [24].

Shading-integrated systems

- Brise-soleil: horizontal shading elements mounted on façades, designed to reduce solar gains while generating electricity. Their geometry allows exposure of both module surfaces to solar radiation, with the upper side receiving direct irradiance and the lower side capturing reflected and diffuse components.

- Louvers or fins: vertical or adjustable shading elements that can be oriented to optimise both shading performance and energy production. Their angular configuration affects the balance between front and rear irradiance, making them highly sensitive to solar position and orientation.

These systems are particularly effective in climates where solar control is required, as they combine passive cooling strategies with active energy generation [24].

Other architectural elements

Bifacial modules can also be integrated into non-conventional elements such as balcony railings, canopies, or façade extensions. Although these configurations are less standardised, they may offer favourable exposure to reflected radiation from the ground and surrounding surfaces. Their performance is highly case-specific and depends strongly on local geometry and material properties.

(ii) Geometrical configurations

The second level focuses on the spatial arrangement of the modules, which directly controls the amount of radiation reaching both the front and rear surfaces.

Module-to-wall distance (air gap)

- Zero gap: the rear surface is completely obstructed, preventing any significant radiative exchange.
- Small gap: limited rear irradiance is possible, but the proximity of the wall restricts the view of surrounding surfaces, reducing the contribution of reflected radiation.
- Large gap: increasing the distance enhances the visibility of both the ground and the sky, allowing a greater fraction of reflected and diffuse radiation to reach the rear surface. However, excessively large gaps may reduce the contribution from wall reflections and introduce structural challenges [1].

Tilt angle

- Vertical configurations: typical of façade systems, these receive reduced direct irradiance, especially at high latitudes, but benefit from a relatively higher contribution of diffuse and reflected radiation.
- Tilted configurations: tilting the modules away from the façade increases their exposure to direct solar radiation and expands the view of the ground, enhancing reflected irradiance. This configuration can significantly improve bifacial gain, especially in environments with high albedo [1].

Detached or spaced systems

Modules mounted at a distance from the façade or tilted outward create a more open geometry, improving radiative exchange with the environment. These configurations increase the effective view factors between the module and surrounding surfaces, leading to higher rear irradiance [1].

Orientation and layout

The orientation of the façade determines the temporal distribution of irradiance. South-facing systems maximise annual energy yield in the northern hemisphere, while east–west configurations provide a more distributed generation profile throughout the day. In urban environments, orientation must be considered together with shading from surrounding buildings, which can significantly alter both front and rear irradiance components.

Module arrangement and spacing

The relative positioning of modules affects mutual shading and the uniformity of irradiance distribution. In bifacial systems, non-uniform rear irradiance can lead to current mismatch between cells, reducing overall system efficiency [1]. Therefore, module spacing and layout must be carefully designed to balance energy yield and uniformity.

(iii) Rear-irradiance-driven configurations

The third level focuses on the physical processes governing rear-side irradiance, which ultimately determine the performance advantage of bifacial systems.

Diffuse-dominated configurations

In these systems, rear irradiance is primarily driven by diffuse radiation from the sky dome. This component becomes particularly important under overcast conditions or for vertical installations, where direct irradiance is limited.

Albedo-driven configurations

Reflected radiation from surrounding surfaces represents one of the most important contributions to rear irradiance. The magnitude of this component depends on surface reflectivity, or albedo. High-albedo conditions, such as snow-covered ground or light-coloured materials, can significantly enhance rear-side irradiance and increase bifacial gain [1].

Wall-reflected configurations

In façade-integrated systems, the building envelope itself can act as a reflecting surface. The contribution of wall-reflected radiation depends on both the optical properties of the façade and the distance between the module and the wall.

Urban multi-reflection configurations

In dense urban environments, multiple reflections between buildings, ground surfaces, and other elements can significantly influence rear irradiance.

Non-uniform irradiance conditions

Rear irradiance is rarely uniform across the module surface. Variations in geometry, shading, and surface reflectivity can lead to uneven irradiance distribution, which in turn causes electrical mismatch between cells. This effect can reduce system performance and must be considered in both design and modelling of bifacial systems [1].

Overall, this classification demonstrates that bifacial BIPV configurations are governed by a complex interplay between architectural integration, geometrical parameters, and radiative processes. These factors collectively determine the magnitude and distribution of rear-side irradiance, and therefore the achievable bifacial gain. The strong dependency of system performance on configuration and environmental conditions highlights the necessity of advanced modelling approaches capable of accurately describing these interactions in the built environment.

The main configurations discussed above are summarised in Table 2, which provides an overview of the different integration strategies, geometrical arrangements, and rear-irradiance mechanisms, together with their main characteristics and impact on rear-side irradiance.

Category	**Configuration**	**Description**	**Effect on rear irradiance**
Integration-based	Flush-mounted façade	Modules directly attached to wall, no air gap	Negligible rear irradiance (monofacial behaviour)
	Ventilated façade	Air cavity between module and wall	Increased rear irradiance from wall and diffuse components
	Double-skin façade (DSF)	Two façade layers with cavity	Multiple reflections, enhanced rear irradiance
	Glazing / curtain wall	Semi-transparent bifacial modules	Rear irradiance from indoor and outdoor reflections
	Shading systems	Brise-soleil, louvers, fins	Both sides active, capturing direct and reflected radiation
	Other elements	Railings, canopies, façade extensions	Strongly dependent on surrounding geometry
Geometrical	Module-to-wall distance	Distance between panel and façade	Larger gap increases rear irradiance
	Tilt angle	Orientation relative to façade	Tilt increases exposure to ground and sky
	Detached systems	Modules spaced away from façade	Higher view factors enhance rear irradiance
	Orientation	Direction of façade	Affects temporal distribution of irradiance
	Module spacing	Distance between modules	Influences shading and irradiance uniformity
Rear-irradiance-driven	Diffuse-dominated	Irradiance mainly from sky	Uniform but moderate contribution
	Albedo-driven	Reflection from surroundings	High rear irradiance in high-albedo conditions
	Wall-reflected	Reflection from building envelope	Relevant in ventilated façades
	Urban multi-reflection	Multiple reflections in urban areas	Complex, site-specific enhancement
	Non-uniform irradiance	Spatial variability of irradiance	Can lead to mismatch losses

Table 1.2: Bifacial BIPV configurations and their impact on rear-side irradiance

1.5 Modelling approaches for bifacial BIPV façades

1.5.1 Optical modelling: view factor vs ray tracing

In bifacial photovoltaic systems, the modelling of incident irradiance plays a fundamental role in the accurate evaluation of energy performance and in the proper design of the system. Unlike monofacial modules, bifacial technologies interact with a more complex radiative environment, in which the incoming radiation is not limited to the direct solar component, but also includes diffuse contributions from the sky and reflected radiation from the ground and surrounding surfaces.

As a result, the irradiance distribution on the module surfaces, particularly on the rear side, is strongly affected by geometric, optical, and environmental parameters. Factors such as ground albedo, array configuration, nearby obstacles, and the optical properties of surrounding materials can significantly influence both the magnitude and the spatial distribution of the incident radiation. Consequently, the accurate modelling of radiative exchange is essential not only for the estimation of the energy yield, but also for the analysis of phenomena such as non-uniform irradiance distributions, electrical mismatch effects, and associated performance losses.

The representation of these radiative interactions requires the adoption of optical models capable of describing the exchange of radiation between the photovoltaic modules and the surrounding environment with an appropriate balance between physical accuracy and computational efficiency. Different modelling approaches have been proposed in the literature, each characterised by specific assumptions and levels of complexity.

Among the available approaches, *view factor methods* and *ray tracing methods* are the most widely employed for the optical modelling of bifacial photovoltaic systems. In the following sections, these methods are presented and compared, with particular attention to their underlying assumptions, modelling capabilities, and applicability to bifacial BIPV systems.

View factors methods

View factor methods, also referred to as configuration factor approaches, are widely used for the estimation of radiative exchange in bifacial photovoltaic systems [19]. These methods are grounded in the theory of radiative heat transfer and rely on the geometric relationship between emitting and receiving surfaces to quantify the fraction of radiation exchanged between them.

A view factor $F_{A \to B}$ represents the proportion of radiant energy leaving a surface A that directly reaches another surface B, and depends exclusively on the relative orientation, distance, and visibility between the two surfaces. In its most general formulation, the view factor between two surfaces can be expressed as [42]:

$$F_{A\to B} = \frac{1}{A_A} \int_{A_A} \int_{A_B} \frac{\cos\theta_A \cos\theta_B}{\pi r^2} \, dA_B \, dA_A \tag{1.3}$$

where A_A is the area of the emitting surface, θ_A and θ_B are the angles between the surface normals and the line connecting the differential elements, and r is the distance between them. This formulation highlights the purely geometric nature of radiative exchange under the assumption of diffuse emission, where energy transfer is governed by line-of-sight interactions between surfaces.

In the context of bifacial PV systems, view factor methods are employed to estimate the irradiance incident on both the front and rear surfaces of the module by decomposing the radiative environment into a set of contributing surfaces. Typically, these include the sky dome, the ground, and surrounding objects such as adjacent modules or nearby structures [19]. The total irradiance incident on a given surface is then computed as the weighted sum of the contributions from these sources, with the weights defined by the corresponding view factors.

In practical implementations, the general integral formulation is rarely evaluated directly due to its computational complexity. Instead, simplified analytical or semi-analytical expressions are derived by introducing assumptions on geometry and surface properties. These often include idealised configurations, such as infinitely extended planar surfaces or regularly spaced module arrays, which allow the reduction of the double surface integral into closed-form expressions based on geometric parameters [19]. Such formulations enable efficient computation of view factors and are particularly suitable for large-scale simulations and long-term energy yield assessments.

A fundamental assumption underlying most view factor models is that all surfaces behave as Lambertian reflectors, meaning that radiation is reflected isotropically in all directions. This assumption significantly simplifies the problem, as it removes the need to account for directional dependencies in reflection. However, it also introduces limitations, as real surfaces may exhibit anisotropic and wavelength-dependent reflectance characteristics that are not captured by this approximation.

Another common assumption concerns the spatial uniformity of irradiance across surfaces. In many implementations, the radiative exchange is evaluated either analytically over idealised geometries or at representative locations, implicitly neglecting local variations in irradiance due to shading, reflections, or geometric discontinuities. While this is generally acceptable for system-level analyses, it may lead to inaccuracies when strong spatial gradients are present.

Furthermore, view factor approaches often rely on simplified representations of the system geometry. For instance, photovoltaic arrays are frequently modelled as infinitely extended in one or more directions, allowing periodic boundary conditions to be applied. While this assumption reduces computational complexity, it inherently neglects finite-size effects such as edge-related irradiance enhancements or reductions.

Despite these limitations, view factor methods offer a favourable balance between physical consistency and computational efficiency. They are capable of capturing the dominant radiative exchange mechanisms in bifacial PV systems while maintaining relatively low computational requirements. As a result, they are widely adopted in both academic and industrial contexts, and form the basis of several established simulation tools for photovoltaic performance assessment.

Widely used implementations of view factor approaches include software such as *PVSyst* and the NREL bifacial view factor model [43], which are commonly employed for system-level simulations. These tools typically incorporate additional modelling features, such as sky diffuse irradiance models and empirical corrections, to improve the accuracy of irradiance predictions while preserving computational efficiency.

Overall, view factor methods provide a robust and scalable framework for modelling radiative exchange in bifacial photovoltaic systems, particularly in cases where the geometry can be reasonably approximated and computational efficiency is a key requirement. However, their reliance on simplifying assumptions necessitates careful consideration of their applicability when dealing with complex geometries or highly heterogeneous radiative environments.

Ray tracing methods

Ray tracing methods represent a physically detailed approach for modelling solar irradiance in bifacial photovoltaic systems. In contrast to view factor methods, which rely on geometric relationships between surfaces, ray tracing simulates the propagation of individual light rays within a defined three-dimensional environment. Each ray is emitted from a source and tracked through space, undergoing interactions such as reflection, absorption, and transmission depending on the optical properties of the surfaces encountered.

The fundamental principle of ray tracing is based on geometrical optics, where radiation is represented as discrete rays travelling in specific directions. When a ray intersects a surface, its behaviour is determined by the material properties, which may include diffuse and specular reflection components, as well as wavelength-dependent characteristics. This allows for a highly flexible and realistic representation of radiative exchange processes, particularly in complex environments.

One of the main advantages of ray tracing methods is their ability to handle arbitrary geometries without the need for simplifying assumptions such as infinite surfaces or idealised configurations. This makes them particularly suitable for modelling BIPV systems, where architectural elements, façade geometries, and surrounding urban features can significantly influence the irradiance distribution. In such cases, ray tracing can accurately capture shading effects, multiple reflections, and the contribution of nearby structures.

Moreover, ray tracing enables the spatially resolved calculation of irradiance across the surface of photovoltaic modules. This is particularly relevant for bifacial systems, where rear-side irradiance may exhibit strong non-uniformities due to localised reflections and partial shading. By discretising the module surface into small elements, ray tracing models can provide detailed irradiance maps, which can then be coupled with electrical models to assess mismatch losses and performance degradation.

Ray tracing techniques are typically implemented using physically-based rendering engines such as *Radiance* [44], which has been widely adopted in the photovoltaic community. Advanced tools, such as the NREL *bifacial_radiance* framework [43], extend these capabilities by integrating solar geometry, material properties, and PV-specific modelling features. These tools allow for high-fidelity simulations of both front- and rear-side irradiance under realistic environmental conditions.

Despite their high level of accuracy, ray tracing methods are associated with significant computational requirements. The need to simulate a large number of rays and their interactions leads to increased simulation time, particularly when high spatial resolution or long temporal datasets are considered. Additionally, the accuracy of the results depends on the number of rays traced and the level of detail used in the geometric and material modelling, which further increases computational cost.

For these reasons, ray tracing is often employed in detailed design studies, validation of simplified models, or research applications where high accuracy is required. In contrast, its use in large-scale or long-term simulations may be limited due to computational constraints.

Overall, ray tracing methods provide a comprehensive and physically consistent framework for modelling radiative exchange in bifacial PV systems, particularly in complex geometries and heterogeneous environments. However, the trade-off between accuracy and computational cost remains a key consideration in their practical application.

Comparison between approaches

The choice between view factor and ray tracing approaches involves a fundamental trade-off between computational efficiency and modelling accuracy. View factor methods rely on simplified geometric relationships to estimate radiative exchange, allowing for fast and scalable simulations. As a result, they are particularly well suited for long-term analyses, such as annual energy yield calculations and parametric studies, where computational cost is a critical constraint.

In contrast, ray tracing methods provide a more detailed and physically comprehensive representation of radiative processes by explicitly simulating the propagation and interaction of individual light rays. This enables the accurate modelling of complex geometries, multiple reflections, and spatially non-uniform irradiance distributions, which are typically neglected or approximated in view factor formulations.

From a modelling perspective, view factor approaches generally require a number of simplifying assumptions, including Lambertian reflection, idealised geometries, and, in some cases, spatial averaging of irradiance. While these assumptions may limit the accuracy of the results in complex environments, they allow for a transparent and computationally efficient formulation of the problem. Conversely, ray tracing methods relax many of these assumptions, enabling the inclusion of realistic material properties, directional reflectance behaviour, and detailed geometric features.

In the context of bifacial BIPV façades, where the interaction between the photovoltaic modules and the surrounding built environment plays a significant role, the selection of the modelling approach depends on the level of detail required. View factor methods can provide a practical and efficient approximation of the dominant radiative exchanges, particularly in early-stage design or large-scale simulations. On the other hand, ray tracing methods are more suitable for detailed analyses of specific configurations, where accurate representation of shading, reflections, and spatial variability is essential.

Overall, view factor and ray tracing approaches should not be regarded as competing methods, but rather as complementary tools. The former offers efficiency and simplicity, while the latter provides accuracy and flexibility. The appropriate choice depends on the objectives of the analysis, the complexity of the system, and the available computational resources.

1.5.2 Thermal modelling of ventilated façades

The thermal behaviour of BIPV systems plays a crucial role in determining both their electrical performance and their interaction with the building envelope. In photovoltaic modules, the conversion efficiency decreases with increasing operating temperature, making accurate temperature prediction essential for reliable performance assessment. This aspect is particularly relevant in façade-integrated configurations, where reduced rear-side ventilation may lead to higher operating temperatures compared to open-field installations.

Ventilated façade systems are commonly adopted to mitigate this effect by promoting airflow within an air cavity between the photovoltaic modules and the building envelope. This configuration enhances heat removal from the modules and reduces heat transfer to the interior of the building. As a result, the thermal modelling of ventilated BIPV façades is essential not only for predicting the electrical output of the PV system, but also for evaluating its impact on building energy performance.

From a physical perspective, a ventilated BIPV façade can be interpreted as a system composed of two parallel surfaces separated by an air cavity, in which airflow develops due to thermal and/or mechanical driving forces. The thermal behaviour of this system is governed by the interaction of multiple heat transfer mechanisms, including solar radiation absorption, conductive heat transfer through the module and the wall, and convective heat exchange within the air cavity.

Among these mechanisms, convective heat transfer within the cavity plays a dominant role, particularly in naturally ventilated configurations. In such cases, airflow is primarily driven by buoyancy forces arising from temperature differences between the air inside the cavity and the ambient environment. This phenomenon, commonly referred to as the stack effect, induces an upward flow of heated air, which is replaced by cooler air entering from the lower openings of the façade. The resulting airflow significantly enhances heat removal from the photovoltaic modules and strongly influences their operating temperature.

The behaviour of airflow within the cavity depends on several factors, including the height of the façade, the thickness of the air gap, the intensity of solar radiation, and the thermal properties of the involved surfaces. Due to the coupling between heat transfer and fluid flow, the thermal modelling of ventilated façades inherently involves both thermodynamic and fluid dynamic considerations. This complexity motivates the development of different modelling approaches, ranging from simplified empirical correlations to detailed numerical simulations, depending on the level of accuracy required and the computational resources available.

Empirical and lumped models

Empirical and lumped-parameter models represent the simplest approach for the thermal analysis of ventilated BIPV façades. These models are widely used in photovoltaic thermal modelling to relate the operating temperature of the module to environmental conditions through simplified heat transfer coefficients, without explicitly resolving the underlying heat transfer and airflow processes [22, 45].

A widely adopted formulation is the model proposed by Faiman [22], in which the module temperature is expressed as a function of ambient temperature, solar irradiance, and an overall heat transfer coefficient:

$$T_{pv} = T_{amb} + \frac{G}{U_0 + U_1 v} \tag{1.4}$$

where T_{pv} is the module temperature, T_{amb} is the ambient air temperature, G is the incident irradiance, v is the wind speed, and U_0 and U_1 are empirical heat loss coefficients. In this formulation, the combined effects of radiative and convective heat transfer are incorporated into effective coefficients, avoiding the need for a detailed physical description of the system.

In the context of ventilated façades, similar approaches are extended by incorporating the effect of airflow within the cavity into effective heat transfer coefficients. As discussed in the literature, convective heat transfer in double skin and BIPV façades is often modelled using empirical correlations expressed in terms of dimensionless numbers such as the Nusselt, Rayleigh, and Reynolds numbers [45]. These correlations provide simplified relationships for estimating heat transfer coefficients without explicitly solving the fluid flow within the cavity.

The main advantage of empirical models lies in their computational efficiency and ease of implementation, making them particularly suitable for long-term simulations and parametric analyses. However, their accuracy depends strongly on the validity of the empirical correlations and coefficients employed, which are typically derived under specific experimental or idealised conditions. In particular, correlations developed for closed cavities or simplified geometries may not be directly applicable to naturally ventilated BIPV façades, where airflow occurs in open channels and is strongly influenced by boundary conditions and system geometry [45].

Overall, empirical and lumped models provide a practical and computationally efficient framework for estimating module temperature, but they do not explicitly capture the coupling between heat transfer and airflow within the cavity, which may limit their accuracy in detailed analyses of ventilated façade systems.

Analytical models

Analytical or nodal models provide a more physically representative description of the thermal behaviour of ventilated BIPV façades compared to purely empirical approaches. In these models, the system is discretised into a set of interconnected nodes, typically representing the photovoltaic module, the air within the ventilated cavity, and the building envelope. Each node is governed by an energy balance equation describing the heat exchanges with adjacent components and the surrounding environment [45, 19].

The thermal balance for each node accounts for the dominant heat transfer mechanisms within the system, including absorbed solar radiation, conductive heat transfer through solid layers, radiative exchange between surfaces, and convective heat transfer with the ambient air and cavity airflow. For the photovoltaic module, the energy balance can be generally expressed as:

$$C_{pv}\frac{dT_{pv}}{dt} = \alpha G - q_{conv} - q_{rad} - q_{cond} \tag{1.5}$$

where C_{pv} is the effective thermal capacitance of the module, αG represents the absorbed solar radiation, and q_{conv}, q_{rad}, and q_{cond} denote the convective, radiative, and conductive heat transfer terms, respectively [45, 46].

A key aspect of analytical models is the representation of airflow within the ventilated cavity. In naturally ventilated façades, the airflow is generally estimated through simplified formulations based on buoyancy-driven flow and stack-effect correlations, linking the airflow rate to temperature differences within the cavity [45]. As a result, the thermal and fluid dynamic behaviour of the system are inherently coupled, since the airflow influences convective heat transfer while simultaneously being affected by the temperature distribution.

Convective heat transfer coefficients are commonly estimated using empirical or semi-empirical correlations expressed in terms of dimensionless numbers such as Nusselt, Rayleigh, and Reynolds numbers [45, 46]. Although these correlations enable practical implementation of the models, their applicability may depend on the specific geometrical configuration and flow regime considered.

However, despite their improved physical basis, analytical models still rely on simplifying assumptions, particularly in the treatment of airflow and convective heat transfer. The cavity airflow is often represented using one-dimensional or averaged formulations, while local phenomena such as flow separation, turbulence, and spatially non-uniform temperature distributions are generally neglected. Consequently, the accuracy of these models may decrease when applied to complex façade geometries or strongly heterogeneous operating conditions [45, 46].

Computational Fluid Dynamics models

Computational Fluid Dynamics (CFD) models provide a detailed numerical framework for the analysis of heat transfer and airflow phenomena in photovoltaic and BIPV systems. Unlike simplified analytical approaches, CFD methods explicitly solve the governing equations of fluid flow and heat transfer within a discretised computational domain, enabling the spatially resolved prediction of temperature, velocity, and pressure fields [47, 48, 46].

In the context of BIPV applications, CFD models are widely employed to investigate the thermal behaviour of photovoltaic modules and ventilated cavities, where the interaction between buoyancy-driven airflow, convective heat transfer, and radiative exchange strongly affects the operating temperature of the system. These methods are particularly suitable for configurations characterised by complex geometries, non-uniform temperature distributions, and multidimensional airflow patterns, which are difficult to capture using simplified nodal formulations [47, 48].

The governing equations solved in CFD simulations generally include the conservation equations for mass, momentum, and energy. Depending on the level of modelling detail, additional equations may be introduced to account for turbulence, radiative heat transfer, and conjugate heat transfer within solid components [46]. The numerical solution is typically obtained through finite-volume discretisation methods implemented in commercial or open-source CFD solvers such as *ANSYS Fluent* or *OpenFOAM* [47, 46].

Different modelling approaches can be adopted depending on the characteristics of the problem. Simulations may be performed in two-dimensional or three-dimensional domains, under steady-state or transient conditions, and considering either natural or forced convection. In naturally ventilated BIPV façades, buoyancy-driven airflow is commonly modelled through the coupling between temperature and density variations, while mechanically ventilated systems may include prescribed inlet velocity conditions [48].

The treatment of turbulence represents another important aspect of CFD modelling. In photovoltaic applications, Reynolds-Averaged Navier–Stokes (RANS) approaches are commonly employed due to their balance between computational cost and accuracy. Among these, the RNG $k-\varepsilon$ turbulence model is frequently adopted for the simulation of airflow and heat transfer around photovoltaic modules and ventilated cavities [47, 48]. More advanced approaches, such as Large Eddy Simulation (LES), may also be used when detailed transient flow structures are of interest, although at significantly higher computational cost.

Radiative heat transfer can be incorporated through dedicated radiation models, including discrete transfer methods, surface-to-surface radiation models, or participating media formulations, depending on the required level of detail and the optical characteristics of the system [47, 48]. These formulations allow the simultaneous representation of convective and radiative heat exchanges within the computational domain.

An important aspect of CFD modelling is the definition of the computational mesh and boundary conditions. The accuracy of the solution depends strongly on mesh quality and spatial resolution, particularly near solid boundaries where steep thermal and velocity gradients may occur. Consequently, mesh independence analyses and model validation against experimental measurements are commonly performed to ensure the reliability of the numerical predictions [47, 48, 46].

Overall, CFD methods provide a comprehensive and physically detailed approach for the thermal analysis of photovoltaic and BIPV systems, enabling the investigation of local heat transfer phenomena and complex airflow behaviour within the system.

Comparison between approaches

Empirical, analytical, and CFD approaches represent different levels of complexity in the thermal modelling of ventilated BIPV systems, each characterised by a different balance between computational efficiency, physical accuracy, and modelling flexibility.

Empirical and lumped-parameter models rely on simplified correlations relating the module temperature to environmental variables such as irradiance, ambient temperature, and wind speed. Their main advantage lies in their low computational cost and ease of implementation, which make them particularly suitable for long-term simulations, early-stage design analyses, and integration into building energy simulation tools [22, 45]. However, since the underlying heat transfer and airflow phenomena are not explicitly resolved, their applicability is generally limited to conditions similar to those under which the empirical coefficients were derived.

Analytical or nodal models introduce a more physically based representation of the system by explicitly formulating energy balance equations for the different façade components. Compared to empirical approaches, they allow the interaction between conduction, convection, radiation, and airflow within the cavity to be represented in a more consistent manner [45, 19]. In addition, transient effects and thermal inertia can be incorporated while maintaining relatively moderate computational requirements. Nevertheless, these models still rely on simplified assumptions for the airflow and heat transfer coefficients, which may limit their ability to capture multidimensional and highly non-uniform thermal phenomena.

CFD approaches provide the highest level of physical detail among the considered methods. By directly solving the governing equations of fluid flow and heat transfer within a discretised domain, CFD models enable the spatially resolved analysis of temperature distributions, airflow structures, turbulence effects, and local heat transfer mechanisms [47, 48, 46]. This makes them particularly suitable for the investigation of naturally ventilated cavities, complex façade geometries, and configurations characterised by strong thermal and flow non-uniformities. Furthermore, CFD methods offer significant flexibility in the representation of boundary conditions, radiative exchange, and turbulence models.

The increased physical accuracy of CFD simulations, however, is associated with significantly higher computational cost and modelling complexity. The generation of an appropriate computational mesh, the definition of boundary conditions, and the selection of turbulence and radiation models require careful consideration and validation. In addition, simulation times may become substantial for three-dimensional or transient analyses.

Overall, the choice of the modelling approach depends on the objectives of the analysis, the required level of detail, and the available computational resources. Empirical models are generally suitable for simplified or large-scale simulations, analytical models provide an intermediate level of physical representation with moderate computational requirements, while CFD approaches are more appropriate for detailed investigations of local thermo-fluid dynamic phenomena in ventilated BIPV systems.

1.5.3 Optical-thermal coupling approaches

In bifacial BIPV modelling, the optical and thermal domains are strongly interconnected, since the irradiance distribution calculated by the optical model constitutes the primary input for the thermal analysis. The absorbed solar radiation determines the heat generation within the photovoltaic module and therefore directly affects the temperature distribution of both the module and the ventilated cavity.

The coupling between optical and thermal models becomes particularly relevant in bifacial configurations due to the strong dependence of rear-side irradiance on surrounding geometry, surface reflectance, and multiple reflections. Unlike monofacial systems, the rear irradiance contribution may exhibit significant spatial and temporal non-uniformities, especially in urban and façade-integrated applications. Consequently, the resulting thermal field cannot be accurately represented through uniform irradiance assumptions.

Different coupling strategies may be adopted depending on the required modelling detail. In simplified approaches, the optical and thermal models are solved sequentially. The irradiance distribution obtained from view factor or ray tracing calculations is transferred to the thermal model as a boundary condition or heat source term within the energy balance equations governing the façade components. This approach is commonly employed in analytical and nodal thermal models due to its relatively low computational cost [19].

More advanced formulations involve a stronger integration between radiative, thermal, and fluid dynamic phenomena. In CFD-based approaches, the absorbed radiation may be directly incorporated into the governing energy equation as a distributed source term, while airflow and heat transfer are solved simultaneously through the coupled solution of continuity, momentum, turbulence, and energy equations [48, 46]. This allows the detailed investigation of local temperature gradients, buoyancy-driven airflow, and convective heat transfer mechanisms within naturally ventilated cavities.

Coupled optical-thermal-electrical frameworks have also been proposed in the literature for bifacial BIPV systems. Tina et al. [19] developed a multilayer transient model in which the irradiance incident on the front and rear surfaces of the module is coupled with the thermal energy balances of the façade layers. In this formulation, conductive, convective, and radiative heat transfer mechanisms are simultaneously considered, while the resulting module temperature is used to evaluate the temperature-dependent electrical efficiency of the photovoltaic system.

The integration of optical and thermal models therefore represents a fundamental step towards the accurate simulation of bifacial BIPV systems, particularly when local irradiance conditions and ventilation effects play a significant role in determining the operating behaviour of the façade. The relevance of these coupled approaches becomes even more pronounced in high-latitude applications, where the characteristics of the solar resource and the increased contribution of diffuse and reflected radiation further strengthen the interaction between optical and thermal phenomena.

1.6 Bifacial BIPV systems in Nordic climates

The integration of bifacial BIPV systems in Nordic regions presents both significant opportunities and specific technical challenges. Unlike conventional photovoltaic applications developed for lower-latitude climates, solar energy systems operating at high latitudes are exposed to distinct radiative and environmental conditions, including low solar elevations, strong seasonal variability, high diffuse irradiance fractions, and seasonal snow cover. These factors substantially influence the magnitude and distribution of both front- and rear-side irradiance, making the performance of bifacial façade-integrated systems strongly climate-dependent.

At the same time, several characteristics of Nordic environments may be particularly favourable for bifacial vertical configurations. The combination of diffuse radiation, low-angle solar incidence, and highly reflective snow-covered surfaces can enhance rear-side irradiance and partially compensate for the reduced direct solar exposure typically associated with vertical installations. For these reasons, understanding the interaction between high-latitude solar conditions and bifacial BIPV behaviour is essential for the accurate assessment and modelling of such systems.

1.6.1 Solar resource characteristics at high latitudes

Solar energy availability at high latitudes is characterized by climatic and geometrical conditions that differ significantly from those observed in lower-latitude regions. In Nordic countries, the solar resource is not only reduced in terms of annual irradiation, but also strongly affected by seasonal variability, low solar elevation angles, and pronounced changes in daylight duration throughout the year. These characteristics substantially influence the spatial and temporal distribution of solar irradiance and must therefore be carefully considered when evaluating photovoltaic applications in northern climates.

One of the main distinguishing features of high-latitude regions is the low average solar elevation. Due to the high geographical latitude, the sun remains relatively close to the horizon for most of the year, particularly during winter months. As a consequence, the angle of incidence between solar radiation and building surfaces changes significantly compared to lower-latitude locations. At the same time, the annual solar cycle becomes highly seasonal, with very long daylight periods during summer and extremely short days during winter. This results in large temporal variations in available solar irradiance and in the corresponding photovoltaic energy production.

Another important characteristic of northern climates is the wider azimuthal solar path. At high latitudes, the sun follows a lower and more extended trajectory across the sky dome, especially during summer months. Consequently, solar exposure is distributed over a broader range of azimuth angles compared to regions closer to the equator. This aspect affects the irradiance received by building envelopes and increases the importance of façade orientation in determining the solar potential of urban surfaces.

In addition to solar geometry effects, atmospheric conditions typical of Nordic regions also influence the composition of solar irradiance. Cloud cover and low solar elevations increase the relative contribution of diffuse radiation compared to direct beam irradiance. Under these conditions, the diffuse component of the sky dome becomes a significant fraction of the total available irradiance, particularly during winter and intermediate seasons. Moreover, the low position of the sun enhances near-horizon scattering phenomena, making the angular distribution of diffuse radiation more relevant than in conventional photovoltaic applications located at lower latitudes.

Seasonal snow cover further modifies the radiative characteristics of high-latitude environments. Snow-covered surfaces can exhibit very high albedo values, substantially increasing the amount of reflected radiation within the built environment. Although snow presence is inherently seasonal, its effect on reflected irradiance may become particularly significant during winter and early spring periods, when direct solar radiation is limited and reflected as well as diffuse components contribute more substantially to the total irradiance balance.

Therefore, solar resource assessment at high latitudes cannot rely solely on annual global irradiation values, but must also account for the specific angular, temporal, and radiative distribution of solar energy. Low solar elevations, strong seasonal variability, enhanced diffuse radiation, and high winter albedo collectively create environmental conditions that differ substantially from conventional lower-latitude climates. Under these circumstances, the interaction between solar geometry, surface orientation, and reflected radiation becomes particularly relevant, making vertical and bifacial photovoltaic configurations of growing interest for building-integrated applications in Nordic regions.

1.6.2 Opportunities and limitations of vertical configurations

The radiative conditions typical of Nordic climates create a context in which vertical bifacial photovoltaic configurations may become particularly attractive compared to conventional rooftop systems. While vertically mounted modules generally receive lower annual direct irradiance than optimally tilted south-facing installations, the characteristics previously described of high-latitude environments can partially compensate for this limitation and enhance the performance of façade-integrated bifacial systems.

One of the main advantages of vertical configurations at high latitudes is their interaction with low solar elevation angles. During winter and intermediate seasons, when the sun remains close to the horizon for extended periods, vertical façades can intercept solar radiation more effectively than low-tilt rooftop systems. This effect becomes especially relevant for south-facing and east–west-oriented façades, whose irradiance profile is more closely aligned with the low-angle solar trajectories characteristic of Nordic regions [49, 50].

In addition, vertical bifacial systems can benefit significantly from the enhanced contribution of diffuse and reflected radiation discussed in the previous section. Since the rear side of bifacial modules is able to harvest radiation reflected by snow-covered ground, pavements, and surrounding surfaces, high-albedo winter conditions may substantially increase rear-side irradiance and partially offset the reduction in direct beam radiation. This aspect is particularly important in Nordic climates, where seasonal snow cover can persist for long periods and strongly modify the local radiative environment [14, 49, 19].

Another important advantage of vertical façade systems is the reduced impact of snow accumulation on the active photovoltaic surface. Unlike rooftop installations, where snow deposition may completely obstruct solar radiation and cause significant winter production losses, vertical modules are generally less affected by snow coverage due to their orientation. At the same time, snow located on the ground in front of the façade may increase surface reflectivity and further enhance bifacial gain through additional rear-side irradiance [49].

Vertical east–west configurations may also provide a more distributed daily production profile compared to conventional south-facing systems. Instead of concentrating electricity generation around solar noon, vertically mounted east–west systems tend to produce more energy during morning and evening hours, potentially improving the temporal match between photovoltaic production and building electricity demand. This aspect can become particularly relevant in urban environments and in high-latitude regions, where winter electricity demand is typically concentrated outside midday hours [49].

Despite these advantages, vertical bifacial configurations also present important limitations. Due to their geometry, vertical systems generally receive lower annual global irradiation than optimally tilted rooftop installations, especially during summer months when solar elevations are higher. Their performance is also strongly influenced by local environmental conditions, including façade orientation, surrounding obstructions, urban density, and surface reflectivity. In dense urban contexts, the low solar elevations characteristic of Nordic regions can produce long shadowing effects that significantly affect both front- and rear-side irradiance distributions [51, 19].

Furthermore, the strong dependence on diffuse and reflected radiation introduces additional complexity in system modelling and performance prediction. The accurate estimation of rear-side irradiance under low solar elevations, variable snow conditions, and complex urban geometries remains a challenging task, particularly because many conventional irradiance transposition models were not specifically developed or validated for vertical bifacial systems operating at high latitudes [**?**, 49].

In this context, vertical bifacial BIPV systems should not be regarded simply as less efficient alternatives to conventional rooftop photovoltaics, but rather as climate-specific configurations whose performance depends strongly on the interaction between solar geometry, surface reflectivity, urban morphology, and system design.

1.6.3 Existing studies on bifacial BIPV systems in Nordic climates

In recent years, increasing research attention has been devoted to the application of bifacial photovoltaic technologies in high-latitude regions, where the peculiar radiative characteristics of Nordic climates create conditions substantially different from those encountered in conventional photovoltaic applications. Low solar elevation angles, enhanced diffuse irradiance, extended summer daylight periods, and seasonal snow cover collectively influence the angular and temporal distribution of solar radiation, making vertical bifacial configurations particularly attractive for building-integrated applications. Consequently, several studies have investigated the behaviour of bifacial systems under these conditions, ranging from irradiance modelling and experimental outdoor measurements to urban-scale and building-integrated applications.

Among the most relevant contributions in this field, Khan et al. [52] developed a detailed physical model for vertically mounted bifacial photovoltaic systems, focusing on the combined effects of direct, diffuse, and ground-reflected irradiance together with mutual shading and non-uniform illumination phenomena. Their study demonstrated that the geometry of solar trajectories at high latitudes significantly modifies the irradiance distribution received by vertical surfaces, increasing the relevance of east–west-oriented bifacial configurations. The authors showed that diffuse and reflected radiation may become major contributors to the total collected energy under low solar elevations, while rear-side irradiance strongly depends on surrounding reflectivity and geometric shading interactions. The work also highlighted that the illumination of bifacial modules is inherently non-uniform, particularly under complex shading conditions, emphasizing the need for detailed irradiance modelling approaches capable of accounting for spatially distributed rear-side radiation and electrical mismatch effects.

Further investigations specifically addressed the application of bifacial photovoltaic systems to building-integrated and urban configurations under northern climatic conditions. Manni et al. [49] analyzed the performance of vertical bifacial photovoltaic façades by considering the combined effects of façade orientation, diffuse irradiance, surrounding reflections, and seasonal climatic variability typical of high-latitude environments. Their studies highlighted how the contribution of reflected and diffuse radiation becomes increasingly relevant for façade-integrated systems operating under low solar elevations, particularly in dense urban areas where surrounding surfaces significantly influence rear-side irradiance. The authors also emphasized that vertical bifacial systems may provide more balanced seasonal and daily production profiles compared to conventional rooftop installations, while simultaneously reducing snow accumulation losses on the active photovoltaic surface. At the same time, the studies pointed out that the accurate prediction of bifacial gain in urban environments remains particularly challenging due to the strong dependence on local geometry, shadowing effects, and the complex angular distribution of reflected radiation.

The importance of snow-related albedo effects under Nordic conditions was experimentally investigated by Molin et al. [53], who performed outdoor measurements on bifacial photovoltaic modules installed in Sweden. Their work compared conventionally mounted and vertically mounted bifacial systems under real climatic conditions, highlighting the strong influence of seasonal surface reflectivity on bifacial gain. Although the annual increase in energy production remained relatively moderate under low-albedo conditions, winter measurements revealed a substantial enhancement of rear-side irradiance during sunny snow-covered periods. In particular, vertically mounted bifacial modules exhibited bifacial gains of up to 48% during snowy days, demonstrating how seasonal snow cover can significantly amplify the contribution of reflected radiation in northern climates. The study also confirmed that vertical configurations are less vulnerable to snow accumulation on the active photovoltaic surface, simultaneously reducing obstruction losses and benefiting from the increased reflectivity of the surrounding environment.

The growing interest in vertical bifacial systems for Nordic applications was further consolidated by the review work of Jouttijärvi et al. [50], which examined the opportunities and challenges associated with vertically mounted bifacial photovoltaics in high-latitude regions from both modelling and application perspectives. The authors highlighted that the low average solar altitude characteristic of Nordic countries allows vertical east–west bifacial systems to effectively harvest both morning and evening solar radiation, producing a daily generation profile substantially different from that of conventional south-facing rooftop installations. Instead of concentrating electricity production around solar noon, vertical bifacial systems were shown to produce two broader generation peaks, improving the temporal match between photovoltaic production and typical residential electricity demand. The review also discussed the importance of local diffuse radiation conditions, ground reflectance, and urban integration strategies, emphasizing how the interaction between photovoltaic systems and the surrounding built environment becomes particularly relevant for façade-integrated applications. In addition, the study identified several practical advantages associated with vertical mounting, including reduced snow accumulation and lower soiling losses compared to tilted rooftop systems.

More recent investigations extended these considerations to real building-scale urban applications. Jouttijärvi et al. [54] investigated innovative façade-mounted photovoltaic solutions for apartment buildings in Finland, comparing rooftop systems with several vertical bifacial façade configurations under realistic urban conditions. The study analyzed the influence of façade orientation, shading scenarios, and electricity-sharing strategies using real residential load profiles and local climatic data. Their results showed that vertical bifacial façade systems can improve load matching and increase the value of the generated electricity by distributing production more evenly throughout the day. The authors also observed that moderate urban shading produced relatively limited reductions in annual energy yield, while non-optimal building orientation had a smaller impact on system performance than typically expected. The work further emphasized the importance of façade-integrated photovoltaics for high-rise residential buildings, where façade surfaces may provide significantly larger usable areas than rooftops for local renewable electricity generation.

Overall, the existing literature consistently indicates that vertical bifacial photovoltaic systems may become particularly advantageous in Nordic and high-latitude environments due to the combined effects of low solar elevation, enhanced diffuse irradiance, and snow-induced albedo. At the same time, previous studies also demonstrate that the performance of bifacial façade systems strongly depends on urban geometry, surrounding reflectivity, façade orientation, and the complex spatial distribution of rear-side irradiance. Consequently, the accurate assessment of bifacial BIPV systems in northern climates requires modelling approaches capable of capturing both the optical and environmental interactions that characterize façade-integrated photovoltaic applications.

1.7 Research gaps and motivation

The literature reviewed in the previous sections demonstrates the growing interest in bifacial photovoltaic technologies and their integration into building envelopes, particularly in high-latitude regions where vertical configurations can benefit from diffuse radiation and seasonal high-albedo conditions. Several studies have shown that bifacial systems may achieve significant energy gains compared to conventional monofacial solutions, especially when installed in vertical or façade-integrated configurations under Nordic climatic conditions. Furthermore, previous investigations highlighted the importance of rear-side irradiance, surrounding reflectivity, and module operating temperature in determining the overall performance of bifacial photovoltaic systems. [50, 1]

Despite these advances, important limitations still remain in the current literature. First, most studies on bifacial photovoltaics focus either on utility-scale installations or rooftop applications, while comparatively fewer investigations address bifacial BIPV façades. In particular, ventilated bifacial façade systems operating under realistic Nordic climatic conditions remain insufficiently explored. Existing studies often analyse electrical performance and bifacial gain without considering the coupled thermal and fluid-dynamic phenomena occurring within the ventilated cavity behind the modules.

Another important limitation concerns the modelling approach adopted in previous studies. Optical and thermal analyses are frequently treated separately, with limited integration between irradiance prediction and thermo-fluid dynamic modelling. Several investigations rely on simplified thermal boundary conditions, such as uniform heat fluxes, constant wall temperatures, or spatially uniform irradiance distributions. However, in façade-integrated bifacial systems, the thermal behaviour strongly depends on the local distribution of absorbed solar radiation, the conductive response of the building envelope, and the buoyancy-driven airflow developing within the air cavity. Neglecting these coupled interactions may lead to inaccurate predictions of module operating temperatures and cooling performance.

The modelling of rear-side irradiance also remains a significant challenge in bifacial BIPV applications. Previous studies identified the non-uniform distribution of rear irradiance as one of the major unresolved issues limiting the accurate assessment of bifacial systems integrated into buildings. [1] While several optical models have been developed to estimate bifacial gain and rear irradiance contributions, the resulting non-uniform radiative loads are rarely transferred into detailed thermal simulations of ventilated façades. Consequently, the influence of spatially varying irradiance on local temperature fields and natural convection patterns inside the cavity is still not fully understood.

In addition, the optimization of the air gap in ventilated bifacial façades has received limited attention in the existing literature. Although the cavity thickness plays a key role in determining airflow development, heat removal capability, and module cooling effectiveness, many studies assume fixed geometrical configurations without investigating the thermo-fluid dynamic implications of different air-gap dimensions. This aspect becomes particularly relevant for vertical bifacial systems, where natural convection inside the cavity directly affects photovoltaic operating temperatures and therefore electrical efficiency.

Finally, many previous investigations employ simplified climatic assumptions or constant albedo values, despite the strong seasonal variability characterizing Nordic environments. In high-latitude regions, snow cover, diffuse radiation, and changing surface reflectivity can substantially modify both front-side and rear-side irradiance conditions throughout the year. Therefore, realistic climate-based modelling approaches are required in order to accurately describe the coupled optical and thermal behaviour of bifacial BIPV systems operating in these contexts.

In light of these research gaps, there is a clear need for integrated modelling methodologies capable of coupling realistic optical calculations with detailed thermo-fluid dynamic simulations for ventilated bifacial BIPV façades under Nordic climatic conditions. Such approaches are necessary to improve the understanding of the interactions between irradiance distribution, wall heat transfer, cavity airflow, and photovoltaic operating temperature, ultimately supporting the optimization and design of high-performance bifacial façade systems.

Chapter 2

Optical and Electrical Model

2.1 Overview and objectives

The first phase of the present work concerns the development of a coupled optical and electrical model for a building-integrated bifacial photovoltaic (BIPV) system mounted on a vertical, south-facing façade in Helsinki, Finland. The model computes the solar irradiance incident on both the front and the rear surface of three bifacial glass–glass modules arranged at different heights along the façade, and from these it estimates the operating temperature, the electrical power output and the bifacial gain of each module over a full year of operation.

The distinguishing feature of a building-integrated bifacial array, relative to a free-standing one, is that the rear surface of the modules faces a nearby opaque wall across a narrow ventilated cavity. The rear-side irradiance is therefore governed not only by the sky and the ground, but predominantly by the radiation exchanged with the wall, and it varies with the vertical position of each module along the façade. Reproducing this position-dependent rear-side irradiance is the central objective of the optical model. The specific aims of this phase are:

1. to quantify the front-side irradiance by means of an established sky-diffuse transposition model adapted to the vertical façade geometry;
2. to formulate a view-factor-based description of the rear-side irradiance that explicitly accounts for the vertical position of each module;
3. to estimate the module operating temperature through a lumped steady-state thermal balance;
4. to evaluate the electrical output in both monofacial and bifacial configurations, thereby quantifying the bifacial gain associated with each module position and seasonal condition; and
5. to provide, for a set of representative operating conditions, the absorbed solar loads that serve as boundary conditions for the CFD thermal model of Chapter 3.

The model is implemented in Python. Solar geometry and the transposition of the measured irradiance onto the plane of the array are handled through the `pvlib` library [18], whereas the rear-side irradiance is reconstructed from a geometric, view-factor-based decomposition into sky, ground and wall contributions developed specifically in this work. The meteorological boundary conditions are taken from one-minute measurements of the Finnish Meteorological Institute (FMI) station at Helsinki Kumpula (station ID 101004) for the year 2021. The overall thermal–electrical framework follows the approach of Tina et al. [19], while the treatment of the rear-side irradiance is extended here to resolve the effect of vertical module position, which the reference formulation does not capture.

2.2 System description

2.2.1 Façade configuration

The system consists of three bifacial glass–glass modules based on n-type TOPCon cell technology (Leapton LP182×210-M-54-NB, nominal power 500 W, bifaciality factor 0.80), mounted contiguously in a vertical column on a south-facing building façade. The modules are separated from the building wall by a ventilated air cavity of width d, which provides natural (buoyancy-driven) ventilation of the gap. Unless otherwise stated, the optical–electrical results reported in this chapter refer to a baseline cavity depth of $d = 0.15\,\text{m}$; the influence of the cavity width is subsequently assessed over the range 0.10 m to 0.50 m to support the selection of an optimal geometry for the CFD analysis of Chapter 3.

2.2.2 System geometry

The geometric parameters of the system are summarised in Table 2.1 and illustrated in Figure 2.1.

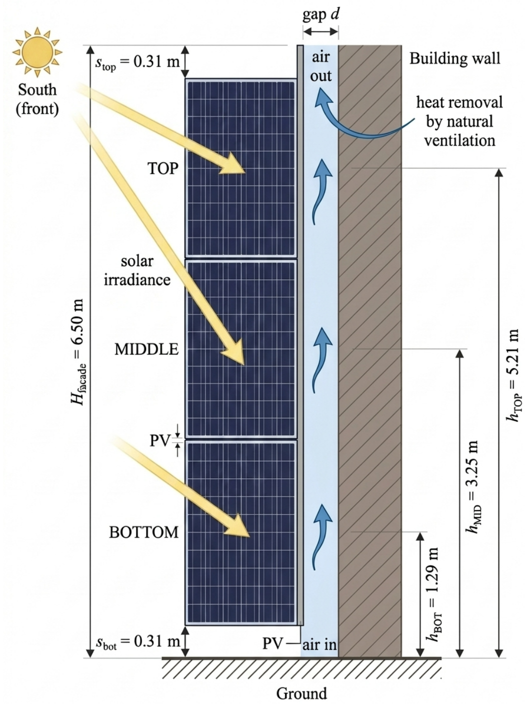

Figure 2.1: Cross-section of the vertical BIPV façade. Three bifacial modules (TOP, MIDDLE, BOTTOM) are stacked in a contiguous column on the south-facing façade, separated from the building wall by a ventilated air gap of width d. The centre heights of the modules and the overall façade height are indicated (generated using FigureLabs).

The three modules are stacked without vertical spacing between them and the array is centred on the façade, leaving equal free strips of height $s_{\text{top}} = s_{\text{bot}}$ above the top module and below the bottom module. Taking the ground as the vertical origin, the height of the centre of each module is

$$h_{\text{TOP}} = H_{\text{fac}} - s_{\text{top}} - \frac{H_{\text{pan}}}{2} = 6.50 - 0.31 - 0.98 = 5.21\,\text{m}, \tag{2.1}$$

$$h_{\text{MID}} = \frac{H_{\text{fac}}}{2} = 3.25\,\text{m}, \tag{2.2}$$

$$h_{\text{BOT}} = s_{\text{bot}} + \frac{H_{\text{pan}}}{2} = 0.31 + 0.98 = 1.29\,\text{m}. \tag{2.3}$$

These centre heights determine the angular extent of sky and ground seen by the rear of each module and are therefore the primary geometric input to the view-factor calculation of Section 2.4.2. The front surface of the array is vertical (tilt $\beta = 90°$) and faces due south (azimuth $\gamma = 180°$), consistent with a façade-integrated installation.

Table 2.1: System geometry parameters.

Parameter	Symbol	Value	Unit
Façade height	H_{fac}	6.50	m
Panel height	H_{pan}	1.961	m
Panel width	W_{pan}	1.134	m
Panel area	A_{pan}	2.224	m^2
Free space above	s_{top}	0.31	m
Free space below	s_{bot}	0.31	m
Air gap (baseline)	d	0.15	m
Façade tilt	β	90	$^\circ$
Façade azimuth	γ	180	$^\circ$

2.3 Model assumptions

The optical–electrical model relies on a set of simplifying assumptions, stated and justified below. They are grouped into geometric, optical, thermal and electrical assumptions, and are referenced throughout the remainder of this section.

2.3.1 Geometric assumptions

A1) Two-dimensional, horizontally infinite façade. The façade is treated as invariant and unbounded in the horizontal direction, so that edge effects at the lateral borders of the array are neglected and the problem reduces to the vertical plane. This is consistent with a façade composed of many identical columns of modules placed side by side, of which a single representative column is modelled.

A2) Panels represented at their mid-height. The view factors of each module are evaluated at the height of its geometric centre, rather than integrated over the module surface. Because the view factors vary smoothly with height, the mid-height value is representative of the module average; the upper module, which experiences the largest vertical gradient, is additionally subdivided into three segments (Section 2.6.4) to resolve this variation where it is most pronounced.

A3) Contiguous, coplanar array. The three modules are coplanar and stacked without vertical gaps between them, forming a continuous PV surface of height $3\,H_{\text{pan}}$ centred on the façade.

A4) Uniform air-gap width. The cavity depth d between the rear of the modules and the wall is constant over the whole façade height, so that the wall and the array are parallel planes.

2.3.2 Optical assumptions

A5) Isotropic surfaces for reflected and diffuse radiation. The sky, the ground and the wall are treated as isotropic (Lambertian) sources of diffuse and reflected radiation. Their contributions to the rear-side irradiance are therefore fully described by the corresponding view factors, without angular dependence.

A6) First-order reflections only. Only single reflections from the ground and the wall are considered; multiple inter-reflections between the wall, the ground and the module rear surface are neglected. Given the low reflectances involved and the dominance of the direct wall contribution, higher-order terms are a second-order effect.

A7) Diffuse, grey wall reflectance. The building wall is characterised by a single, wavelength-independent (grey) diffuse reflectance $\rho_{\text{wall}} = 0.30$, representative of a conventional light-coloured rendered façade.

A8) Monthly ground albedo. The ground albedo is prescribed on a monthly basis from ERA5 reanalysis data (Table 2.5), in order to represent the strong seasonal variation associated with snow cover at the Helsinki site. A constant annual albedo would not capture the enhanced ground-reflected contribution during the winter months.

A9) Constant glass transmittance. The glass transmittance is taken as a constant $\tau_{\text{glass}} = 0.90$, independent of the angle of incidence. The fraction of radiation transmitted through the inactive area of the module and reaching the wall is $\tau_{\text{glass}}(1 - \text{PF})$, with the packing factor $\text{PF} = 0.928$ computed from the cell layout of the module.

A10) Front-side transposition. The plane-of-array front irradiance is obtained from the measured global, direct and diffuse components through the transposition model implemented in `pvlib` [18], applied to the vertical, south-facing plane.

2.3.3 Thermal assumptions

A11) Lumped, steady-state module temperature. In the optical–electrical model the module operating temperature is obtained from a lumped steady-state energy balance, following the empirical correlation of Tina et al. [19]. Thermal capacitance and transient effects are neglected, consistent with the use of hourly-representative operating points. The detailed temperature field and the ventilated-cavity heat transfer are resolved separately in the CFD model of Chapter 3.

A12) Wind-dependent heat-transfer coefficients. The heat-loss coefficients of the temperature correlation, $U_0 = 25$ and $U_1 = 1.2$, are taken from Tina et al. [19], with U_1 scaling the convective loss linearly with the measured wind speed.

A13) Sky temperature from the Swinbank relation. The effective sky temperature used for the long-wave radiative exchange is estimated from the ambient temperature through the Swinbank correlation [72].

2.3.4 Electrical assumptions

A14) Linear temperature derating of efficiency. The module efficiency is corrected linearly with temperature, $\eta = \eta_{\mathrm{STC}} [1 - \beta_0 (T_{\mathrm{pv}} - 25)]$, with $\eta_{\mathrm{STC}} = 0.2248$ and temperature coefficient $\beta_0 = 0.0030\,\mathrm{K}^{-1}$, from the module datasheet.

A15) Constant bifaciality factor. The rear-side response is scaled by a constant bifaciality factor BF = 0.80, independent of irradiance level and angle of incidence.

A16) Uniform illumination of each module (or segment). Within each module — or, for the upper module, within each of its three segments — the front and rear irradiance are assumed uniform, and mismatch losses between cells are not modelled.

A17) Absorption of the active area. The absorbed solar load is computed from an absorptance $\alpha_{\mathrm{abs}} = 0.90$ applied to the active (cell-covered) fraction of the module, quantified by the packing factor.

A18) No electrical or system losses. Inverter, wiring and other balance-of-system losses are not included; the reported quantities refer to the DC output at module level, so that the comparison between positions and configurations is not affected by system-level assumptions.

2.4 Mathematical formulation

The optical–electrical model proceeds in five stages: (i) the solar position and the front-side irradiance are evaluated from the measured meteorological data; (ii) the position-dependent view factors are computed; (iii) the rear-side irradiance is reconstructed as a weighted sum of sky, ground and wall contributions; (iv) the module operating temperature is obtained from a lumped thermal balance; and (v) the electrical output and the bifacial gain are derived. Each stage is described below.

2.4.1 Front-side irradiance

The solar position (zenith and azimuth) is computed from the site coordinates and the timestamp of each one-minute record using `pvlib` [18]. The global tilted irradiance on the vertical, south-facing plane of the array, G_{front}, is then obtained by transposition of the measured global horizontal (GHI), direct and diffuse horizontal components onto the plane of array, accounting for the beam, sky-diffuse and ground-reflected contributions. The transposition is evaluated for a tilt $\beta = 90°$ and an azimuth $\gamma = 180°$, using the monthly ground albedo of Table 2.5.

A fraction of the front irradiance is transmitted through the transparent inactive area of the glass–glass module and reaches the wall behind the array. This transmitted irradiance is

$$G_{\text{wall,tr}} = G_{\text{front}}\, \tau_{\text{glass}}\, (1 - PF), \tag{2.4}$$

where $\tau_{\text{glass}} = 0.90$ is the glass transmittance and $PF = 0.928$ is the packing factor of the module. The term $G_{\text{wall,tr}}$ represents only the portion of front-side irradiance transmitted through the inactive glass area and reaching the wall; it does not represent the total irradiance incident on the wall.

2.4.2 View factors

The rear surface of each module exchanges diffuse radiation with three surfaces: the sky, the ground and the building wall. Because the array and the wall form two parallel planes separated by the narrow gap d, the portion of sky and ground seen by the rear of a module depends on its height along the façade. For a module whose centre is at height h on a façade of height H_{fac}, the sky and ground view factors are evaluated from the angles subtended, through the gap, by the façade portion above and below the module:

$$F_{\text{sky}} = \frac{1}{2}\big(1 - \cos\alpha\big), \qquad \alpha = \arctan\!\left(\frac{d}{H_{\text{fac}} - h}\right), \tag{2.5}$$

$$F_{\text{grd}} = \frac{1}{2}\big(1 - \cos\beta_g\big), \qquad \beta_g = \arctan\!\left(\frac{d}{h}\right), \tag{2.6}$$

and the remaining fraction of the hemisphere is attributed to the wall, so that the view factors sum to unity:

$$F_{\text{wall}} = 1 - F_{\text{sky}} - F_{\text{grd}}. \tag{2.7}$$

Table 2.2: View factors between the rear side of each module and the sky, ground and wall for the baseline air gap $d = 0.15\,\mathrm{m}$.

Position	h [m]	F_{sky}	F_{grd}	F_{wall}
TOP	5.21	0.00335	0.00021	0.99644
MIDDLE	3.25	0.00053	0.00053	0.99894
BOTTOM	1.29	0.00021	0.00335	0.99644

Equations (2.5)–(2.7) show that a module located higher on the façade sees a larger portion of sky and a smaller portion of ground, and vice versa. Because the gap d is small compared with the façade height, the angles α and β_g are small and the wall dominates the rear field of view; as the gap widens, the sky and ground fractions grow at the expense of the wall. The resulting view factors for the baseline gap are reported in Table 2.2.

2.4.3 Rear-side irradiance

The rear-side irradiance of each module is reconstructed as the sum of the three contributions, each weighted by its view factor:

$$G_{\mathrm{rear}} = \underbrace{D\,F_{\mathrm{sky}}}_{\mathrm{sky}} + \underbrace{G\,\rho_{\mathrm{grd}}\,F_{\mathrm{grd}}}_{\mathrm{ground}} + \underbrace{G_{\mathrm{wall,tr}}\,\rho_{\mathrm{wall}}\,F_{\mathrm{wall}}}_{\mathrm{wall}}, \tag{2.8}$$

where D is the diffuse horizontal irradiance, G the global horizontal irradiance, ρ_{grd} the monthly ground albedo, $\rho_{\mathrm{wall}} = 0.30$ the wall reflectance, and $G_{\mathrm{wall,tr}}$ the irradiance transmitted through the inactive glass area of the module and reaching the wall. The first term represents the diffuse radiation from the sky reaching the rear side through the gap, the second term represents the ground-reflected radiation, and the third term represents the wall-reflected contribution generated by the portion of front-side irradiance transmitted through the module (Eq. 2.4). The wall term is dominant for the narrow gaps of interest, in accordance with the view factors of Table 2.2.

2.4.4 Module temperature

The module operating temperature is estimated from a lumped steady-state balance between the absorbed solar radiation and the convective and radiative losses, following Tina et al. [19]:

$$T_{\mathrm{pv}} = T_{\mathrm{air}} + \frac{G_{\mathrm{front}}\,(1-\eta_{\mathrm{STC}})}{U_0 + U_1\,v_{\mathrm{w}}}, \tag{2.9}$$

where T_{air} is the ambient temperature, v_{w} the wind speed, and $U_0 = 25$, $U_1 = 1.2$ the heat-loss coefficients of the correlation. The effective sky temperature governing the long-wave radiative exchange is obtained from the ambient temperature through the Swinbank relation.

2.4.5 Electrical output and bifacial gain

The temperature-corrected efficiency follows a linear derating law,

$$\eta = \eta_{STC} \left[1 - \beta_0 \left(T_{PV} - 25\right)\right]$$

where $\eta_{STC} = 0.2248$ and $\beta_0 = 0.0030$ K^{-1}. In this expression, T_{PV} is expressed in degrees Celsius.

The monofacial and bifacial electrical power outputs are calculated as

$$P_{mono} = \eta(T_{PV}) G_{front} A_{pan}$$

and

$$P_{bif} = \eta(T_{PV}) \left(G_{front} + BF\, G_{rear}\right) A_{pan}$$

where A_{pan} is the total module aperture area and BF is the bifaciality factor. The packing factor is not included in the electrical power equations because the module efficiency reported in the datasheet is already defined with respect to the total module area. Therefore, including PF in these equations would double-count the inactive module fraction.

The bifacial gain is then computed as

$$BG = \frac{P_{bif} - P_{mono}}{P_{mono}} = \frac{BF\, G_{rear}}{G_{front}}$$

2.4.6 Coupling to the CFD model

For the representative operating points used in the thermal analysis, the absorbed solar radiation is converted into the volumetric heat sources that drive the CFD model of Chapter 3. The absorbed front and rear heat fluxes are

$$q''_{\text{front}} = G_{\text{front}}\, \alpha_{\text{abs}}\, \text{PF}\, (1 - \eta), \qquad q''_{\text{rear}} = G_{\text{rear}}\, \alpha_{\text{abs}}\, \text{PF}\, (1 - \text{BF}\, \eta), \tag{2.10}$$

with $\alpha_{\mathrm{abs}} = 0.90$ the absorptance. The corresponding volumetric source in the PV solid, of thickness t_{PV}, is $S_{\mathrm{PV}} = (q''_{\mathrm{front}} + q''_{\mathrm{rear}})/t_{\mathrm{PV}}$, evaluated separately for each vertical band of the array. Likewise, the irradiance transmitted to the wall defines a volumetric source in the wall solid,

$$S_{\mathrm{wall}} = \frac{G_{\mathrm{wall,tr}}\,\alpha_{\mathrm{wall}}}{t_{\mathrm{wall}}}, \tag{2.11}$$

with $\alpha_{\mathrm{wall}} = 1 - \rho_{\mathrm{wall}}$. Long-wave radiative losses are not subtracted from the absorbed heat fluxes at this stage, because radiative exchange is resolved explicitly in the CFD model through the Surface-to-Surface radiation model. These band-wise sources, evaluated at the peak-irradiance hour of each seasonal design day and for each gap width, constitute the boundary conditions of the CFD model.

2.5 Input data and parameters

This section collects the meteorological data, the material and optical properties, and the wall construction used as input to the model. The module and optical parameters are summarised in Table 2.3, while the wall stratigraphy and the seasonal ground albedo are described in the following subsections.

2.5.1 Meteorological data

The meteorological boundary conditions are taken from the Finnish Meteorological Institute (FMI) open-data station at Helsinki Kumpula (station ID 101004, latitude 60.18°N), for the reference year 2021 at a temporal resolution of one minute [66]. The measured quantities used by the model are the global, direct and diffuse horizontal irradiance, the ambient air temperature and the wind speed. Records with a global horizontal irradiance below $5\,\mathrm{W\,m^{-2}}$ are discarded, so that only daylight conditions contribute to the analysis.

2.5.2 Module and optical parameters

The photovoltaic module is a Leapton LP182×210-M-54-NB bifacial glass–glass unit based on n-type TOPCon technology. Its electrical and optical parameters are listed in Table 2.3. The efficiency, bifaciality factor and temperature coefficient are taken from the manufacturer datasheet [67]. The heat-loss coefficients U_0 and U_1 of the temperature correlation follow Tina et al. [19].

The packing factor PF was computed as the ratio between the active photovoltaic cell area and the total module aperture area:

$$\mathrm{PF} = \frac{A_{\mathrm{cells}}}{A_{\mathrm{pan}}} = \frac{54 \cdot 0.182 \cdot 0.210}{1.961 \cdot 1.134} \approx 0.928. \tag{2.12}$$

Here, the 108 half-cells reported in the module datasheet are treated as 54 equivalent full cells. The packing factor therefore represents the fraction of the module aperture area covered by active photovoltaic cells, while the remaining fraction $1 - \mathrm{PF}$ corresponds to the optically inactive glass area.

Table 2.3: Module, optical and thermal parameters of the model.

Parameter	Symbol	Value	Source
STC efficiency	η_{STC}	0.2248	datasheet [67]
Temperature coefficient	β_0	0.0030	datasheet [67]
Bifaciality factor	BF	0.80	datasheet [67]
Packing factor	PF	0.928	computed
Glass transmittance	τ_{glass}	0.90	assumed
Absorptance	α_{abs}	0.90	assumed
Wall reflectance	ρ_{wall}	0.30	assumed
Loss coefficient	U_0	25	[19]
Wind loss coefficient	U_1	1.2	[19]

The values of glass transmittance, photovoltaic absorptance and wall reflectance were introduced as modelling assumptions representative of the materials considered in this study. The glass transmittance was set to $\tau_{\mathrm{glass}} = 0.90$, consistently with the use of a thin anti-reflective photovoltaic glass and with the order of magnitude of solar transmittance values reported for glass materials by Incropera et al. [68]. The absorptance of the active photovoltaic area was assumed equal to $\alpha_{\mathrm{abs}} = 0.90$, representative of a dark solar-absorbing surface; this value is consistent with the high solar absorptances reported for black absorbing materials in radiative heat-transfer data [68]. Finally, the wall reflectance was assumed equal to $\rho_{\mathrm{wall}} = 0.30$, corresponding to a solar absorptance of $\alpha_{\mathrm{wall}} = 1 - \rho_{\mathrm{wall}} = 0.70$, and was adopted as a representative value for a moderately absorbing building façade. These parameters should therefore be interpreted as physically plausible reference values rather than as experimentally measured properties of the specific façade materials.

2.5.3 Building wall

The building wall behind the array is a multilayer construction designed to be representative of a well-insulated Finnish building envelope. Its overall thermal transmittance is close to the reference wall value of $0.17\,\mathrm{W\,m^{-2}\,K^{-1}}$ reported in Decree 1010/2017 of the Finnish Ministry of the Environment on the energy performance of new buildings [69]. The layer sequence, from the exterior to the interior, together with the thickness s_i and thermal conductivity k_i of each layer, is reported in Table 2.4 and illustrated in Figure 2.2. The thermal conductivities of the individual materials are taken from Incropera et al. [68].

The overall thermal resistance and transmittance of the wall are obtained from the series of the layer resistances,

$$R_{\text{wall}} = \sum_i \frac{s_i}{k_i} = 5.95\,\text{m}^2\,\text{K}\,\text{W}^{-1}, \qquad U_{\text{wall}} = \frac{1}{R_{\text{wall}}} = 0.168\,\text{W}\,\text{m}^{-2}\,\text{K}^{-1}, \tag{2.13}$$

for a total wall thickness of $t_{\text{wall}} = 0.3832\,\text{m}$. The resulting transmittance is representative of a well-insulated envelope for the Nordic climate. In the CFD model, this multilayer wall is represented by an equivalent homogeneous solid with a conductivity $k_{\text{eq}} = t_{\text{wall}}/R_{\text{wall}} = 0.0644\,\text{W}\,\text{m}^{-1}\,\text{K}^{-1}$, which reproduces the same overall transmittance while avoiding the explicit discretisation of the individual layers; its density and specific heat are taken as the thickness-weighted averages of the layer properties.

Table 2.4: Wall stratigraphy (exterior to interior) and layer properties.

Layer	Material	s_i [m]	k_i [W m^{-1}K^{-1}]	Source
1	Plaster (exterior)	0.010	0.70	[68]
2	Concrete	0.150	0.72	[68]
3	Mineral wool	0.210	0.037	[68]
4	Moisture barrier	0.0002	0.50	[68]
5	Gypsum board (interior)	0.013	0.25	[68]
Total / equivalent		0.3832	0.0644 (eq.)	

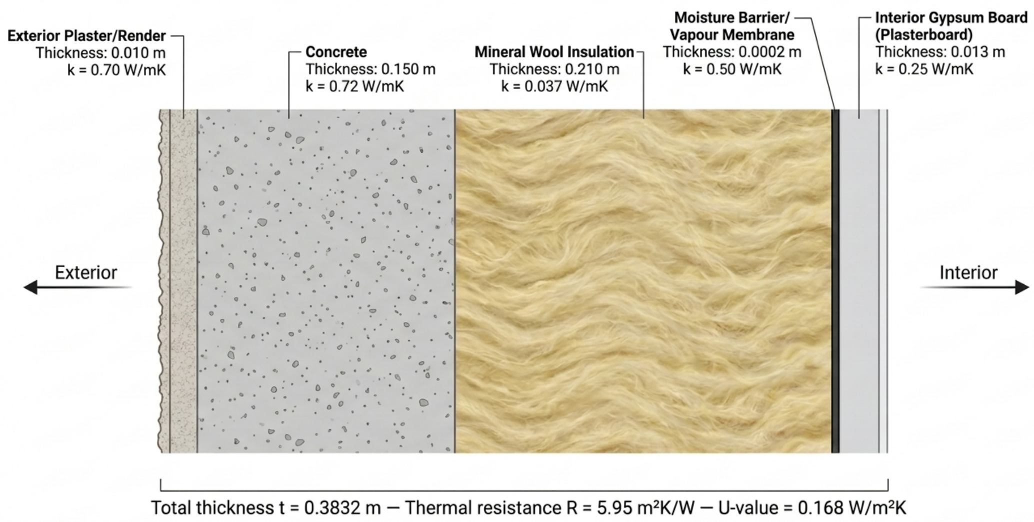

Figure 2.2: Stratigraphy of the multilayer building wall, from the exterior plaster layer to the interior gypsum board. The equivalent homogeneous wall used in the CFD model preserves the same overall thermal resistance (generated using FigureLabs).

2.5.4 Ground albedo

The ground albedo is prescribed on a monthly basis from ERA5 reanalysis data [70], as reported in Table 2.5. The strong seasonal variation is characteristic of the Nordic site: the albedo exceeds 0.5 during the winter months, when the ground is snow-covered, and falls to about 0.11 in summer. This variation directly affects the ground-reflected contribution to the rear-side irradiance (Eq. 2.8), and its explicit monthly representation is therefore essential for a realistic estimate of the bifacial gain at this location.

Table 2.5: Monthly ground albedo from ERA5 reanalysis data for Helsinki Kumpula in 2021.

Month	Jan	Feb	Mar	Apr	May	Jun	Jul	Aug	Sep	Oct	Nov	Dec
ρ_{grd}	0.534	0.526	0.429	0.119	0.118	0.128	0.132	0.121	0.111	0.104	0.218	0.275

2.6 Results

The optical–electrical model was run over the full year 2021 for the three modules and, for the upper module, for its three vertical segments. This section reports the annual and seasonal results; their physical interpretation is deferred to the discussion of Section 2.7. For annual, monthly and daily results, the bifacial gain is evaluated from the corresponding energy yields:

$$BG = \frac{E_{\text{bif}} - E_{\text{mono}}}{E_{\text{mono}}} \cdot 100. \tag{2.14}$$

This definition represents the effective energy benefit of bifacial operation over the considered time period and avoids averaging instantaneous gain values.

2.6.1 Annual results

The annual results for the three module positions are summarised in Table 2.6. The three modules yield an identical annual monofacial energy of 410.10 kWh, while the bifacial energy ranges from 423.50 kWh for the middle module to 424.82 kWh for the top module. The corresponding additional energy production is between 13.40 kWh and 14.72 kWh.

For consistency with the definition introduced above, the bifacial gain reported in the table is calculated from the annual energy yields. The mean rear-side irradiance lies between 7.83 and 8.09 W m^{-2}, and the annual mean module temperature is 15.3°C for all three positions. The bifacial gain ranges from 3.298% for the middle module to 4.006% for the top module.

Table 2.6: Annual results for the three module positions, Helsinki Kumpula 2021.

Position	E_{mono} [kWh]	E_{bif} [kWh]	Gain [kWh]	BG [%]	G_{rear} [W m^{-2}]	T_{pv} [°C]
TOP	410.10	424.82	14.72	4.006	8.09	15.3
MIDDLE	410.10	423.50	13.40	3.298	7.83	15.3
BOTTOM	410.10	423.60	13.49	3.326	7.88	15.3

2.6.2 Monthly behaviour

Figure 2.3 presents four complementary views of the annual optical–electrical behaviour: the monthly energy yield, the monthly bifacial gain by position, the mean rear-side irradiance together with the ground albedo, and the daily bifacial energy over the year.

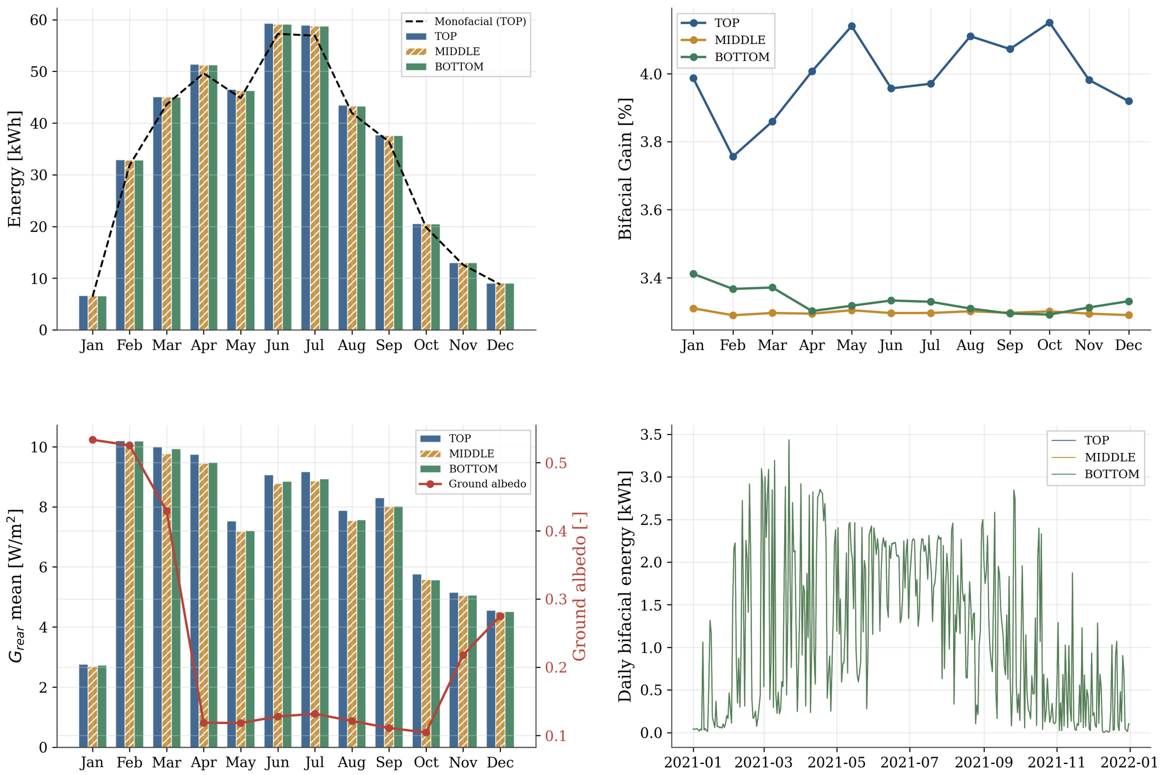

Figure 2.3: Overview of the annual optical–electrical results for Helsinki Kumpula 2021: (top left) monthly energy yield in the monofacial and bifacial cases for the three positions; (top right) monthly bifacial gain by position; (bottom left) mean rear-side irradiance and monthly ground albedo; (bottom right) daily bifacial energy over the year.

The monthly energy yield (top left) follows the seasonal cycle of the high-latitude solar resource, rising steeply from a minimum of about 6 kW h in January to a maximum of roughly 59 kW h in June and July; the bifacial bars remain marginally above the monofacial reference in every month. The monthly bifacial gain (top right) is highest for the top module throughout the year, ranging between about 3.76 % in February and 4.15 % in May and October, and lowest for the middle module, which stays close to 3.28 % with little seasonal variation; the bottom module lies in between, ranging from about 3.2 % in summer to 3.4 % in winter. The mean rear-side irradiance (bottom left) is largest in the winter and spring months, when the ground albedo, overlaid on the same axis, is highest owing to snow cover, and decreases through the summer as the albedo drops. Finally, the daily bifacial energy (bottom right) confirms the strong seasonal envelope, with the highest daily yields concentrated between March and September.

2.6.3 Decomposition of the rear-side irradiance

The three contributions to the rear-side irradiance (sky-diffuse, ground-reflected and wall-reflected) are separated in Figure 2.4 for the top module. The wall-reflected term is the dominant contribution in every month of the year, accounting for about 94-98% of the total rear-side irradiance. The sky-diffuse term represents most of the remaining contribution, whereas the ground-reflected term is negligible at the scale of the total rear-side irradiance.

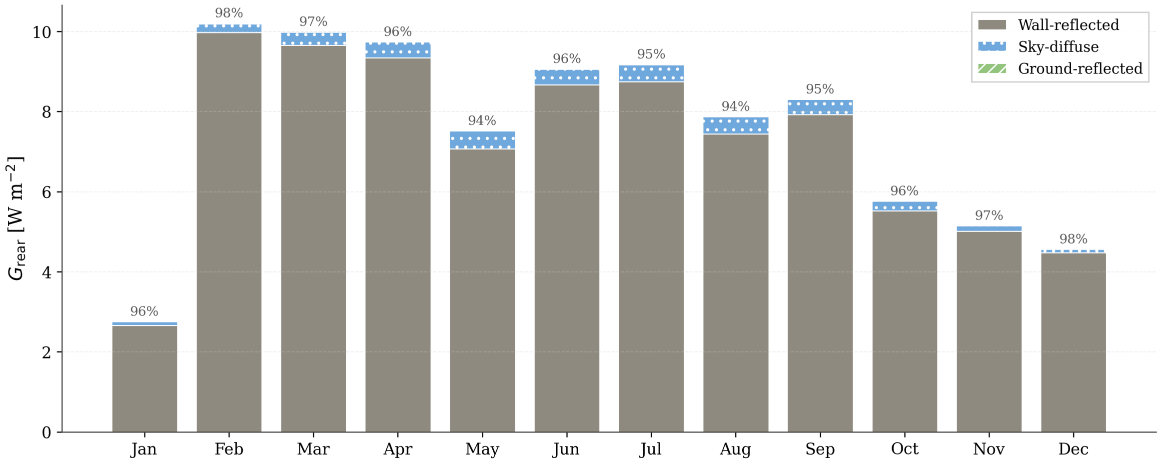

Figure 2.4: Decomposition of the monthly mean rear-side irradiance of the top module into wall-reflected, sky-diffuse and ground-reflected contributions.

2.6.4 Vertical segmentation of the top module

The rear-side irradiance of the three vertical segments of the upper module (upper, middle and lower) is shown in Figure 2.5. The upper segment receives systematically the highest rear-side irradiance, and the spread between the segments is largest in the months of high diffuse irradiance. These height-resolved values provide the piecewise-in-height source applied in the CFD model (Chapter 3).

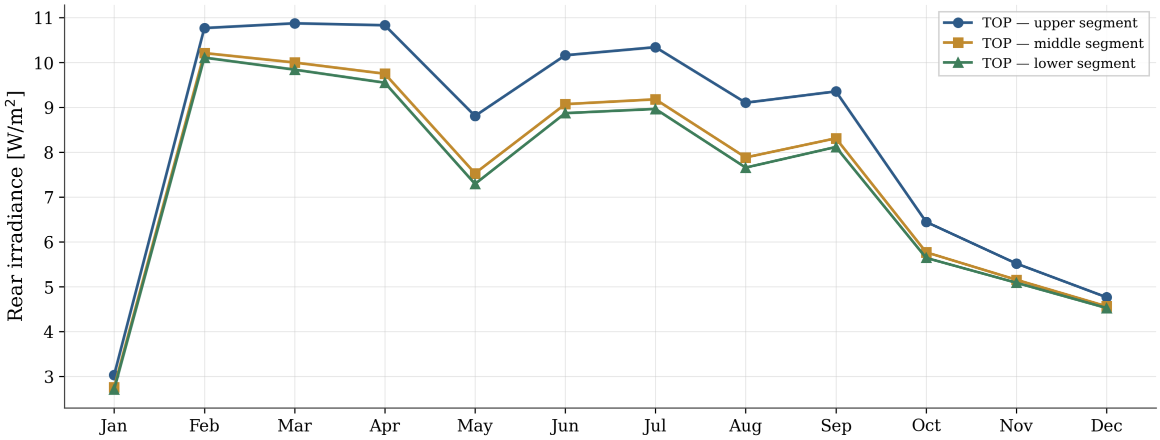

Figure 2.5: Monthly mean rear-side irradiance of the three vertical segments of the top module (upper, middle, lower).

2.6.5 Ground-albedo analysis

Figure 2.6 reports the monthly ERA5 ground albedo (left) and the seasonal distribution of the ground-reflected contribution to the rear-side irradiance of the top module (right). The ground albedo (left) exceeds 0.5 in January and February, decreases to about 0.43 in March, drops to about 0.10-0.13 from April to October, and rises again through November (about 0.22) and December (about 0.28). The ground-reflected contribution to G_{rear} (right), however, does not follow the albedo alone: it is highest in spring and summer, with mean values of about 0.0095 and 0.0090 W m^{-2} respectively, despite the much lower albedo in these seasons, because the higher incident irradiance more than compensates the reduced ground reflectivity. Winter shows an intermediate contribution (mean about 0.0072 W m^{-2}) despite having the highest albedo, reflecting the low incident irradiance at this latitude in that period, while autumn shows the lowest contribution (mean about 0.0035 W m^{-2}), combining moderate irradiance with low albedo.

2.6.6 Representative design days

Five representative days are selected to characterise the system across the seasons and to define the operating points subsequently used in the CFD analysis. Four of them correspond to the canonical astronomical dates (the winter solstice (21 December), the spring equinox (20 March), the summer solstice (21 June) and the autumn equinox (22 September)) which together span the full range of solar elevation and day length over the year. The spring equinox of 2021, however, was an overcast day, representative of diffuse-dominated conditions but not of the high-irradiance regime that produces the largest thermal loads. To ensure that the design set also includes a clear-sky, high-load

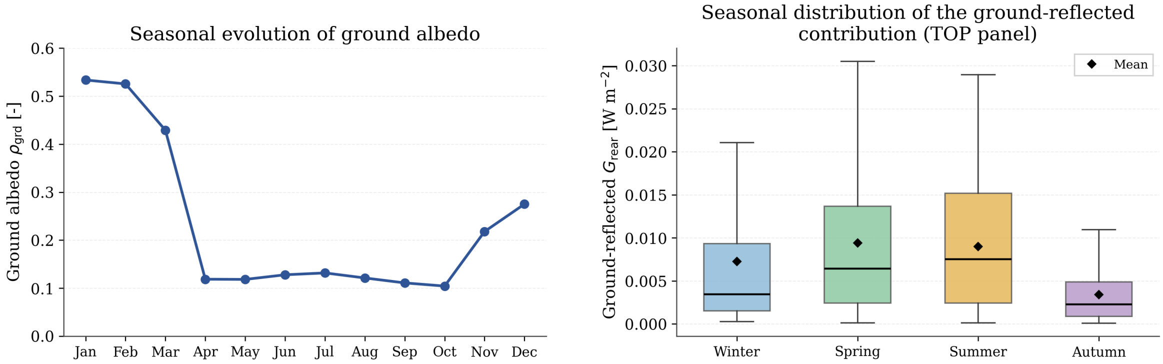

Figure 2.6: Ground-albedo analysis for Helsinki Kumpula 2021, showing the monthly ERA5 ground albedo and the seasonal distribution of the ground-reflected contribution to the rear-side irradiance of the top module.

condition in the intermediate season, a fifth day is added: a clear day close to the spring equinox (22 March). The two March days thus bracket the range of sky conditions in the intermediate season, fully overcast on 20 March and clear on 22 March, which is particularly relevant for the subsequent thermal analysis, where the clear day represents a near-worst-case load for the ventilated cavity. The statistics of the five design days for the top module are summarised in Table 2.7. The peak front irradiance ranges from about 187 W m^{-2} on the overcast spring day to nearly 950 W m^{-2} on the clear spring day. The corresponding peak module temperature reaches 45.7°C in summer, while the highest daily bifacial gain is obtained for the overcast spring equinox case.

Table 2.7: Statistics of the representative design days for the top module, Helsinki Kumpula 2021.

Day	E_{mono} [Wh]	E_{bif} [Wh]	**BG** [%]	$G_{\text{front}}^{\text{max}}$ [W m^{-2}]	$T_{\text{pv}}^{\text{max}}$ [°C]
Winter solstice (21 Dec)	1037.6	1071.4	3.320	521.8	1.5
Spring equinox (20 Mar, overcast)	426.9	444.7	4.171	186.5	10.6
Spring equinox (22 Mar, clear sky)	3325.9	3435.3	3.354	949.8	27.4
Summer solstice (21 Jun)	2006.6	2079.4	3.964	632.6	45.7
Autumn equinox (22 Sep)	1771.8	1833.1	3.706	865.8	34.8

2.7 Discussion

The results of Section 2.6 are discussed here in terms of the mechanisms that govern the rear-side irradiance and the bifacial gain, of the effect of vertical module position, and of the role of the seasonal ground albedo. The implications for the design of the ventilated façade are also outlined.

2.7.1 Dominance of the wall-reflected contribution

The most significant feature of the results is the dominance of the wall-reflected term, which accounts for between about 88% and 96% of the rear-side irradiance depending on the month (Figure 2.4). This behaviour follows directly from the geometry of the ventilated cavity. Because the air gap is narrow relative to the façade height, the angular extent of sky and ground seen by the rear of the modules is small, and the wall occupies almost the entire rear field of view (Table 2.2). The rear-side irradiance is therefore controlled by the flux transmitted through the inactive area of the module and reflected by the wall, rather than by the direct view of the sky or the ground.

This finding has a direct design implication: at the baseline gap, the rear-side irradiance, and hence the bifacial gain, is governed primarily by the wall reflectance rather than by the module position or the ground albedo. A more reflective wall coating would consequently be the most effective means of increasing the bifacial contribution. This is consistent with experimental BIPV configurations reported in the literature, where the use of a reflective surface behind a bifacial module was shown to increase the rear-side contribution and improve the energy yield [71].

2.7.2 Effect of the vertical module position

The model reproduces the expected effect of vertical position: the top module, which sees the largest portion of sky, attains the highest bifacial gain, whereas the middle module, whose rear field of view is almost entirely occupied by the wall, attains the lowest (Table 2.6). The vertical segmentation of the upper module (Figure 2.5) confirms the same trend at a finer scale, with the uppermost segment receiving the highest rear-side irradiance.

On an annual basis, however, the magnitude of this effect is small, with a difference in bifacial gain of only $\Delta \mathrm{BG} \approx 0.11\,\%$ between the top and the middle module. This is a direct consequence of the wall dominance discussed above: since the sky and ground together contribute at most about $12\,\%$ of the rear-side irradiance, the variation of the sky and ground view factors with height can only modulate a small fraction of the total. The position effect, although physically captured and qualitatively in line with the expected behaviour, is therefore of secondary importance in the present baseline configuration. It is expected to become more pronounced for wider air gaps, larger façades, or lower-reflectance walls, in which the relative weight of the sky and ground contributions increases.

2.7.3 Seasonal role of the ground albedo

The seasonal behaviour of the ground-reflected contribution illustrates the interplay between albedo and available irradiance. The ground albedo at the Helsinki site varies strongly over the year, from above 0.5 under winter snow cover to about 0.11 in summer (Figure 2.6, left). One might expect the ground-reflected contribution to the rear-side irradiance to peak in winter, when the albedo is highest; the results, however, show that this contribution is comparable across spring and summer and is not maximal in winter (Figure 2.6, right). The reason is that the ground-reflected term scales with the product of the albedo and the incident irradiance: at this high latitude the winter irradiance is so low that even a very high albedo yields only a modest reflected flux, whereas the abundant summer irradiance compensates for the low summer albedo. This confirms that a realistic, monthly-resolved albedo is necessary — a constant annual value would misrepresent the seasonal distribution — but also that the ground term remains a minor contributor to the rear-side irradiance in all seasons, consistent with the dominance of the wall discussed above.

2.7.4 Magnitude of the bifacial gain

The annual bifacial gain obtained for all positions is of the order of 3.5 %, a modest value compared with those typically reported for free-standing bifacial systems. This is again a direct consequence of the building-integrated configuration with a narrow cavity: the rear surface faces a nearby wall of moderate reflectance rather than an open, highly reflective ground, so the rear-side irradiance and the resulting gain are inherently limited. The bifacial gain of the representative design days (Table 2.7) remains consistent with the annual value, ranging from 3.320 % to 4.171 %. The highest value is obtained for the overcast spring equinox case, where the reduced front-side irradiance increases the relative weight of the rear-side contribution. These results indicate that, in the present configuration, the bifacial contribution is a secondary but non-negligible term, whose exploitation would require either a more reflective wall or a wider cavity.

2.8 Model limitations

The optical–electrical model presented in this chapter should be regarded as a simplified, first-stage framework, adequate for capturing the dominant physical mechanisms and the relative influence of the design parameters, but subject to a number of limitations that are stated here for completeness and that delimit the interpretation of the results.

L1) Simplified view factors. The rear-side irradiance is reconstructed from view factors evaluated geometrically at the centre of each module (or segment), rather than through a full radiosity or ray-tracing solution over the module surface. This choice, justified by the smooth variation of the view factors with height, does not resolve the continuous distribution of the rear-side irradiance across the module face, which is only partially recovered through the segmentation of the upper module.

L2) First-order reflections. Only single reflections from the ground and the wall are considered; multiple inter-reflections between the wall, the ground and the module rear surface are neglected. Given the moderate reflectances and the dominance of the direct wall contribution, these higher-order terms are expected to be a second-order effect, but they would gain relevance for highly reflective wall coatings.

L3) Constant optical properties. The glass transmittance, the wall reflectance and the bifaciality factor are treated as constant, without angular dependence. In particular, the angle-of-incidence dependence of the glass transmittance and of the bifacial response is not modelled, which may lead to a slight overestimation of both the front and the rear absorbed irradiance at large incidence angles.

L4) Lumped thermal model in the optical stage. Within the optical–electrical model the module temperature is obtained from a lumped steady-state correlation (Eq. 2.9), which does not resolve the temperature field of the module nor the heat transfer within the ventilated cavity. This limitation is specifically addressed in the second phase of the work, where the detailed thermal behaviour of the ventilated façade is resolved through the CFD model of Chapter 3, using the absorbed loads provided by the present model as boundary conditions.

L5) Absence of experimental validation. The model has not been validated against experimental measurements for the Helsinki case study. The results should therefore be interpreted as a theoretical and comparative assessment, suitable for identifying trends and the relative weight of the governing parameters, rather than as an absolute prediction of the energy yield.

Notwithstanding these limitations, the model fulfils its intended purpose: it quantifies the front- and rear-side irradiance of a building-integrated bifacial array as a function of vertical position, identifies the wall-reflected contribution as the dominant term of the rear-side irradiance, and provides the height-resolved absorbed loads required by the subsequent CFD analysis.

Chapter 3

Computational Fluid Dynamics Model

3.1 Overview and Objectives

The optical model of Chapter 2 quantifies the solar radiation absorbed by the bifacial modules and by the wall, but it represents the thermal behaviour of the system only through a lumped, steady-state correlation for the module temperature (Section 2.4.4). That correlation does not resolve the temperature field within the modules, nor the air motion and the heat transfer that take place in the ventilated cavity between the modules and the wall. Yet it is precisely this cavity, its buoyancy-driven airflow and the associated convective and radiative exchanges, that governs the operating temperature of the array and determines the amount of heat that can be recovered from the façade. Resolving this behaviour is the purpose of the second phase of the work.

To this end, a two-dimensional, steady-state computational fluid dynamics (CFD) model of the ventilated façade is developed in ANSYS Fluent 2026 R1. The model couples heat conduction in the solid modules and wall with natural-convection airflow in the cavity and surface-to-surface radiative exchange between the cavity surfaces, in a conjugate heat transfer (CHT) framework. The absorbed solar loads computed by the optical model are applied as volumetric heat sources, providing the physical link between the two phases of the work.

The specific objectives of the CFD analysis are:

1. to resolve the temperature field of the modules and the buoyancy-driven flow in the ventilated cavity, for a set of representative seasonal operating conditions;
2. to quantify the convective and radiative heat-transfer coefficients at the rear of the modules and at the wall, and the resulting module operating temperature;
3. to assess, through a parametric study, the influence of the air-gap width on the thermal behaviour and on the cavity airflow;
4. to evaluate the thermal power that can be recovered from the cavity air in an active-façade scenario, and to identify the gap width that maximises it; and

5. to provide a physically based selection of the most favourable cavity geometry within the investigated range, combining thermal and electrical criteria.

The chapter is organised as follows. Section 3.2 describes the coupling between the optical and the thermal model through the volumetric source terms. Sections 3.3 to 3.7 define the computational domain, the governing equations, the material properties, the boundary conditions and the numerical methods. Section 3.8 reports the verification and consistency checks of the model. The results are then presented in three stages: the seasonal behaviour at the baseline gap (Section 3.9), the parametric air-gap study (Section 3.10) and the thermal-recovery analysis with the selection of the most favourable gap (Section 3.11). Section 3.12 discusses the results and Section 3.13 states the limitations of the model.

3.2 Optical-to-CFD coupling and volumetric source terms

The optical-electrical model of Chapter 2 returns the front- and rear-side irradiance incident on the PV module: G_{front} is uniform over the array, whereas $G_{\text{rear},i}$ is resolved according to the vertical module/segment discretisation introduced by the view-factor formulation of Chapter 2. The same model also provides a lumped estimate of the module operating temperature. For implementation in Fluent, the absorbed optical loads are imposed as volumetric heat-generation terms within the PV and wall solid regions rather than as surface heat fluxes. This choice ensures compatibility with the conjugate heat-transfer formulation adopted throughout (Section 3.4.5) and allows the PV solid to be kept as a single continuous solid domain (Section 3.3), with the spatial variation of the source handled entirely through a coordinate-dependent Fluent Named Expression rather than through a segmented geometry.

3.2.1 PV and wall absorbed heat fluxes

Following Chapter 2 (Eqs. 15–16), the heat flux absorbed by the PV module and available for heating is

$$q''_{front} = G_{front}\,\alpha_{abs}\,PF\,(1-\eta), \qquad q''_{rear,i} = G_{rear,i}\,\alpha_{abs}\,PF\,(1-BF\,\eta) \tag{3.1}$$

with $\alpha_{abs} = 0.90$, $PF = 0.928$, $BF = 0.80$ (Table 3.5) and η the temperature-corrected efficiency (Section 3.2.2). Because G_{front} and η are uniform over the array, q''_{front} is likewise uniform. By contrast, $q''_{\text{rear},i}$ varies band by band through $G_{\text{rear},i}$, which inherits the vertical view-factor gradient identified in Chapter 2.

The corresponding source in the wall solid represents the front-side irradiance transmitted through the optically inactive fraction of the PV module:

$$G_{wall,tr} = G_{front}\,\tau_{glass}\,(1-PF), \qquad \dot{q}_{gen,wall} = \frac{G_{wall,tr}\,\alpha_{wall}}{t_{wall}}, \qquad \alpha_{wall} = 1-\rho_{wall} = 0.70 \tag{3.2}$$

(Chapter 2, Eqs. 9, 16), applied uniformly along the full wall height, including the plenum regions (Section 3.3). Long-wave radiative losses are not subtracted from q''_{front}, $q''_{rear,i}$ or $\dot{q}_{gen,wall}$ at this stage, since radiative exchange is instead resolved explicitly within the CFD model itself, through the front-side Mixed boundary condition (Section 3.6.3) and the S2S radiation model in the cavity (Section 3.4.6).

For a band i of frontal area A_i and PV thickness t_{PV}, the resulting volumetric source is

$$\dot{q}_{gen,i} = \frac{q''_{front} + q''_{rear,i}}{t_{PV}} \tag{3.3}$$

3.2.2 Temperature-corrected efficiency and one-way coupling

The efficiency entering Equation 3.1 is the temperature-corrected value

$$\eta = \eta_{STC}\left[1 - \beta_0\left(T_{PV,lumped} - 25\right)\right], \qquad T_{PV,lumped} = T_{air} + \frac{G_{front}(1-\eta_{STC})}{U_0 + U_1 v_w} \tag{3.4}$$

with $\eta_{STC} = 0.2248$, $\beta_0 = 0.0030\,\mathrm{K}^{-1}$, and $T_{PV,lumped}$ the lumped operating temperature from Chapter 2 (Eq. 14, $U_0 = 25$, $U_1 = 1.2$), itself evaluated at η_{STC} rather than at η from Equation 3.4. This lumped temperature is computed entirely within the optical model and is generally different from the temperature field subsequently resolved by the CFD simulation (Section 3.9, Table 3.13): the coupling between the two models is one-way, with $T_{PV,lumped}$ fixing η and hence the source terms of Equations 3.1–3.2, but the CFD-resolved temperature is never fed back to update them within the same run. Each of the thirty gap-season cases of the parametric study (Section 3.10) uses its own source terms, computed from the corresponding optical-model run at that gap and season.

3.2.3 Vertical source-term discretisation and Fluent implementation

The three-module column is partitioned into five vertical bands (Table 3.1), each with its own $\dot{q}_{gen,i}$: BOTTOM and MIDDLE span one module each, while the top module – where the vertical gradient of $G_{rear,i}$ is steepest – is subdivided into TOP_LOWER, TOP_MIDDLE and TOP_UPPER, matching the segmentation of Chapter 2, Section 2.6.4.

Table 3.1: Vertical bands used for the piecewise volumetric source term.

Band	Y_{start} [m]	Y_{end} [m]
BOTTOM	0.3085	2.2695
MIDDLE	2.2695	4.2305
TOP_LOWER	4.2305	4.8842
TOP_MIDDLE	4.8842	5.5378
TOP_UPPER	5.5378	6.1915

A preliminary approach based on five separate PV solid bodies, one per band, was discarded because it introduced internal body-to-body interfaces that behaved as artificial thermal resistances between adjacent bands. The adopted strategy instead keeps the PV module as a single continuous solid region (Section 3.3) and imposes the vertical variation of the source through a coordinate-dependent Fluent Named Expression, evaluated on the cell-centroid coordinate `Position.y`:

$$\dot{q}_{\text{gen}}(y) = \begin{cases} \dot{q}_{\text{gen,BOTTOM}} & 0.3085 \leq y < 2.2695 \\ \dot{q}_{\text{gen,MIDDLE}} & 2.2695 \leq y < 4.2305 \\ \dot{q}_{\text{gen,TOP\_LOWER}} & 4.2305 \leq y < 4.8842 \\ \dot{q}_{\text{gen,TOP\_MIDDLE}} & 4.8842 \leq y < 5.5378 \\ \dot{q}_{\text{gen,TOP\_UPPER}} & 5.5378 \leq y \leq 6.1915 \end{cases} \tag{3.5}$$

assigned as the energy-equation source on the PV solid cell zone. The wall source $\dot{q}_{gen,wall}$ (Equation 3.2), being uniform along the domain height, is assigned as a single constant value on the wall solid cell zone, with no equivalent piecewise treatment required.

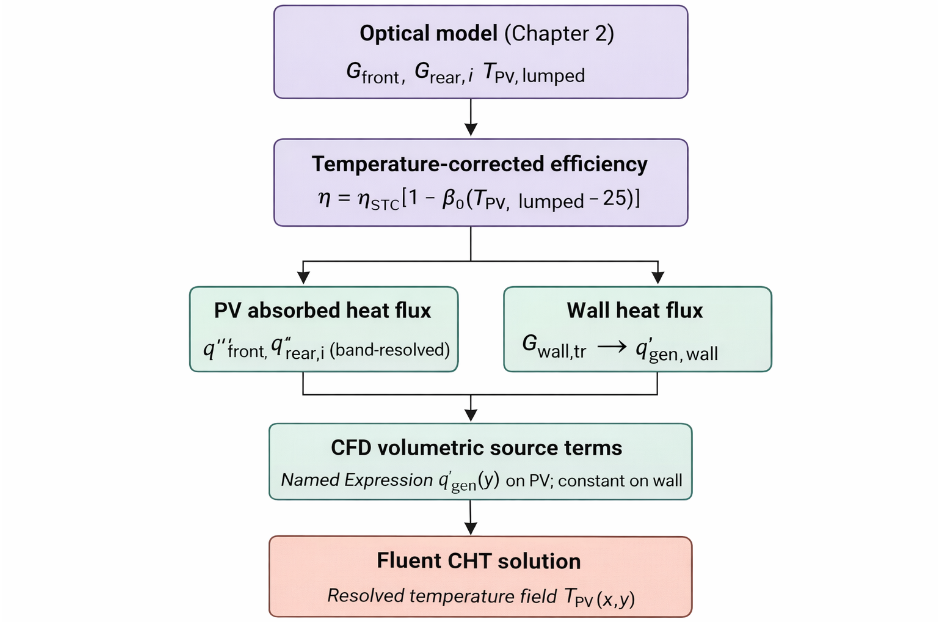

Figure 3.1: Schematic of the coupling between the optical model (Chapter 2) and the CFD domain: band-resolved irradiance and lumped temperature feed the temperature-corrected efficiency, which determines the PV and wall heat fluxes and hence the volumetric source terms imposed in Fluent. The coupling is one-way: the CFD-resolved temperature field is not fed back into the efficiency correction.

3.2.4 Scope of the coupling

In summary, the coupling is one-way and radiative–thermal only. The optical model provides fixed source terms to the CFD simulation, while the CFD-resolved temperature field is used only for post-processing and comparison, not to update the optical or electrical model. The discrepancy between $T_{\text{PV,lumped}}$ and the CFD-resolved temperature is quantified in Section 3.9.

3.3 Computational domain and geometry

3.3.1 Coordinate system and domain extent

The computational domain is defined in a two-dimensional Cartesian frame (x, y), with x normal to the façade and y vertical (positive upward, origin at the base of the cavity), consistently with the y-coordinate used in the piecewise source term of Equation 3.5. The façade is treated as a two-dimensional section: the façade width is considerably larger than the cavity depth ($d = 0.10\,\text{m}$–$0.50\,\text{m}$), so that, away from the lateral edges of the installation, gradients along the horizontal direction parallel to the façade are expected to be negligible.

The domain spans a total height $H_{dom} = 6.5\,\text{m}$ and comprises three contiguous regions along x, coupled through conjugate heat transfer at their common interfaces: the PV module ($t_{PV} = 0.030\,\text{m}$, hosting the source term of Section 3.2), the ventilated cavity (thickness d, the parametric variable), and the equivalent wall ($t_{wall} = 0.3832\,\text{m}$). Only d changes between the six gap geometries; t_{PV}, t_{wall} and H_{dom} are held fixed.

3.3.2 Vertical subdivision and plenum regions

The three modules form a continuous PV column of height $H_{PV} = 3 \times 1.961\,\text{m} = 5.883\,\text{m}$, occupying $y \in [0.3085, 6.1915\,\text{m}]$, consistent with the band boundaries of Table 3.1. Open plenum regions of height $(H_{dom} - H_{PV})/2 = 0.3085\,\text{m}$ are retained above and below the array, letting the flow organise before reaching the heated section and relax before the outlet, rather than imposing boundary conditions directly adjacent to the buoyancy-forced region. Within the plenum, the cavity is bounded on the outdoor side by an adiabatic extension (Section 3.6.6), while the wall – a continuous building element – spans the full domain height including both plenum regions.

Table 3.2: Geometric parameters of the computational domain (baseline gap $d = 0.15\,\text{m}$).

Parameter	Value
Total domain height, H_{dom}	6.5 m
PV column height (3 modules), H_{PV}	5.883 m
Bottom / top plenum height	0.3085 m each
PV thickness, t_{PV}	0.030 m
Air gap width, d	0.10 m to 0.50 m (parametric, 6 values)
Wall thickness, t_{wall}	0.3832 m

3.3.3 Geometry construction strategy

The three regions are built as separate, contiguous bodies within a single multi-body part, ensuring node-to-node continuity across the CHT interfaces without requiring a non-conformal mesh treatment. The PV is kept as a single continuous solid body in order to avoid internal interfaces between adjacent source bands. The vertical variation of the heat source is therefore imposed numerically through the coordinate-dependent Named Expression introduced in Section 3.2, rather than through a segmented geometry. The air cavity and the wall are likewise built as single continuous bodies spanning the full domain height.

3.3.4 Boundary faces and named selections

Each geometry exposes the following named selections, referenced in Section 3.6: *PV front* (outdoor-facing PV surface); *PV rear / wall front* (the two coupled-wall cavity interfaces, over H_{PV}); *plenum walls* (adiabatic outdoor-side cavity boundary within the plenum regions); *cavity inlet / cavity outlet* (horizontal faces at $y = 0$ and $y = H_{dom}$); *wall indoor* (indoor-facing wall surface, full domain height). This convention is identical across all six gap variants.

3.3.5 Parametric gap variants and S2S recalculation

Each of the six gap widths required an independently constructed geometry and mesh, with all other dimensions (Table 3.2) held fixed. Because the S2S view factors (Section 3.4.6) are purely geometric, they were recomputed for every gap variant – ray tracing at a resolution of 10 rays per surface element, with the PV rear and wall front surfaces set as critical zones – before the corresponding case was run. The baseline gap $d = 0.15$ m was used for model development, the checks of Section 3.8, and the seasonal comparison of Section 3.9; the remaining five widths were reserved for the parametric study of Section 3.10.

3.3.6 Mesh generation

A structured, quadrilateral-dominant mesh was generated for each geometry using the MultiZone method, chosen for the controlled, monotonic grading it allows across the thin, wall-bounded channel flow of interest. A double-sided biased distribution was applied across the cavity thickness, clustering elements toward both the PV rear and wall front surfaces, with first-cell height sized to target $y^+ \approx 1$ at each wall, consistent with the Enhanced Wall Treatment formulation (Section 3.4.4). Along y, node lines were placed at each band boundary of Table 3.1, so that the source discontinuities of Equation 3.5 coincide with element faces.

The baseline mesh comprises 14 483 elements (15 203 nodes), distributed as 1800 elements in the PV solid, 8000 in the air cavity, and 4683 in the wall solid (Table 3.3), with orthogonal quality and aspect ratio within the ranges recommended for the solver of Section 3.7. For the wider-gap variants, the near-wall resolution and grading ratio were adjusted to preserve the same target y^+ across all six geometries; the adequacy of this resolution is assessed through a mesh-independence check reported in Section 3.8.3.

Table 3.3: Baseline mesh element and node count by region (gap $d = 0.15\,\mathrm{m}$).

Region	Nodes	Elements
PV solid	2034	1800
Air cavity	8241	8000
Wall solid	4928	4683
Total	15203	14483

Figure 3.2 shows the full computational domain, illustrating the extreme aspect ratio of the façade cross-section (total height 6.5 m against a total thickness of only 0.5632 m). Figure 3.3 then shows a magnified detail of the mesh at mid-height, where the near-wall bias distribution within the air cavity, described above, is clearly visible.

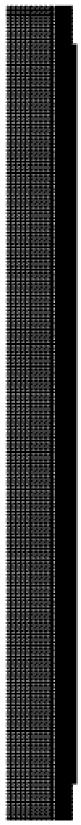

Figure 3.2: Full computational domain for the baseline gap configuration ($d = 0.15\,\mathrm{m}$), showing the extreme aspect ratio of the façade cross-section.

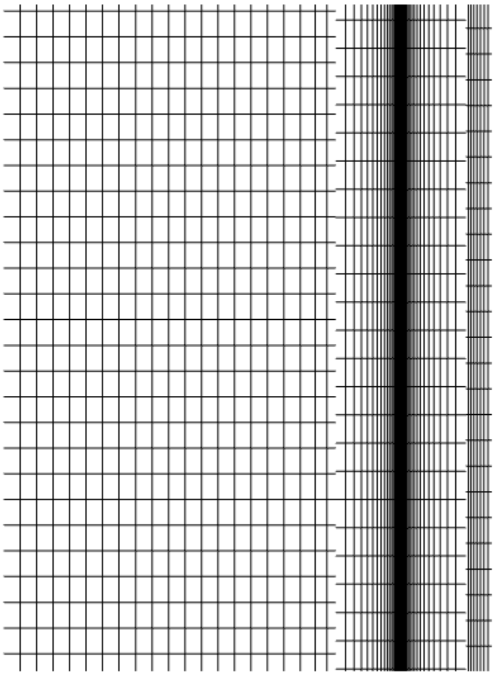

Figure 3.3: Detail of the structured mesh at mid-height, showing the near-wall bias distribution within the air cavity ($d = 0.15\,\mathrm{m}$).

3.4 Mathematical model

The CFD model solves the steady-state RANS equations for mass, momentum and energy within the air cavity, coupled with steady-state conduction in the two solid regions, and a surface-to-surface radiation model for long-wave exchange between the cavity-facing surfaces.

3.4.1 Continuity equation

For steady, incompressible flow,

$$\frac{\partial(\rho u_i)}{\partial x_i} = 0 \tag{3.6}$$

with ρ the fluid density and u_i the mean velocity component along x_i ($i \in \{1, 2\}$: horizontal across the gap, vertical along the façade height).

3.4.2 Momentum equation and the Boussinesq approximation

$$\frac{\partial(\rho u_i u_j)}{\partial x_j} = -\frac{\partial p}{\partial x_i} + \frac{\partial}{\partial x_j}\left[(\mu + \mu_t)\left(\frac{\partial u_i}{\partial x_j} + \frac{\partial u_j}{\partial x_i}\right)\right] + \rho g_i \tag{3.7}$$

where p is pressure, μ the molecular viscosity, μ_t the turbulent viscosity, and g_i the gravitational acceleration. The buoyancy source ρg_i is the sole driver of the flow in this problem (Section 3.6.2: no velocity is imposed at either cavity opening).

Given the moderate temperature excursions relative to the absolute temperature level, density is treated through the Boussinesq approximation: held constant at ρ_0 everywhere except in the buoyancy term, where it is linearised about the reference temperature T_0,

$$\rho \approx \rho_0 \left[1 - \beta(T - T_0)\right] \tag{3.8}$$

with $\rho_0 = 1.241\,\mathrm{kg\,m^{-3}}$ and $\beta = 0.003\,53\,\mathrm{K^{-1}}$ (Table 3.4; the choice of reference state is discussed in Section 3.5.1). This allows the flow to be solved as effectively incompressible while retaining the buoyancy forcing that drives the entire ventilation mechanism.

3.4.3 Energy equation

$$\frac{\partial(\rho u_i c_p T)}{\partial x_i} = \frac{\partial}{\partial x_i}\left[(k + k_t)\frac{\partial T}{\partial x_i}\right] \tag{3.9}$$

with $k_t = c_p \mu_t / \mathrm{Pr}_t$ ($\mathrm{Pr}_t = 0.85$, Fluent default) and air properties from Table 3.4, held constant except for the buoyancy linearisation above.

3.4.4 Turbulence closure

Although the cavity flow is buoyancy- rather than shear-driven, local instabilities and mixing can develop as air accelerates along the heated PV rear surface. Turbulence is modelled with the RNG k–ε model [73], in preference to the standard k–ε formulation, because its renormalization-group-derived correction to the dissipation-rate equation improves accuracy for flows with streamline curvature, recirculation and buoyancy effects, all relevant here. The model solves standard transport equations for k and ε, including a buoyancy production/destruction term G_b evaluated consistently with the Boussinesq density model, with $\mu_t = \rho C_\mu k^2/\varepsilon$ and RNG default constants ($C_\mu = 0.0845$, $C_{1\varepsilon} = 1.42$, $C_{2\varepsilon} = 1.68$). Buoyancy production in both the momentum and turbulence equations is activated through Fluent's Full Buoyancy Effects option.

Near-wall treatment uses Enhanced Wall Treatment (EWT), resolving the viscous sublayer directly rather than bridging it with wall functions calibrated on forced-convection boundary layers not representative of the present buoyancy-driven regime. This is required because the convective coefficients of Section 3.4.7 are extracted directly from the near-wall fields, and motivates the $y^+ \approx 1$ mesh target of Section 3.3.6.

3.4.5 Heat conduction in the solid regions

$$\nabla \cdot (k_s \nabla T) + S = 0 \tag{3.10}$$

with S the volumetric source: $\dot{q}_{gen}(y)$ (Equation 3.5) in the PV solid, $\dot{q}_{gen,wall}$ (Equation 3.2) in the wall. Solid properties are given in Table 3.6. Temperature and heat-flux continuity are enforced at both solid-fluid interfaces through the coupled-wall CHT formulation.

3.4.6 Surface-to-surface radiation model

Cavity air is treated as non-participating in the infrared, so radiative exchange occurs only between the PV rear and wall front surfaces, modelled as diffuse-grey through the S2S model. The radiosity of surface k is

$$J_k = \varepsilon_k \sigma T_k^4 + (1 - \varepsilon_k) \sum_j F_{kj} J_j \tag{3.11}$$

with σ the Stefan–Boltzmann constant and F_{kj} the view factor between surfaces k and j (Section 3.3.5, ray tracing at 10 rays/element). The net radiative flux at each surface, $q''_k = J_k - \sum_j F_{kj} J_j$, enters the surface energy balance at each coupled wall; view factors are fixed per geometry, while radiosities are updated through the Loosely Coupled scheme of Section 3.7.4.

3.4.7 Extraction of convective heat transfer coefficients

The convective heat transfer coefficient at each cavity-facing surface is extracted directly from the converged solution,

$$h = \frac{q''_{conv}}{T_{surf} - T_{ref}} \tag{3.12}$$

with T_{ref} taken as the ambient inlet temperature T_{air} of the corresponding climatic case. Equation 3.12 gives h_{rear} (PV rear surface) and h_{wall} (wall surface), each an area-weighted average over the full array height.

For comparison with the literature, a corresponding Nusselt number can also be derived as $Nu = hL/k_{\text{air}}$, with $L = d$ the gap width, the natural characteristic length for a parallel-plate vertical channel. However, h is retained as the primary output of the CFD analysis throughout this chapter, since it directly quantifies the heat exchange at the cavity-facing surfaces without the additional ambiguity introduced by a variable characteristic length across the six gap widths of the parametric study.

3.5 Material properties

3.5.1 Constant-properties assumption

All thermophysical properties, fluid and solid, are held constant throughout the domain and across the full simulation matrix, with the sole exception of the Boussinesq buoyancy linearisation of Equation 3.8. The reference temperature for the air properties, $T_0 \approx 284.4\,\mathrm{K}$ (11.3 °C), was back-calculated from the Boussinesq reference density $\rho_0 = 1.241\,\mathrm{kg\,m^{-3}}$ via the ideal gas law, and closely matches the ambient temperature of the Autumn Equinox benchmark case (10.2 °C) from which the property set was originally derived. This single reference state was then retained unchanged for all thirty gap-season combinations of the parametric study; the consequences of this simplification at the seasonal extremes are quantified in Section 3.13.

3.5.2 Air properties

Table 3.4: Reference thermophysical properties of air (Boussinesq incompressible model), evaluated at $T_0 \approx 284.4\,\mathrm{K}$, verified from the Fluent material definition.

Property	Symbol	Value	Unit
Reference density	ρ_0	1.241	$\mathrm{kg\,m^{-3}}$
Thermal expansion coefficient	β	0.00353	$\mathrm{K^{-1}}$
Specific heat capacity	c_p	1006.43	$\mathrm{J\,kg^{-1}\,K^{-1}}$
Thermal conductivity	k	0.02494	$\mathrm{W\,m^{-1}\,K^{-1}}$
Dynamic viscosity	μ	1.761×10^{-5}	Pa s
Kinematic viscosity (derived)	$\nu = \mu/\rho_0$	1.419×10^{-5}	$\mathrm{m^2\,s^{-1}}$
Prandtl number (derived)	Pr	0.711	–

The derived Prandtl number, $\mathrm{Pr} \approx 0.71$, matches standard tabulated values for air near this temperature, confirming the internal consistency of the property set; note also $\beta \approx 1/T_0$, consistent with the ideal-gas origin of both quantities.

3.5.3 PV module properties

The PV module is represented as a single homogeneous solid (Table 3.5), justified by its small thickness ($t_{PV} = 0.030\,\mathrm{m}$) relative to the other length scales of the problem.

Table 3.5: Photovoltaic module properties (effective homogeneous solid).

Property	Symbol	Value	Unit
Thermal			
Density	ρ_{PV}	2500	$\mathrm{kg\,m^{-3}}$
Specific heat	$c_{p,PV}$	750	$\mathrm{J\,kg^{-1}\,K^{-1}}$
Thermal conductivity	k_{PV}	1.4	$\mathrm{W\,m^{-1}\,K^{-1}}$
Thickness	t_{PV}	0.030	m
Radiative / optical			
Front / rear emissivity	$\varepsilon_{front}, \varepsilon_{rear}$	0.90	–
Glass transmittance	τ_{glass}	0.90	–
Solar absorptance	α_{abs}	0.90	–
Packing factor	PF	0.928	–
Module efficiency (STC)	η_{STC}	0.2248	–
Temperature coefficient of power	β_0	0.0030	$\mathrm{K^{-1}}$
Bifaciality factor	BF	0.80	–

The radiative, optical and electrical properties are inherited from the optical–electrical model of Chapter 2. The electrical parameters are based on the Leapton LP182-54 datasheet, while τ_{glass} and α_{abs} are assumed reference values consistent with radiative heat-transfer data. Within the CFD model, ϵ_{front} and ϵ_{rear} enter the PV front Mixed and PV rear coupled-wall boundary conditions, respectively (Section 3.6); τ_{glass}, α_{abs}, PF, η_{STC}, β_0 and BF enter the upstream source-term derivation of Section 3.2.

3.5.4 Equivalent wall properties

The wall is represented by a single equivalent homogeneous solid, sized to reproduce the overall transmittance $U_{wall} = 0.168\,\mathrm{W\,m^{-2}\,K^{-1}}$ (Chapter 2, Eq. 18, $R_{wall} = 5.95\,\mathrm{m^2\,K\,W^{-1}}$, conductive resistance only, without surface films – consistent with the present model, where those films are represented separately by the PV-front and indoor-wall boundary conditions). With $t_{wall} = 0.3832\,\mathrm{m}$,

$$k_{wall} = U_{wall}\,t_{wall} = 0.168 \times 0.3832 = 0.0644\,\mathrm{W\,m^{-1}\,K^{-1}} \tag{3.13}$$

Density and specific heat, $\rho_{wall} = 791.4\,\mathrm{kg\,m^{-3}}$ and $c_{p,wall} = 846.8\,\mathrm{J\,kg^{-1}\,K^{-1}}$, are thickness-weighted averages of the multilayer construction (Chapter 2, Table 6); since the model is steady-state, these two properties affect only the pseudo-transient path to convergence (Section 3.7), not the converged solution. The wall front surface emissivity, $\varepsilon_{wall} = 0.90$, was likewise verified from the Fluent boundary condition setup.

Table 3.6: Equivalent wall properties.

Property	Symbol	Value
Density [kg m^{-3}]	ρ_{wall}	791.4
Specific heat [J kg^{-1} K^{-1}]	$c_{p,wall}$	846.8
Thermal conductivity [W m^{-1} K^{-1}]	k_{wall}	0.0644
Thickness [m]	t_{wall}	0.3832
Front emissivity	ε_{wall}	0.90

All non-participating boundaries (plenum extensions, module edges) are adiabatic with zero emissivity, excluding them from the S2S radiative network (Section 3.6.6).

3.6 Boundary conditions

3.6.1 Steady-state formulation for representative operating points

Each of the thirty simulations represents an independent steady-state snapshot of the façade at the peak-irradiance hour of one representative design day, for one gap width – not a simulation of every hour of the year. Ambient conditions and the volumetric source terms of Section 3.2 are fixed inputs for each case; no transient coupling exists between simulations. Boundary condition *types* are identical across all thirty cases, differing only in the season- and gap-dependent input values, summarised in Table 3.7.

Table 3.7: Summary of boundary conditions applied to the computational domain.

Named selection	**Type**	**Governing relation**
`cavity_inlet`	Pressure inlet (gauge 0)	Section 3.6.2
`cavity_outlet`	Pressure outlet (gauge 0)	Section 3.6.2
PV front	Mixed (convection + external radiation)	Section 3.6.3, Eqs. 3.14–3.15
`wall_indoor`	Fixed temperature	Section 3.6.4
PV rear, wall front	Coupled wall, S2S participant	Section 3.6.5
Plenum walls, module edges	Adiabatic, non-participating	Section 3.6.6
PV solid (cell zone)	Volumetric source (Eq. 3.5)	Section 3.2

3.6.2 Cavity inlet and outlet

Both cavity openings are pressure boundaries at zero gauge pressure, rather than a velocity inlet with a prescribed chimney velocity: since the flow rate is precisely the quantity the simulation is meant to predict (Section 3.4.2), imposing it a priori would be circular. With both openings at the same reference pressure, the flow rate – and hence U_{gap} – emerges from the density variation within the cavity. Backflow temperature at both boundaries is set to the ambient air temperature T_{air}; the inlet hydraulic diameter is set consistently as $D_h = 2d$ for the parallel-plate channel.

3.6.3 PV front: Mixed boundary condition

The PV front exchanges heat with the environment through convection and long-wave sky radiation, combined in a single Mixed condition. The convective coefficient follows the McAdams correlation,

$$h_{\text{front}} = 5.7 + 3.8V \tag{3.14}$$

with V the wind speed. The correlation was originally based on the experimental data of Jürges for a heated vertical flat plate and was later reported by McAdams [20]. It was preferred over temperature-dependent correlations, such as the Faiman model, because these would require the unknown PV surface temperature as an input, introducing a circular dependency. The free-stream temperature is T_{air}; the external radiation temperature follows the Swinbank correlation [72],

$$T_{sky} = 0.0552\, T_{air}^{1.5} \tag{3.15}$$

(both in kelvin), capturing the physically expected narrowing of the sky-to-ambient gap under cold, dry winter conditions. External emissivity is $\varepsilon_{front} = 0.90$ (Table 3.5).

3.6.4 Indoor wall surface

The indoor wall surface is held at $T_{indoor} = 294.15\,\text{K}$ (21 °C), identical across all thirty simulations, representing a conditioned indoor space decoupled from the outdoor seasonal variation.

3.6.5 Coupled walls: PV rear and wall front

The PV rear and wall front interfaces are coupled-wall boundaries enforcing CHT continuity (Section 3.4.5); no convective coefficient is prescribed, since the local flux is computed directly from the resolved near-wall gradients (Sections 3.4.4, 3.3.6) and only post-processed into h_{rear}, h_{wall} (Section 3.4.7). Both surfaces participate in the S2S network with $\varepsilon_{rear} = \varepsilon_{wall} = 0.90$.

3.6.6 Adiabatic boundaries

The plenum wall extensions and the PV top/bottom edges are adiabatic ($q'' = 0$) with zero emissivity, excluded from the S2S network – representing either a domain extension not physically present (plenum) or a small-area edge of negligible heat exchange (module edges).

3.6.7 Volumetric source term

The PV and wall solids carry the volumetric sources of Section 3.2 (Equations 3.5, 3.2). Although a cell-zone rather than boundary condition, it is listed in Table 3.7 as it completes the external forcing specification for each case.

3.6.8 Seasonal climatic inputs

Table 3.8 reports T_{air} and V for the five design days, from the FMI record at Helsinki Kumpula, shared with Chapter 2; these are independent of gap width, unlike the source terms of Section 3.2, which vary with d through the rear-side view factors.

Table 3.8: Ambient climatic inputs by representative design day (baseline gap $d = 0.15\,\mathrm{m}$).

Design day	T_{air} [°C]	V [m s^{-1}]	h_{front} [W m^{-2} K^{-1}]	T_{sky} [K]	G_{front} [W m^{-2}]
Winter Solstice (21 Dec)	−12.2	3.55	19.19	232.69	509.48
Spring Equinox, overcast (20 Mar)	−0.2	8.65	38.57	248.92	135.41
Spring, clear sky (22 Mar)	2.1	4.50	22.80	252.08	942.31
Autumn Equinox (22 Sep)	10.2	2.50	15.20	263.28	801.26
Summer Solstice (21 Jun)	30.1	4.80	23.94	291.50	573.84

All five days use the peak-irradiance hour from the corresponding FMI/optical-model record; h_{front} and T_{sky} follow directly from Equations 3.14–3.15 (e.g. Autumn: $5.7 + 3.8 \times 2.5 = 15.2\,\mathrm{W\,m^{-2}\,K^{-1}}$). Wind speed does not track the thermal season label monotonically: Spring overcast has the highest wind of the matrix ($8.65\,\mathrm{m\,s^{-1}}$) despite mild temperatures, governing its comparatively high h_{front}.

3.7 Numerical methods and convergence

This section documents the numerical schemes, solver settings and convergence criteria applied uniformly across all thirty simulations of the seasonal and parametric matrix.

3.7.1 Solver formulation

The governing equations of Section 3.4 are solved in ANSYS Fluent 2026 R1 using a pressure-based, steady-state formulation. Pressure–velocity coupling is handled with the Coupled algorithm, selected for its robustness in buoyancy-driven flows, where pressure and velocity are strongly linked through the thermal driving force.

The solver is run in pseudo-transient mode. In this formulation, the pseudo-time step acts only as a numerical relaxation mechanism to improve convergence towards the steady-state solution; it does not represent a physical transient evolution of the façade. This choice improves stability during the development of the natural-convection flow field while preserving the steady-state nature of the governing equations.

3.7.2 Spatial discretisation schemes

Gradient reconstruction is performed using the default Least Squares Cell-Based method. Pressure interpolation is performed using the PRESTO! (Pressure Staggering Option) scheme, selected in preference to the standard or second-order pressure interpolation schemes because of its established effectiveness for flows dominated by strong pressure gradients normal to the flow direction, a characteristic feature of buoyancy-driven channel flows such as the present cavity, where the pressure field varies sharply across the (thin) gap direction while the flow itself develops predominantly along the (long) vertical direction.

All other transported quantities (momentum, turbulent kinetic energy k, turbulent dissipation rate ε, and energy (temperature)) are discretised using the Second Order Upwind scheme. This choice, in preference to the (more diffusive but more robust) First Order Upwind scheme, was made to minimise numerical diffusion, which is particularly important in this application because numerical diffusion in a natural-convection problem tends to artificially smear the thin thermal and velocity boundary layers along the PV rear and wall front surfaces (Section 3.3.6) whose gradients directly determine the convective heat transfer coefficients h_{rear} and h_{wall} that constitute the principal output of the model (Section 3.4.7). The higher sensitivity of second-order schemes to mesh quality and initial transients was mitigated by the structured, high-orthogonal-quality mesh described in Section 3.3.6 and by the Hybrid Initialization and staged iteration strategy described below.

3.7.3 Initialization

Each simulation is initialized using Fluent's Hybrid Initialization method. This approach provides a physically reasonable initial estimate of the pressure and velocity fields based on the prescribed boundary conditions, which is particularly useful in the present case because no inlet velocity is imposed and the cavity flow must develop naturally from buoyancy. After initialization, the solution is advanced iteratively until the convergence criteria described in Section 3.7.5 are satisfied.

3.7.4 Radiation-CHT coupling: Loosely Coupled scheme

Because the S2S radiation calculation (Section 3.4.6) and the conjugate heat transfer solution are both temperature-dependent and mutually coupled – surface temperatures determine radiosities through Equation 3.11, while radiative fluxes in turn enter the surface energy balance driving those same temperatures – the two are not solved simultaneously at every iteration, which would be prohibitively expensive, but through a Loosely Coupled CHT scheme, in which the radiative exchange is recomputed and updated every 10 flow/energy iterations rather than at every single iteration. This interval was adopted as a balance between computational cost (each radiation update requires evaluating Equation 3.11 across the participating surfaces) and the rate at which surface temperatures evolve during the iterative solution, over which the underlying view factors (fixed per geometry, Section 3.3.5) do not change, so that only the radiosities need to be re-evaluated at each such interval.

3.7.5 Convergence criteria

Convergence for each case is assessed through two independent and complementary criteria, applied jointly rather than in isolation:

1. **Scaled residuals.** The scaled residuals of continuity, momentum, energy, k and ε are monitored throughout the iterative solution. Residual reduction is used as a numerical convergence indicator, but it is not considered sufficient on its own; convergence is accepted only when residual stabilisation is accompanied by global energy-balance closure and stable temperature, velocity and mass-flow monitors.

2. **Global energy balance closure.** Independently of the residual trend, the overall energy balance of the domain, that is the net of all boundary heat flows and the volumetric energy source, as reported by Fluent's flux report (illustrated for the mesh-independence check of Section 3.8.3), is required to close to within approximately 1 % of the total absorbed solar power for the baseline gap width, recognising that this closure error can increase in low-load cases and at larger gap widths, reaching about 3.7% across the full matrix (Section 3.10) as the convective enthalpy share of the balance grows relative to the conductive and radiative shares.

A case is considered converged only when both criteria are satisfied simultaneously;

residual decay alone, without a correspondingly small energy imbalance, was not considered sufficient evidence of a physically converged solution, since a stalled but numerically stable residual trend can in principle coexist with a systematic energy leak associated with an incompletely resolved radiative or convective coupling.

In addition to the two criteria above, point and surface monitors of temperature, velocity and mass flow rate at representative locations within the cavity (e.g. at the mid-height of the MIDDLE band, Table 3.1) are tracked throughout the iteration history, to verify that the solution has reached a genuinely stable steady state, with these monitored quantities exhibiting a flat trend over the final several hundred iterations, rather than a transient plateau that might still be evolving slowly.

For the baseline benchmark case (Autumn Equinox, $d = 0.15\,\text{m}$), both criteria were satisfied by iteration 383, with a final energy balance closure of 0.43 % (Section 3.8); the mesh-independence check of Section 3.8.3, performed on a mesh refined by a factor of 3.7, required approximately 2000 iterations to reach a comparable closure of 0.62 %, consistent with the expectation that a finer mesh, while not changing the extracted heat transfer coefficients appreciably, requires a larger number of iterations to reach an equivalent level of convergence.

3.8 Verification and consistency checks

3.8.1 Purpose and scope

The baseline configuration (Autumn Equinox, $d = 0.15\,\text{m}$) is subjected to a set of internal consistency checks: global conservation, mesh independence, and agreement between the model's coupled components. These are checks of numerical and internal physical consistency, not validation in the strict sense, since no experimental measurements are available for this façade configuration – a limitation stated explicitly in Section 3.13. Their purpose is to establish that the numerical solution is trustworthy on its own terms before it is used to draw physical conclusions.

3.8.2 Global energy balance closure

The baseline case closes to 0.43 % of the total absorbed solar power, reached at iteration 383 (Section 3.7.5). As part of the mesh-independence check below, the same balance was recomputed on the refined mesh (53 503 elements), giving the breakdown of Table 3.9.

Table 3.9: Global energy balance, Autumn Equinox benchmark case, refined mesh (53 503 elements).

Boundary / source	Heat transfer rate [W]
`inlet_air`	+1466.20
`outlet_air`	−2367.82
PV front	−2372.24
`wall_indoor`	−118.61
Volumetric source	+3371.54
Net imbalance	−20.93

This corresponds to a closure of 0.62 %, consistent in order of magnitude with the baseline mesh, with the expected sign and relative magnitude on each term: the volumetric source is the only incoming contribution, balanced predominantly by the cavity outlet and PV front, with a smaller indoor-wall contribution (Section 3.12).

3.8.3 Mesh independence

A refined mesh was generated by doubling the divisions along all four edge-sizing controls of the baseline mesh (Section 3.3.6), retaining the same bias factor of 20 on the cavity-thickness sizing, yielding 53 503 elements (54 857 nodes, a factor of 3.7 increase), distributed as 4980 in the PV solid, 32 000 in the air cavity, and 16 523 in the wall solid. The refined case was re-initialised, the S2S view factors recomputed for the new surface discretisation, and the solution iterated to the closure reported above. Table 3.10 compares the extracted coefficients.

Table 3.10: Mesh independence check: convective heat transfer coefficients, baseline vs. refined mesh (Autumn Equinox, $d = 0.15\,\mathrm{m}$).

Quantity	Baseline (14 483 el.)	Refined (53 503 el.)	Relative change
h_{rear} [$\mathrm{W\,m^{-2}\,K^{-1}}$]	6.97	7.02	+0.72%
h_{wall} [$\mathrm{W\,m^{-2}\,K^{-1}}$]	1.57	1.62	+3.18%
Energy balance error [%]	0.43	0.62	–

h_{rear}, the coefficient governing the dominant heat removal pathway and the primary quantity of interest throughout Sections 3.9–3.10, changes by less than 1 % upon refinement. h_{wall} changes by 3.18 % in relative terms, corresponding to only $0.05\,\mathrm{W\,m^{-2}\,K^{-1}}$ in absolute terms – within the precision at which these coefficients are reported. The baseline mesh resolution (Table 3.3) is therefore retained for the full thirty-case matrix.

3.8.4 Consistency between the optical source input and the CFD volumetric integration

A check specific to the two-stage coupling strategy (Section 3.2) verifies that the total power prescribed by the piecewise source (Equation 3.5) matches the total reported by the solver at convergence – an error in a band boundary, value mapping, or unit conversion would not necessarily cause the solver to fail, but would silently bias the thermal solution. For the baseline case,

$$P_{PV} = t_{PV} \sum_i \dot{q}_{gen,i}\, h_i \qquad (3.16)$$

with h_i the band heights (Table 3.1), gives $P_{PV} = 3135.66\,\mathrm{W}$ per unit façade width (Table 3.11); adding the wall source, $P_{wall} = 94.72 \times 0.3832 \times 6.5 = 235.92\,\mathrm{W}$, gives a manually integrated total of 3371.58 W, against the 3371.5438 W reported directly by Fluent (Table 3.9) – a difference of 0.0011 %, confirming a correctly implemented Named Expression.

Table 3.11: Manual integration of the piecewise PV source term, Autumn Equinox benchmark case ($d = 0.15\,\mathrm{m}$).

Band	h_i [m]	$\dot{q}_{gen,i}$ [W m^{-3}]	P_i [W]
BOTTOM	1.9610	17 765.82	1045.16
MIDDLE	1.9610	17 763.58	1045.03
TOP_LOWER	0.6537	17 764.63	348.38
TOP_MIDDLE	0.6536	17 767.18	348.38
TOP_UPPER	0.6537	17 781.26	348.71
P_{PV} (sum)			3135.66

3.8.5 Solution stability and physical plausibility

The converged baseline solution shows a single, unidirectional upward flow with no significant recirculation, a temperature field increasing monotonically with height (consistent with the expected solar-chimney behaviour), and stable monitor plateaus (Section 3.7.5) rather than a slowly drifting trend – consistent with a genuine steady solution rather than a numerically stalled intermediate state.

3.9 Seasonal results for the baseline gap

3.9.1 Summary

Table 3.12 collects the CFD results for the five design days (Section 3.6.8) at $d = 0.15\,\mathrm{m}$.

Table 3.12: Seasonal results at the baseline gap width ($d = 0.15\,\mathrm{m}$).

Design day	T_{PV} [°C]	Gradient [K]	U_{gap} [m s^{-1}]	h_{rear} [W m^{-2} K^{-1}]	h_{wall} [W m^{-2} K^{-1}]
Winter Solstice	−2.10	1.20	0.690	4.93	1.79
Spring, overcast	0.60	0.20	0.350	n.s.	1.82
Spring, clear sky	20.10	1.79	0.865	6.78	1.86
Autumn Equinox	28.30	2.03	0.852	6.97	1.57
Summer Solstice	40.70	0.90	0.668	6.08	1.47

Note: n.s. = not significant. For the spring overcast case, the PV is nearly in thermal equilibrium with the cavity air, so $T_{\mathrm{surf}} - T_{\mathrm{ref}}$ in Equation 3.12 is too small for h_{rear} to be robustly defined.

Energy balance closure: 1.3 % (Winter), 2.9 % (Spring overcast), 0.62 % (Spring clear), 0.43 % (Autumn), 1.1 % (Summer).

Overall, the baseline simulations show that the cavity behaves as a buoyancy-driven vertical channel, with upward airflow developing in all seasonal cases. The highest air velocities and rear-side heat-transfer coefficients occur under the high-irradiance spring clear and autumn conditions, whereas the spring overcast case exhibits the weakest thermal driving force.

3.9.2 Mean temperature and vertical gradient

T_{PV} spans approximately 43 K, from −2.10 °C (Winter) to 40.70 °C (Summer), tracking the seasonal range of irradiance and ambient temperature (Table 3.8). The vertical gradient is largest for Spring clear (1.79 K) and Autumn (2.03 K), smallest for Spring overcast (0.20 K), consistent with the latter's near-zero net thermal loading.

Figure 3.4 shows the predicted temperature field over the full domain for the Autumn Equinox benchmark case. Figure 3.5 shows a magnified detail at mid-height, where the thermal gradient across the PV–cavity–wall thickness is clearly visible.

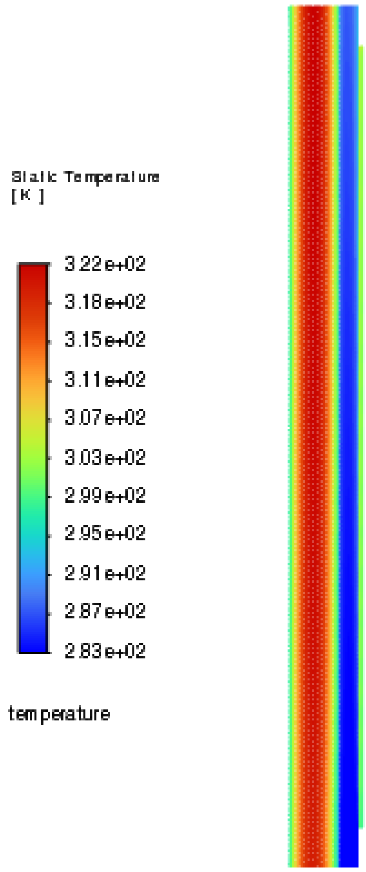

Figure 3.4: Predicted temperature contour, full domain, Autumn Equinox benchmark case ($d = 0.15\,\mathrm{m}$).

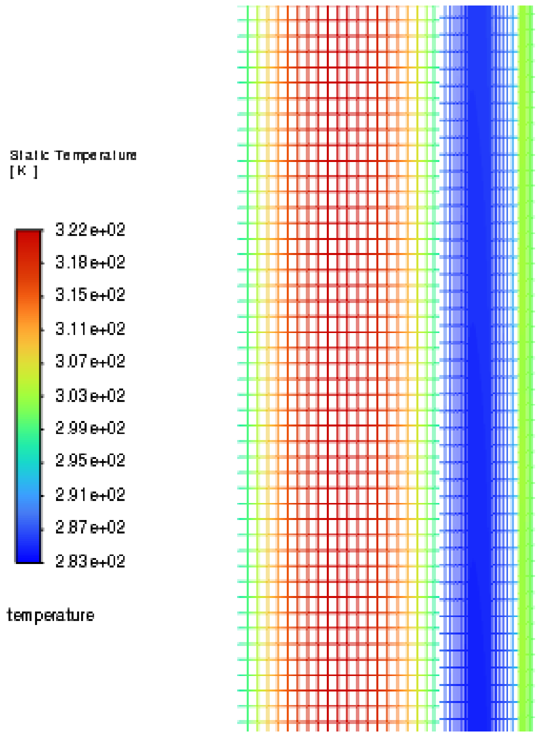

Figure 3.5: Detail of the temperature gradient across the PV–cavity–wall thickness at mid-height, Autumn Equinox benchmark case ($d = 0.15\,\mathrm{m}$).

3.9.3 Airflow field

U_{gap} ranges from $0.350\,\mathrm{m\,s^{-1}}$ (Spring overcast) to $0.865\,\mathrm{m\,s^{-1}}$ (Spring clear); Autumn ($0.852\,\mathrm{m\,s^{-1}}$) is comparable despite its higher T_{PV}, since U_{gap} tracks the local buoyancy-sustaining temperature difference rather than the absolute PV temperature. All five cases show a single, unidirectional upward flow with no significant recirculation (Section 3.8.5).

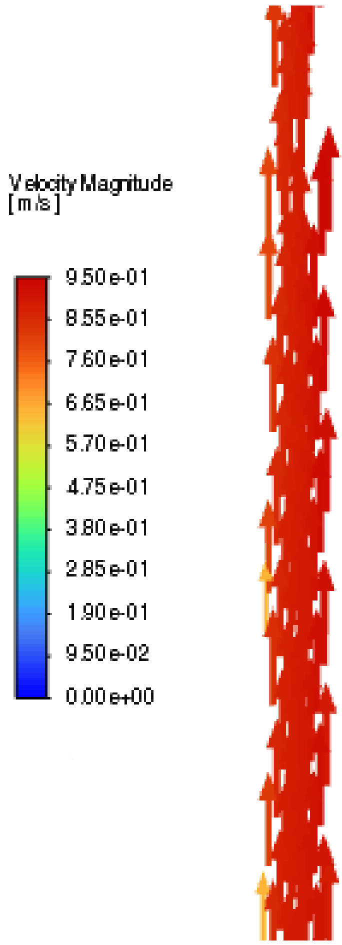

Figure 3.6: Predicted velocity magnitude field in the ventilated cavity for the Autumn Equinox benchmark case ($d = 0.15$ m). The superimposed vectors show the buoyancy-driven upward airflow developing between the PV rear surface and the building wall.

3.9.4 Vertical temperature profile

Figure 3.7 shows the vertical PV temperature profile along the module column for the five seasonal cases at the baseline gap width ($d = 0.15$ m). The profile was extracted along the central line of the PV solid, from the bottom to the top of the active module column. In Winter, Spring clear, Autumn and Summer, the temperature generally increases with height, consistently with the progressive warming of the cavity air as it flows upward through the heated section. The Spring overcast case shows a comparatively flat profile, in agreement with the weak thermal driving force reported in Table 3.12.

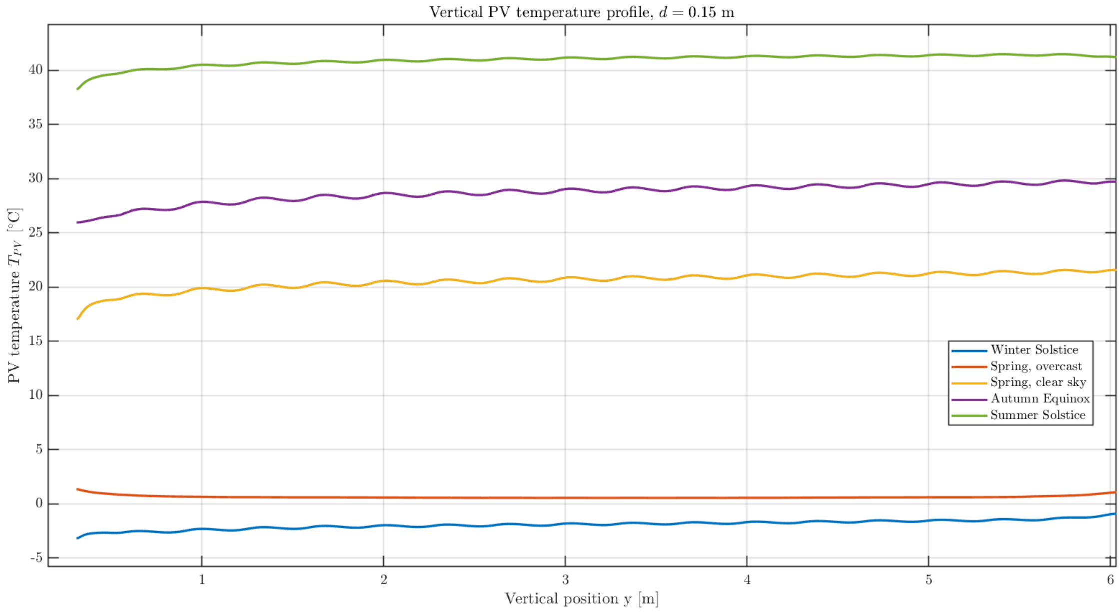

Figure 3.7: Vertical PV temperature profile along the module column for the five seasonal cases at the baseline gap width ($d = 0.15$ m).

3.9.5 Wall-side coefficient

h_{wall} ranges from 1.47 W m^{-2} K^{-1} (Summer) to 1.86 W m^{-2} K^{-1} (Spring clear), a factor of 4–5 smaller than h_{rear}, consistent with the wall's passive role relative to the actively heated PV surface.

3.9.6 Lumped vs. CFD-resolved temperature

The source terms driving each simulation used η evaluated at $T_{PV,lumped}$ (Equation 3.4), computed from the ambient inputs of Table 3.8. Table 3.13 compares this against the CFD-resolved T_{PV}.

Table 3.13: Lumped (optical model) vs. CFD-resolved mean PV temperature, baseline gap ($d = 0.15$ m).

Design day	$T_{PV,lumped}$ [°C]	T_{PV}, CFD [°C]	Difference [K]
Winter Solstice	1.30	−2.10	3.40
Spring, overcast	2.77	0.60	2.17
Spring, clear sky	26.13	20.10	6.03
Autumn Equinox	32.38	28.30	4.08
Summer Solstice	44.56	40.70	3.86

$T_{\mathrm{PV,lumped}}$ overestimates the CFD-resolved temperature in every season, by 2.17–6.03 K. This is expected: the lumped correlation represents the module heat loss through an effective empirical coefficient and does not explicitly resolve the additional cooling pathway provided by the ventilated rear cavity, namely rear-side convection and radiative exchange with the wall (Section 3.4.6). This is precisely the limitation of the lumped thermal treatment that motivates the CFD analysis of this chapter.

3.10 Parametric air-gap study

3.10.1 Overview

The CFD methodology validated on the baseline gap (Sections 3.8–3.9) is applied to five additional cavity depths, $d \in \{10, 15, 20, 30, 40, 50\}$ cm, combined with the five seasonal design days into a matrix of thirty independent simulations. Each gap uses an independently constructed geometry, mesh, and S2S view-factor calculation (Section 3.3.5).

3.10.2 Airflow velocity

Table 3.14 reports the mean air-gap velocity across the parametric matrix. In all seasonal cases, U_{gap} decreases as the cavity width increases. Between $d = 0.10$ m and $d = 0.50$ m, the reduction is approximately 38–42% for the main irradiated cases, and about 27% for the spring overcast case. This behaviour is consistent with the wider channel allowing a larger flow cross-section but a lower mean velocity under the same buoyancy-driven pressure field.

Table 3.14: Air-gap velocity U_{gap} [$\mathrm{m\,s^{-1}}$] across the parametric matrix.

Design day	10 cm	15 cm	20 cm	30 cm	40 cm	50 cm
Winter Solstice	0.748	0.690	0.649	0.580	0.521	0.463
Spring, overcast	0.357	0.350	0.332	0.305	0.283	0.262
Spring, clear sky	0.936	0.865	0.805	0.706	0.621	0.540
Autumn Equinox	0.925	0.852	0.793	0.696	0.610	0.531
Summer Solstice	0.725	0.668	0.622	0.547	0.483	0.423

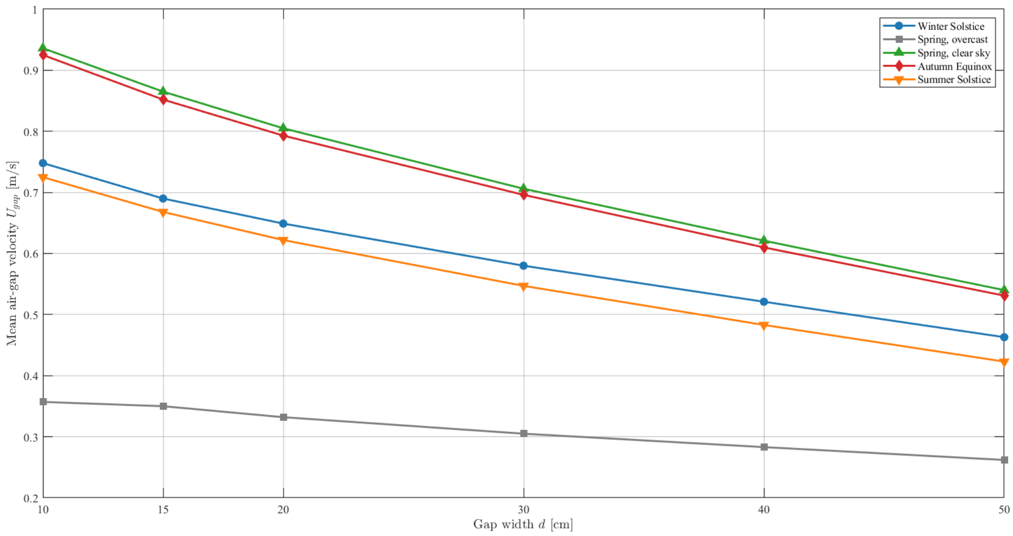

Figure 3.8: Air-gap velocity U_{gap} as a function of gap width, one curve per season.

3.10.3 Convective heat transfer coefficients

Table 3.15 reports h_{rear} across the parametric matrix. For all seasons in which the coefficient is well defined, h_{rear} shows an overall decreasing trend as the gap width increases, although small non-monotonic variations appear in some high-load cases. The relative reduction between $d = 0.10$ m and $d = 0.50$ m ranges from about 6% in Summer to about 31% in Winter. The spring overcast case is excluded from this comparison, consistently with Section 3.9, because the PV solid is close to thermal equilibrium with the cavity air.

Table 3.15: Rear-side convective heat transfer coefficient h_{rear} [$\mathrm{W\,m^{-2}\,K^{-1}}$] across the parametric matrix.

Design day	10 cm	15 cm	20 cm	30 cm	40 cm	50 cm
Winter Solstice	5.21	4.93	4.84	4.56	4.09	3.58
Spring, overcast	n.s.	n.s.	n.s.	n.s.	n.s.	n.s.
Spring, clear sky	6.77	6.78	6.75	6.29	6.10	5.66
Autumn Equinox	7.24	6.97	6.97	6.77	6.41	6.02
Summer Solstice	6.29	6.08	6.16	6.20	6.08	5.88

Table 3.16: Wall-side convective heat transfer coefficient h_{wall} [$\mathrm{W\,m^{-2}\,K^{-1}}$] across the parametric matrix.

Design day	10 cm	15 cm	20 cm	30 cm	40 cm	50 cm
Winter Solstice	1.76	1.79	1.75	1.68	1.58	1.48
Spring, overcast	1.89	1.82	1.74	1.61	1.46	1.33
Spring, clear sky	1.69	1.86	1.84	1.70	1.71	1.62
Autumn Equinox	1.51	1.57	1.56	1.52	1.47	1.39
Summer Solstice	1.41	1.47	1.48	1.49	1.48	1.45

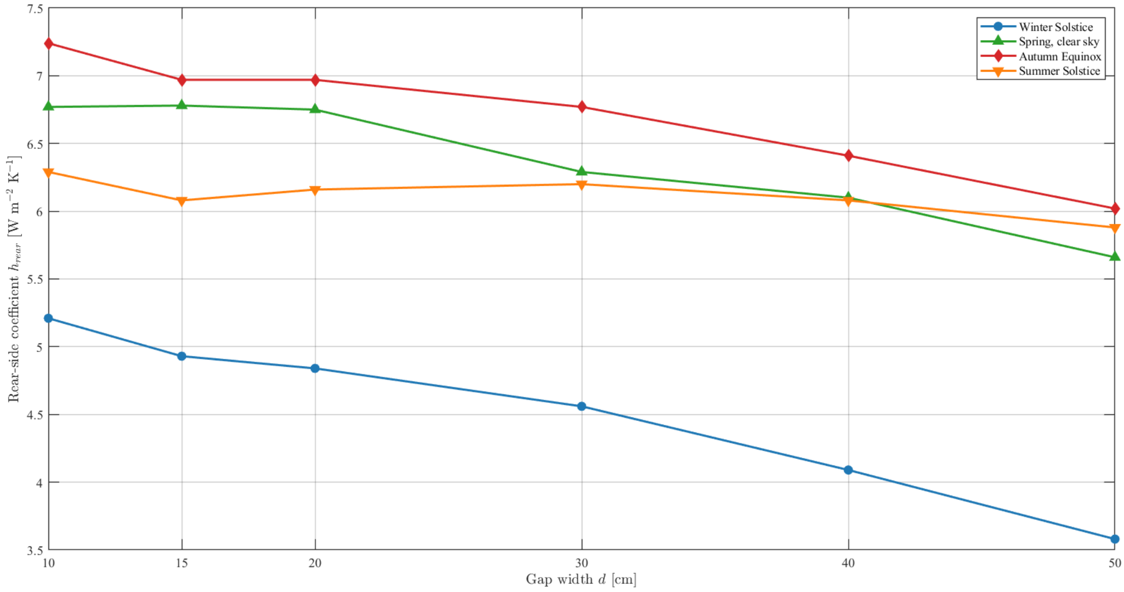

Figure 3.9: Rear-side convective heat transfer coefficient h_{rear} as a function of gap width, one curve per season (Spring overcast omitted, not significant).

3.10.4 PV temperature and vertical gradient

Table 3.17 reports the mean PV temperature, varying by less than 1 K across the full gap range in every season, in contrast to U_{gap} and h_{rear}. T_{PV} is therefore governed predominantly by the front-side energy balance and only weakly affected by d.

Table 3.17: Mean PV temperature T_{PV} [°C] across the parametric matrix.

Design day	10 cm	15 cm	20 cm	30 cm	40 cm	50 cm
Winter Solstice	−2.24	−2.10	−2.07	−1.95	−1.73	−1.47
Spring, overcast	0.59	0.60	0.63	0.72	0.82	0.93
Spring, clear sky	20.59	20.10	20.17	20.94	20.64	20.97
Autumn Equinox	28.16	28.30	28.42	28.58	28.81	29.20
Summer Solstice	40.60	40.70	40.66	40.67	40.73	40.84

Table 3.18: Vertical temperature gradient (bottom-to-top) [K] across the parametric matrix.

Design day	10 cm	15 cm	20 cm	30 cm	40 cm	50 cm
Winter Solstice	1.34	1.20	1.11	0.91	0.72	0.56
Spring, overcast	0.27	0.20	0.31	0.46	0.57	0.67
Spring, clear sky	2.20	1.79	1.39	0.83	0.40	−0.06
Autumn Equinox	2.55	2.03	1.56	0.92	0.43	−0.06
Summer Solstice	1.22	0.90	0.68	0.36	0.15	0.00

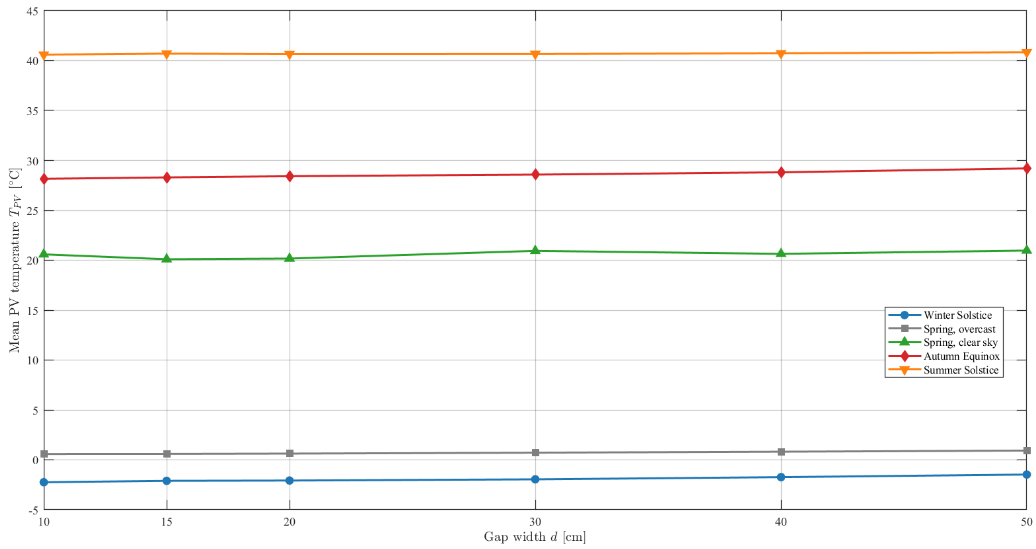

Figure 3.10: Mean PV temperature as a function of gap width, one curve per season.

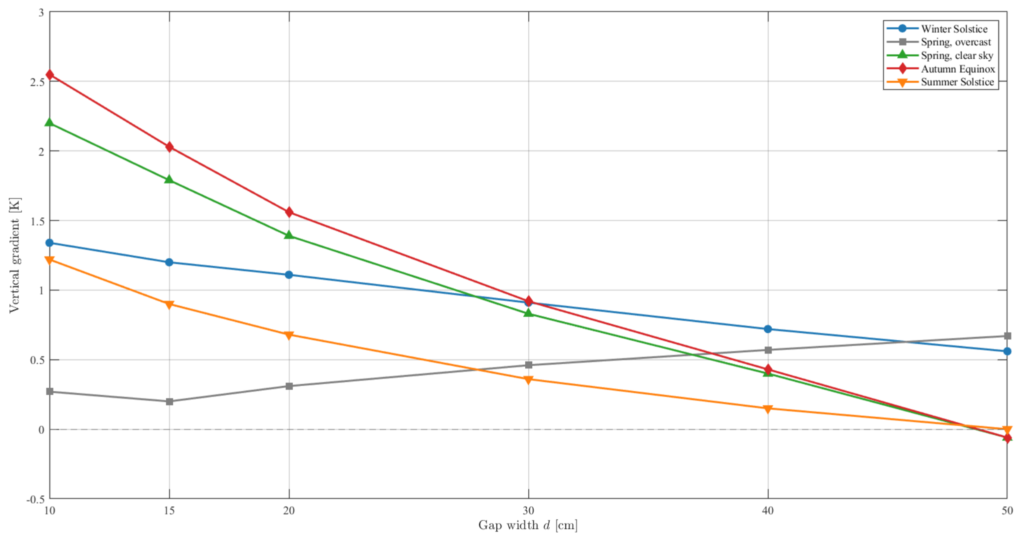

Figure 3.11: Vertical temperature gradient as a function of gap width, one curve per season.

3.10.5 Energy balance closure

The closure error remains below approximately 3.7% across the full thirty-case matrix. For most cases, the imbalance remains below 3%, with Winter, Spring clear and Autumn staying below 1.8% throughout. The largest deviations occur for the Spring overcast case, where the closure error ranges from 2.55% to 3.65%, as a consequence of the small absolute heat fluxes involved under this low-load design day. In Summer, the closure error increases with gap width from 1.0% to 2.83%, reflecting the growing convective enthalpy contribution as the cavity cross-section widens under sustained high thermal loading.

3.11 Thermal recovery and gap selection

3.11.1 Definition

The ventilated cavity can also be regarded as recovering part of the absorbed solar heat as warmed air, potentially extractable for use elsewhere in the building. This recovered power is

$$Q_{rec} = -\left(\dot{Q}_{inlet} + \dot{Q}_{outlet}\right) \tag{3.17}$$

evaluated at the peak-irradiance hour of each design day (Section 3.6.1); Q_{rec} is therefore an instantaneous peak power, not an annual energy yield, whose hourly integration belongs to the techno-economic phase of this work.

3.11.2 Results across the parametric matrix

Table 3.19 reports Q_{rec} across the thirty-case matrix of Section 3.10.

Table 3.19: Peak thermal recovery Q_{rec} [W] across the parametric matrix.

Design day	10 cm	15 cm	20 cm	30 cm	40 cm	50 cm
Winter Solstice	506	495	498	503	500	492
Spring, overcast	74	77	79	84	90	95
Spring, clear sky	951	939	939	919	821	863
Autumn Equinox	920	902	903	887	856	825
Summer Solstice	452	440	431	431	412	390

The recovery criterion below is defined from the perspective of heating-season usefulness, not annual heat extraction: Summer is excluded because, under cooling-dominated conditions, recovered heat would not represent a useful contribution to the building energy balance but an additional load. Table 3.20 reports the mean and sum of Q_{rec} over the four remaining seasons.

Table 3.20: Heating-season thermal recovery (Summer excluded), mean and sum over Winter, Spring overcast, Spring clear, Autumn.

	10 cm	15 cm	20 cm	30 cm	40 cm	50 cm
Mean Q_{rec} [W]	612.75	603.25	604.75	598.25	566.75	568.75
Sum Q_{rec} [W]	2451	2413	2419	2393	2267	2275

3.11.3 Gap selection

The mean heating-season recovery shows an overall decreasing trend with gap width, from 612.75 W at $d = 0.10$ m to 568.75 W at $d = 0.50$ m, corresponding to a reduction of about 7%. Although small non-monotonic variations appear between neighbouring gap values, the highest heating-season recovery is obtained for the narrowest investigated gap, $d = 0.10$ m. Within the investigated range and under the assumptions of buoyancy-driven, wind-free operation, this gap is therefore selected as the most favourable configuration for heating-season thermal recovery.

This selection entails no trade-off with electrical performance: Section 3.10 showed the mean PV temperature to be nearly independent of gap width (Table 3.17, variation below 1 K), so the temperature-dependent efficiency (Equation 3.4) is essentially unaffected by the choice of d. The thermal-recovery and electrical-efficiency criteria therefore converge on the same gap without requiring a compromise between the two. This conclusion is specific to the wind-free regime simulated here; its sensitivity to wind-assisted ventilation is discussed in Section 3.13.

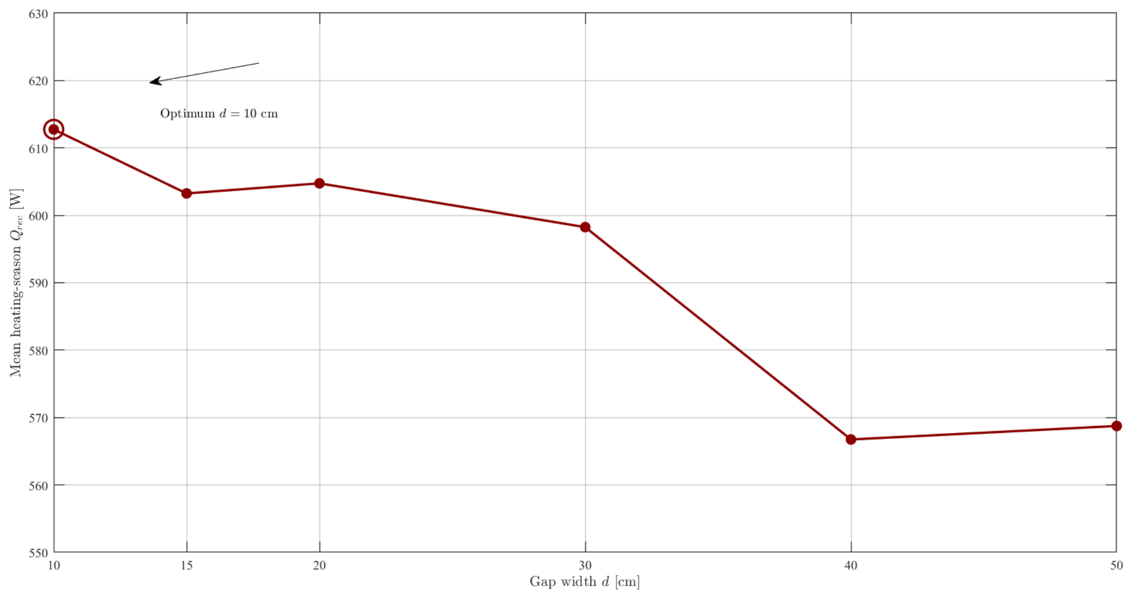

Figure 3.12: Heating-season mean thermal recovery Q_{rec} as a function of gap width, with the $d = 10$ cm result highlighted.

3.11.4 From peak power to daily thermal energy

The values of Q_{rec} reported in Table 3.19 represent instantaneous peak powers evaluated at the hour of maximum irradiance of each design day. In order to estimate the daily recoverable thermal energy, a linear scaling with respect to the hourly front irradiance profile is adopted:

$$E_{\text{rec,day}} = Q_{\text{rec,peak}} \cdot \frac{\sum_h G_{\text{front}}(h)}{\max_h G_{\text{front}}(h)} \cdot \Delta t \tag{3.18}$$

where $\Delta t = 1$ h and the summation is performed over all daylight hours of the design day. This assumption is physically motivated by the dominant role of solar absorption in driving heat generation within the ventilated cavity: the recovered thermal power is primarily determined by the incident solar irradiance, and the linear proportionality provides a reasonable first-order approximation of the intra-day variation of Q_{rec}. Non-linear effects arising from variations in the convective regime and cavity air temperature throughout the day are neglected under this approximation and are identified as a source of uncertainty in the estimate.

The daily recoverable thermal energy obtained from Equation (3.18) for the three-panel CFD model, evaluated at the optimal air-gap configuration of $d = 10$ cm, is reported in Table 3.21 for each design day.

Table 3.21: Daily recoverable thermal energy for the three-panel CFD model per design day (optimal gap $d = 10$ cm).

Design day	$Q_{\text{rec,peak}}$ **[W]**	$E_{\text{rec,day}}$ **[Wh]**
Winter Solstice	506	1,911
Spring clear sky	951	6,685
Autumn Equinox	920	4,334
Summer Solstice	452	3,378

These values constitute the per-day thermal energy output of the simulated three-panel system and are used as input to the techno-economic analysis of Chapter 4, where they are scaled to the full building installation and extrapolated to the annual heating season.

3.12 Discussion

3.12.1 Solar chimney mechanism and gap dependence

The results of Sections 3.9–3.10 reflect a single mechanism: buoyancy from the heated PV rear surface drives an upward flow whose velocity, and hence convective coupling, decreases as the gap widens (Tables 3.14–3.15), while T_{PV} itself remains governed primarily by the front-side energy balance and is largely insensitive to d (Table 3.17). This decoupling between the fluid-dynamic response (strongly gap-dependent) and the thermal load (weakly gap-dependent) is the physical basis for the absence of a trade-off in the gap selection of Section 3.11.

3.12.2 Heat removal partitioning

The benchmark energy balance (Table 3.9) partitions the absorbed solar power among its three pathways: approximately 70 % rejected from the PV front to the sky, approximately 27 % carried by the cavity airflow (Q_{rec}, Equation 3.17), and the remaining 4 % conducted through the wall. The front surface remains the dominant pathway, but cavity ventilation contributes a non-negligible secondary mechanism, consistent with its role as the basis for the thermal-recovery criterion of Section 3.11.

3.12.3 Literature comparison

The ventilated cavity studied here is geometrically and physically analogous to a naturally ventilated double-skin façade (DSF): a narrow, buoyancy-driven air channel bounded by a solar-heated outer skin and a building wall. The CFD literature on ventilated BIPV and double-skin cavities [47, 74] is therefore directly applicable to the present configuration. The rear-side coefficients obtained here (h_{rear} = $3.58\,\mathrm{W\,m^{-2}\,K^{-1}}$ to $7.24\,\mathrm{W\,m^{-2}\,K^{-1}}$ across the full matrix, Table 3.15) fall within the range typically reported for buoyancy-driven ventilated cavities of comparable geometry [47], and the monotonic decrease of U_{gap}, together with the overall decreasing trend of h_{rear} as the gap width increases, reproduces the qualitative behaviour established in that literature for wind-free ventilation. This correspondence supports treating the bifacial BIPV cavity as a special case of the broader ventilated-façade problem, in which the bifacial electrical coupling (Section 3.2) is superimposed on an otherwise conventional solar-chimney flow.

3.12.4 Lumped vs. CFD-resolved temperature

The systematic overestimation of T_{PV} by the lumped correlation (Section 3.9, Table 3.13) demonstrates the limitation motivating the present CFD analysis: an effective empirical heat-loss correlation cannot explicitly capture the additional cooling pathway provided by the ventilated rear cavity. Because this discrepancy varies by nearly a factor of three across seasons, a single constant correction offset would not adequately capture it; the CFD-resolved field is necessary, not merely more accurate, whenever the cavity's contribution to module cooling is of interest.

3.12.5 Implications for gap selection

The gap-selection result is not counterbalanced by an electrical-efficiency penalty: since T_{PV} varies by less than about 1 K across the investigated gap range, the temperature-dependent electrical efficiency is only weakly affected by d. The electrical behaviour therefore does not introduce a meaningful trade-off against the thermal-recovery benefit of the narrowest gap.

3.13 Model limitations

The CFD model presented in this chapter is subject to a number of limitations, stated here for completeness.

L1) Two-dimensional domain. The façade is modelled as a two-dimensional section (Section 3.3), neglecting lateral edge effects and any three-dimensional flow structure near the boundaries of the module array. This is expected to be a good approximation away from the lateral edges of a real, multi-column installation.

L2) Steady-state, representative operating points. Each of the thirty simulations represents a single steady-state snapshot at the peak-irradiance hour of one design day (Section 3.6.1), not a time-resolved simulation of the full annual record; sub-hourly transients in irradiance and wind are not captured.

L3) Wind-free natural ventilation. All simulations represent buoyancy-driven ventilation with no imposed wind inside the cavity; wind enters only through the front-side convective boundary condition (Equation 3.14), not as a driver of flow through the gap. Wind-assisted ventilation would alter the coefficients of Sections 3.9–3.10 and could affect the gap selection of Section 3.11.

L4) Constant thermophysical properties. All properties other than the Boussinesq buoyancy term are held constant at a single reference temperature $T_0 \approx 284.4\,\mathrm{K}$, fixed from the Autumn benchmark case and applied unchanged across the full seasonal range (Section 3.5.1). Since $\beta = 1/T$ for an ideal gas, this introduces an asymmetric bias in the effective thermal expansion coefficient relative to the locally correct value: approximately 4.5 % at the Winter extreme ($T \approx 271\,\mathrm{K}$) and −9.8 % at the Summer extreme ($T \approx 314\,\mathrm{K}$), corresponding to a mild underestimation of buoyancy forcing in Winter and overestimation in Summer. This is judged to lie within the overall numerical uncertainty of the model (energy-balance closure below about 3.7% across the full simulation matrix, and below 3% for most cases) but was not independently verified against a temperature-dependent property set.

L5) Homogenised solid regions. The PV and the wall are each represented as a single homogeneous solid with effective properties (Sections 3.5.3–3.5.4), rather than as their true multilayer constructions, and do not resolve any internal temperature gradient across individual layers.

L6) One-way optical-to-CFD coupling. The volumetric source terms are computed from a lumped temperature estimate $T_{PV,lumped}$ that is not updated using the CFD-resolved field (Section 3.2). Section 3.9 quantified the resulting discrepancy at 2.17–6.03 K across the five seasons; a fully coupled, iterative scheme would remove this inconsistency, at substantially higher computational cost given the thirty-case matrix already required under the present approach.

L7) Absence of experimental validation. Consistent with the optical-electrical model of Chapter 2, no experimental measurements are available for this façade configuration. The checks of Section 3.8 establish internal numerical consistency (energy conservation, mesh independence, correct implementation of the source coupling) but do not constitute validation against measured data; results should be interpreted as a theoretical and comparative assessment of gap-width and seasonal trends, consistent with the same caveat in Chapter 2 (limitation L5).

Notwithstanding these limitations, the model fulfils its intended purpose: it resolves the coupled conduction-convection-radiation behaviour of the ventilated cavity from first principles, quantifies the convective heat transfer coefficients required by the thermal analysis, and identifies a gap width that jointly maximises heating-season thermal recovery and preserves electrical performance within the assumptions stated above.

Chapter 4

Techno-Economic Analysis

4.1 Introduction and Objectives

The optical, electrical and thermal models developed in the previous chapters provide a comprehensive characterisation of the energy performance of building-integrated bifacial photovoltaic systems under Nordic climatic conditions. However, the technical feasibility of a BIPV installation is a necessary but not sufficient condition for its deployment: an assessment of economic viability is equally required in order to determine whether the proposed systems can represent a financially attractive investment over their lifetime.

This chapter presents a techno-economic analysis of two BIPV case studies representative of different building typologies in Finland. The first case study corresponds to the Maarintie 8 building located on the Aalto University campus in Espoo, selected as a representative example of a large public educational facility characterised by high annual electricity demand and an extensive south-oriented brick façade suitable for photovoltaic integration. The second case study considers a multi-family residential building equipped with balcony-integrated photovoltaic modules, representing a typical residential application in the Finnish built environment.

The two case studies were selected to investigate the applicability of BIPV systems across different scales, integration strategies and building uses, and to assess how these factors influence the economic performance of the proposed installations. While the university building adopts a ventilated façade configuration that fully exploits the bifacial nature of the modules, the residential case integrates the photovoltaic panels into building balconies in a laterally mounted configuration, where the contribution of rear-side irradiance is negligible. This distinction has direct implications for the economic comparison between bifacial and monofacial configurations, which is carried out exclusively for the university building.

For the university case study, the economic advantage of the bifacial system over an equivalent monofacial configuration is assessed by considering two distinct contributions. The first is the additional electrical energy produced by the rear surface of the modules, quantified by the bifacial gain calculated in Chapter 2. Although this gain is relatively modest under the vertical façade conditions considered here, it represents a direct and measurable benefit of bifacial technology. The second contribution is the thermal energy recoverable from the ventilated air gap, which accumulates between the photovoltaic modules and the building wall as a consequence of the heat generated within the cavity. This thermal benefit, absent in a conventional monofacial reference scenario, is valorised as a saving on district heating costs and represents a significant additional advantage of the bifacial ventilated façade configuration under Finnish climatic conditions.

In addition to the electrical energy savings associated with self-consumption, the university case study includes an assessment of the thermal energy recoverable from the ventilated air gap, following the suggestion of the project supervisor. The recovered heat, generated within the cavity between the photovoltaic modules and the building wall, is valorised as a saving on district heating costs, which represents the dominant space heating vector in Finnish buildings.

The economic performance of both installations is evaluated using a discounted cash flow approach, considering the initial investment, annual operating and maintenance costs, inverter replacement, module degradation, electricity price escalation and, for the university case, thermal energy savings. Four economic indicators are computed: Net Present Value (NPV), Internal Rate of Return (IRR), Discounted Payback Time (DPBT) and Levelized Cost of Electricity (LCOE). A sensitivity analysis is subsequently performed to evaluate the robustness of the results against uncertainties in the two most influential economic parameters, namely the total investment cost and the electricity price.

The analysis follows the methodological framework proposed by Corti et al. [59] for the economic assessment of BIPV façade case studies, adapted to the Finnish regulatory and market context. The economic performance of the proposed systems is finally discussed in comparison with reference values from the Nordic literature, in particular the Solsmaragden BIPV façade case study in Norway [58], in order to contextualise the obtained results within the broader landscape of high-latitude BIPV applications.

4.2 Methodology

4.2.1 Economic Framework

The economic assessment adopts a discounted cash flow (DCF) approach, discounting future cash flows to the present at a given discount rate. The net cash flow in year t

is:

$$CF_t = CI_t - CO_t \tag{4.1}$$

where CI_t and CO_t are the annual cash inflows and outflows. The annual electricity savings are:

$$CI_t^{\text{elec}} = E_1 \cdot (1 - D)^t \cdot p_e \cdot (1 + \delta)^t \tag{4.2}$$

where E_1 is the first-year electricity production, D the annual module degradation rate, p_e the reference electricity price and δ the annual price escalation rate. For the university case study, thermal savings from heat recovery are added to the cash inflow:

$$CI_t^{\text{thermal}} = Q_{\text{rec}} \cdot \eta_{\text{rec}} \cdot p_{\text{DH}} \tag{4.3}$$

where Q_{rec} is the annual recoverable heat, η_{rec} the heat recovery efficiency and p_{DH} the district heating price. Annual cash outflows are:

$$CO_t = C_{\text{OPEX}} + C_{\text{inv}} \cdot \mathbf{1}_{t=15} \tag{4.4}$$

where C_{OPEX} is the annual operation and maintenance cost and C_{inv} the inverter replacement cost, applied only in year 15.

4.2.2 Economic Indicators

Profitability is evaluated using four indicators widely adopted for renewable energy systems. The **Net Present Value** (NPV) is the cumulative discounted cash flow over the project lifetime:

$$\text{NPV} = -I_0 + \sum_{t=1}^{N} \frac{CF_t}{(1 + r)^t} \tag{4.5}$$

where I_0 is the initial investment (CAPEX), r the discount rate and N the project lifetime in years. The **Internal Rate of Return** (IRR) is the discount rate r^* that sets the NPV to zero:

$$0 = -I_0 + \sum_{t=1}^{N} \frac{CF_t}{(1 + r^*)^t} \tag{4.6}$$

The **Discounted Payback Time** (DPBT) is the year T^* in which the cumulative discounted cash flow first becomes positive:

$$T^* = \min \left\{ T : -I_0 + \sum_{t=1}^{T} \frac{CF_t}{(1+r)^t} \geq 0 \right\} \tag{4.7}$$

The **Levelized Cost of Electricity** (LCOE) is the discounted lifetime cost of electricity generation per unit of energy produced:

$$\text{LCOE} = \frac{\sum_{t=0}^{N} \frac{C_t}{(1+r)^t}}{\sum_{t=1}^{N} \frac{E_t}{(1+r)^t}} \tag{4.8}$$

where C_t is the total annual cost in year t and E_t the annual electricity production.

4.2.3 CAPEX Breakdown

The capital expenditure (CAPEX) is divided into five cost categories: photovoltaic modules, supporting substructure and anchors, inverter, installation and cabling, and planning, permits and grid connection. All components are referred to the installed façade area in €/m^2 and the total investment includes the Finnish VAT of 24%. The breakdown, common to both case studies to ensure a directly comparable assessment, is reported in Table 4.1; its sensitivity is examined in Section 4.5.

Table 4.1: CAPEX breakdown adopted for both case studies.

Cost component	**Reference**	**Value**	**Unit**
PV modules	[56]	26.31	€/m^2
Substructure and anchors	[59]	90.00	€/m^2
Inverter	[57]	6.22	€/m^2
Installation and cabling	[64]	40.00	€/m^2
Planning, permits and grid connection	[59]	9.00	€/m^2
Total (excl. VAT)		171.53	€/m^2
Total (incl. 24% VAT)		212.70	€/m^2

4.2.4 Economic Assumptions

Table 4.2 summarises the economic parameters adopted in the DCF analysis. The 7% discount rate and 2.5% annual price escalation are representative of Finnish renewable energy investment conditions [63], and the 85 €/MWh electricity price is the Finnish commercial tariff reported by Eurostat [55]. The 0.5% per year degradation rate follows the manufacturer datasheet, consistent with the Solsmaragden case study [58]; OPEX and inverter replacement assumptions follow Corti et al. [59].

Table 4.2: Economic assumptions adopted in the techno-economic analysis.

Parameter	**Reference**	**Value**	**Unit**
Project lifetime	[58]	30	years
Discount rate	[63]	7	%
Electricity price	[55]	85	€ /MWh
Electricity price escalation	[63]	2.5	% per year
PV degradation rate	[58]	0.5	% per year
VAT		24	%
Annual OPEX	[59]	0.5	% of CAPEX
Inverter replacement	[59]	10	% of CAPEX (year 15)

4.2.5 Heat Recovery Assessment

For the university case study, the thermal energy recoverable from the ventilated air gap is included as an additional cash inflow, valorised as a saving on district heating costs, the dominant space heating vector in Finnish buildings, supplying approximately 45% of total space heating demand [61].

The recoverable heat is estimated from the CFD simulations of Chapter 3, which provide the hourly thermal power generated within the ventilated cavity for each seasonal benchmark day. Since space heating is required only during the heating season, thermal recovery is considered exclusively for the autumn and winter periods.

A heat recovery efficiency of $\eta_{\text{rec}} = 0.70$ is assumed, consistent with typical air-to-air heat recovery systems in the literature [60], and a district heating price of 101 € /MWh is adopted, based on the average price reported by Finnish Energy for 2023 [61]. These assumptions are summarised in Table 4.3.

Table 4.3: Heat recovery assessment parameters – university building case study.

Parameter	Reference	Value	Unit
Seasons considered	–	Autumn, Winter	–
Annual recoverable heat	CFD (Ch. 3)	56.6	MWh /year
Heat recovery efficiency	[60]	70	%
Effective recovered heat	–	39.6	MWh /year
District heating price	[61]	101	€ /MWh
Annual thermal saving	–	4,002	€ /year

The heat recovery assessment presented here is a simplified first-order estimate: the annual recoverable heat is derived from CFD simulations for representative seasonal benchmark days and extrapolated to the full heating season. A detailed hour-by-hour simulation of the thermal recovery over the entire year, including the cost and integration of a dedicated heat recovery system, falls outside the scope of the present work and is identified as a direction for future research.

4.3 University Building Case Study (Maarintie 8)

4.3.1 Building Description and BIPV Layout

The first case study considers the Maarintie 8 building on the Aalto University campus in Espoo, Finland, a large educational facility with an annual electricity demand of 1.9 GWh year^{-1} (project supervisor's consumption database) and a wide south-oriented brick façade suitable for photovoltaic integration. Façade dimensions, determined from Google Earth Pro measurements across five brick sections separated by non-usable glazed areas, yield a total available area of approximately 852 m^2. The photovoltaic layout, designed to maximise use of the available surfaces while avoiding windows and architectural elements, comprises 300 modules (Leapton LP182-54, 500 W TOPCon) for an installed capacity of 150 kWp, covering approximately 78% of the available brick façade area. The main geometric and layout parameters are summarised in Table 4.4.

Table 4.4: BIPV layout parameters – university building case study.

Parameter	Value	Unit
Total available façade area	852	m^2
Façade coverage	78	%
Number of PV modules	300	–
Installed capacity	150	kWp
Module dimensions	1961 × 1134 × 30	mm
Module orientation	Portrait	–

Figure 4.1: Illustrative AI rendering of the proposed BIPV layout on the south façade of the Maarintie 8 university building.

4.3.2 Energy Assessment

The energy performance of the proposed BIPV system was evaluated using the simulation framework developed in Chapters 2 and 3. The final installation, consisting of 300 photovoltaic modules with a total installed capacity of 150 kWp, generates an annual electricity production of 127,071 kWh /year, corresponding to a specific energy yield of 847 kWh /kWp/ year. This value is consistent with the expected performance of south-oriented façade-integrated photovoltaic systems operating under Finnish climatic conditions [50].

Since the annual electricity demand of the building (1.9 GWh /year) is significantly higher than the annual PV production, all the electricity generated by the BIPV installation is assumed to be directly self-consumed, resulting in a self-consumption ratio of 100%. Consequently, no electricity export to the grid is considered in the economic assessment.

The daily thermal energy values obtained from the three-panel CFD model (Section 3.11.4) are scaled to the full university building installation and extrapolated to the annual heating season through the following procedure.

The CFD model simulates a system of three panels over a façade of 6.5 m height and 1.134 m width, corresponding to an active PV area of approximately 6.67 m^2. The full university building installation consists of 300 panels with a total active area of 667 m^2, yielding a geometric scaling factor of 100. The daily thermal energy of the full installation is therefore obtained by multiplying the per-model daily energy by this factor:

$$E_{\mathrm{rec,day}}^{300} = E_{\mathrm{rec,day}}^{3} \times 100 \tag{4.9}$$

This scaling implicitly assumes that the thermal behaviour of each panel is independent of its position within the array, which is a reasonable first approximation given the uniform south orientation of the façade.

The annual thermal energy is estimated by assigning each design day to a representative number of days within its season, as reported in Table 4.5. Two seasons are excluded from the heating-season valorisation on the following grounds.

Summer is excluded because recovered heat during the cooling-dominated period would not represent a useful contribution to the building energy balance but rather an additional thermal load under Finnish climatic conditions [61].

Spring is excluded as a conservative measure: the only available representative day is a clear-sky condition (Spring clear sky, 22 March), which would likely overestimate the recoverable energy for the entire spring season given the highly variable cloud cover typical of Finnish spring conditions. Other potential uses of the recovered heat beyond space heating, such as domestic hot water production or pre-heating of ventilation air, are outside the scope of the present work and are identified as directions for future research.

The heating season is therefore conservatively defined as winter and autumn, corresponding to the period from October to April in which space heating is most consistently required under Finnish climatic conditions.

Table 4.5: Seasonal extrapolation of daily thermal energy to annual yield – full 300-panel installation.

Season	**Representative day**	$E^{3}_{\text{rec,day}}$ **[Wh]**	$E^{300}_{\text{rec,day}}$ **[kWh]**	**Days**	**Included**
Winter	Winter Solstice	1,911	191.1	90	✓
Spring	Spring clear sky	6,685	668.5	92	×
Autumn	Autumn Equinox	4,334	433.4	91	✓
Summer	Summer Solstice	3,378	337.8	92	×

The heating-season recoverable thermal energy for the full installation is therefore:

$$E_{\text{rec,heating}} = (191.1 \times 90 + 433.4 \times 91) \times 10^{-3} \approx 56.6 \text{ MWh year}^{-1} \tag{4.10}$$

Applying the assumed heat recovery efficiency of $\eta_{\text{rec}} = 0.70$ and the Finnish district heating price of $p_{\text{DH}} = 101$ € MWh^{-1} [61], the resulting annual thermal saving is:

$$S_{\text{thermal}} = E_{\text{rec,heating}} \cdot \eta_{\text{rec}} \cdot p_{\text{DH}} = 56.6 \times 0.70 \times 101 \approx 4{,}002 \text{ € year}^{-1} \tag{4.11}$$

This value is included as an additional annual cash inflow in the discounted cash flow analysis of Section 4.2. It should be noted that no dedicated heat recovery system is explicitly modelled or costed in the present analysis; the thermal savings should therefore be interpreted as an upper bound on the recoverable benefit, subject to the efficiency and cost of the actual recovery system adopted. This limitation is discussed further in Section 4.6.

Table 4.6: Energy performance indicators – university building case study.

Parameter	Value	Unit
Annual electricity demand	1,900,000	kWh /year
Annual PV electricity production	127,071	kWh /year
Specific energy yield	847	kWh /kWp/year
Self-consumption ratio	100	%
Annual recoverable heat (raw)	56.6	MWh /year
Effective recovered heat	39.6	MWh /year
Annual thermal saving	4,002	€ /year

4.3.3 Economic Assessment

The economic performance of the proposed BIPV installation was evaluated according to the methodology described in Section 4.2. The discounted cash flow analysis accounts for the initial investment cost, annual operating and maintenance expenses, inverter replacement in year 15, module degradation, electricity price escalation and the thermal savings associated with heat recovery from the ventilated air gap.

The total CAPEX including 24% VAT amounts to 141,897 €, corresponding to an annual OPEX of 709 € /year. The main economic results are summarised in Table 4.7.

Table 4.7: Economic results – university building case study.

Parameter	Value	Unit
CAPEX (incl. 24% VAT)	141,897	€
Annual OPEX	709	€ /year
Net Present Value (NPV)	21,582	€
Internal Rate of Return (IRR)	9	%
Discounted Payback Time (DPBT)	21	years
Levelized Cost of Electricity (LCOE)	0.100	€ /kWh

Figure 4.2 illustrates the cumulative discounted cash flow over the 30-year project lifetime.

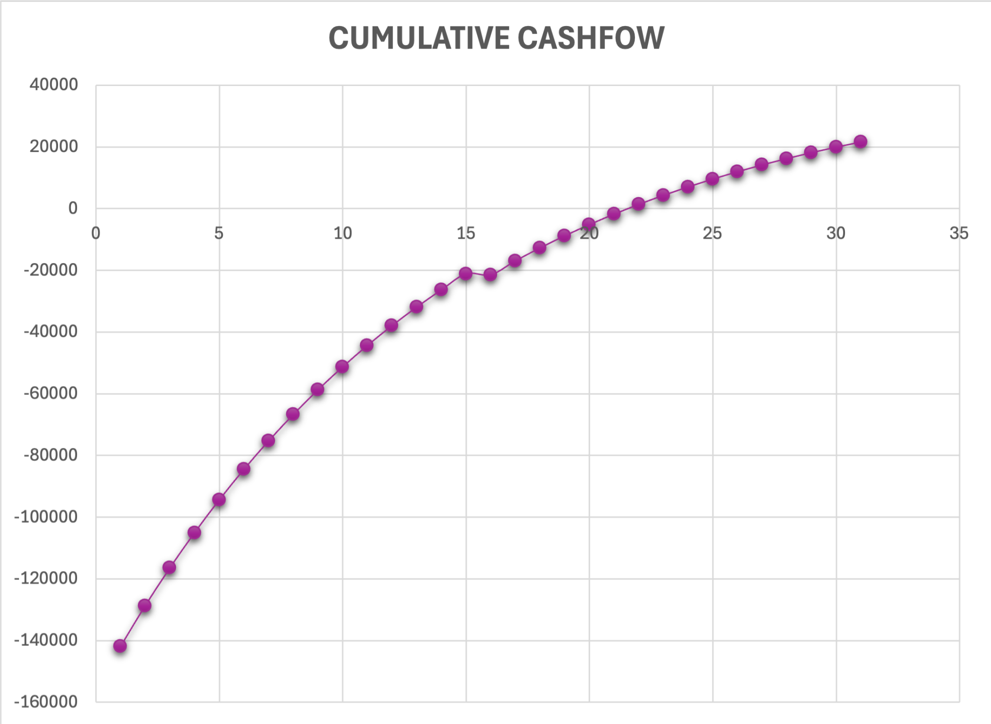

Figure 4.2: Cumulative discounted cash flow over the project lifetime – university building case study.

4.3.4 Bifacial Advantage Assessment

The economic advantage of the bifacial ventilated façade system over a conventional monofacial reference is assessed by considering two distinct contributions, as described in Section 4.2: the additional electrical energy associated with the bifacial gain, and the thermal energy savings enabled by the ventilated air gap configuration.

The bifacial gain of approximately 3.5% computed by the optical model (Chapter 2) corresponds to an additional annual electricity production of approximately 4,330 kWh /year with respect to the monofacial reference. At the assumed electricity price of 85 € /MWh, this translates into an additional annual saving of approximately 368 € /year.

The thermal energy savings from heat recovery, amounting to 4,002 € /year, represent a significantly larger economic benefit, confirming that the ventilated air gap configuration provides a substantial additional advantage over a flush-mounted monofacial system. The combined annual economic benefit of bifaciality, electrical and thermal, therefore amounts to approximately 4,370 € /year, corresponding to an increase of approximately 41% in the annual cash inflow compared to the monofacial electrical-only scenario.

These results highlight that, under the climatic and economic conditions considered here, the thermal recovery from the ventilated air gap is the dominant driver of the economic advantage of the bifacial system, while the bifacial gain contributes a smaller but non-negligible additional benefit.

4.4 Residential Building Case Study

4.4.1 Building Description and BIPV Layout

The second case study considers a multi-family residential building representative of typical Finnish apartment blocks: seven floors, fourteen apartments of approximately 120 m^2 each, and an assumed occupancy of four residents per apartment (56 occupants total). Based on the average annual consumption of 19 MWh per fully electrified apartment reported by the Finnish electricity supplier Vaasan Sähkö [62], the total annual electricity demand amounts to 266 MWh /year. Following Xiang and Matusiak [65], who identify laterally integrated balcony modules as a favourable BIPV solution for Nordic residential buildings, four photovoltaic modules were installed on each balcony, resulting in 56 PV modules and an installed capacity of 28 kWp. The main layout parameters are summarised in Table 4.8.

Table 4.8: BIPV layout parameters – residential building case study.

Parameter	Value	Unit
Number of floors	7	–
Number of apartments	14	–
Modules per balcony	4	–
Total number of PV modules	56	–
Installed capacity	28	kWp
Module orientation	Lateral	–

Figure 4.3: Illustrative AI rendering of the proposed balcony-integrated BIPV configuration for the residential building case study.

It should be noted that, due to the lateral balcony mounting configuration, the rear surface of the photovoltaic modules receives negligible irradiance. Consequently, the bifacial nature of the selected modules cannot be effectively exploited in this application, and the energy yield is essentially equivalent to that of a monofacial system. For this reason, no bifacial advantage assessment is carried out for the residential case study.

4.4.2 Energy Assessment

The photovoltaic system consists of 56 BIPV modules, corresponding to four modules installed on the balcony of each apartment. The annual electricity production estimated with the optical model amounts to 23,746 kWh /year, corresponding to a specific energy yield of 848 kWh /kWp/ year. This value is remarkably consistent with the specific yield obtained for the university building (847 kWh /kWp/ year) despite the different integration strategy, confirming the coherence of the simulation framework across the two case studies.

The annual electricity demand of the residential building (266 MWh /year) is significantly higher than the electricity generated by the BIPV system. Therefore, all the electricity produced is assumed to be directly self-consumed, resulting in a self-consumption ratio of 100%. No electricity export to the grid is considered in the economic assessment. The main energy performance indicators are summarised in Table 4.9.

Table 4.9: Energy performance indicators – residential building case study.

Parameter	Value	Unit
Annual electricity demand	266,000	kWh/ year
Annual PV electricity production	23,746	kWh/ year
Specific energy yield	848	kWh/ kWp/year
Self-consumption ratio	100	%

4.4.3 Economic Assessment

The economic performance of the proposed residential BIPV installation was evaluated following the methodology described in Section 4.2. The discounted cash flow analysis considers the initial investment cost, annual operating and maintenance expenses, inverter replacement in year 15, module degradation and electricity price escalation. No thermal savings are included for the residential case, as the balcony-integrated configuration does not feature a ventilated air gap from which heat can be recovered.

The total CAPEX including 24% VAT amounts to 21,469 €, corresponding to an annual OPEX of 107 €/ year. The main economic results are summarised in Table 4.10.

Table 4.10: Economic results – residential building case study.

Parameter	Value	Unit
CAPEX (incl. 24% VAT)	21,469	€
Annual OPEX	107	€ /year
Net Present Value (NPV)	7,142	€
Internal Rate of Return (IRR)	10	%
Discounted Payback Time (DPBT)	19	years
Levelized Cost of Electricity (LCOE)	0.08	€/ kWh

Figure 4.4 illustrates the cumulative discounted cash flow over the 30-year project lifetime.

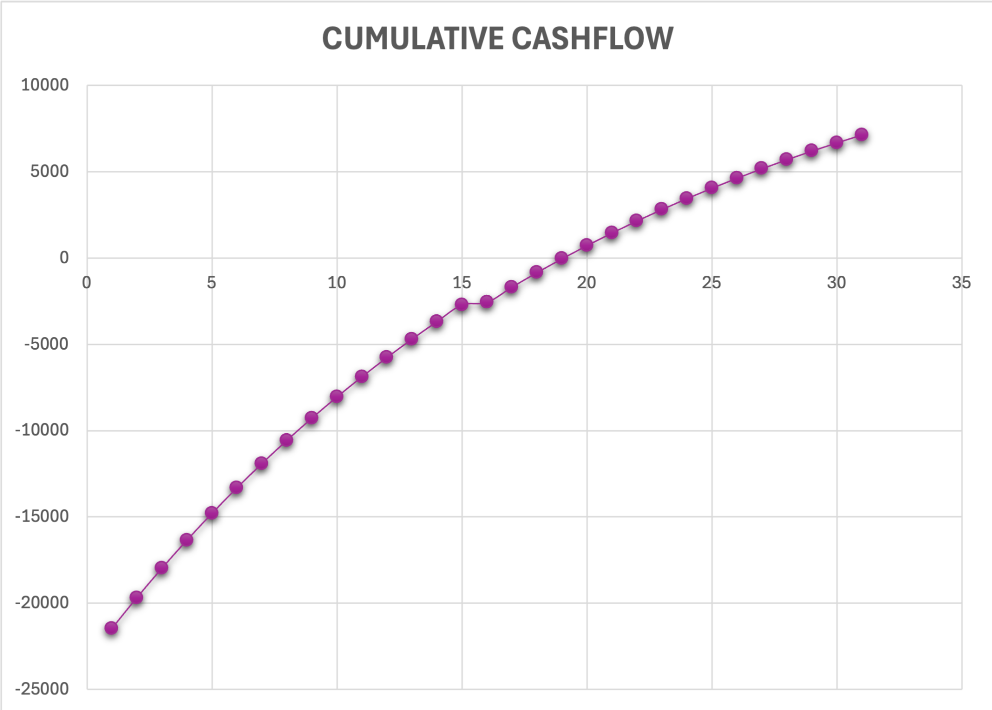

Figure 4.4: Cumulative discounted cash flow over the project lifetime – residential building case study.

The obtained results indicate that the proposed balcony-integrated BIPV system is economically attractive under the adopted assumptions. The positive NPV of 7,142 € confirms the profitability of the investment over the project lifetime, while the IRR of 10% significantly exceeds the assumed discount rate of 7%, indicating a satisfactory return on investment. Compared with the university case study, the residential installation achieves a considerably shorter discounted payback time of 19 years, mainly due to the substantially lower initial investment required. The calculated LCOE of 0.08 € /kWh is lower than the assumed electricity purchase price of 0.085 € /kWh, confirming that the system is capable of producing electricity at a competitive cost under the considered Finnish conditions.

4.5 Sensitivity Analysis

4.5.1 Methodology

A sensitivity analysis, following the methodology of Corti et al. [59], evaluates the robustness of the results against uncertainty in the two economic parameters expected to have the largest impact on profitability: the total investment cost (CAPEX) and the electricity price. Both are varied independently from −20% to +20% in 5% increments, with all other assumptions held constant, and the resulting NPV variation is evaluated for both case studies. CAPEX uncertainty reflects the project-specific nature of BIPV installation costs (substructure, installation and grid connection depend strongly on local practices), while electricity price uncertainty reflects market volatility over the 30-year project horizon.

4.5.2 CAPEX Sensitivity

The results of the CAPEX sensitivity analysis are reported in Table 4.11 and illustrated in Figure 4.5.

Table 4.11: CAPEX sensitivity analysis – NPV variation for both case studies.

CAPEX variation	Residential			University		
	CAPEX [€]	NPV [%]	NPV [€]	CAPEX [€]	NPV [%]	NPV [€]
−20%	17,175	+66%	11,859	113,518	+144%	52,751
−15%	18,249	+49%	10,680	120,613	+108%	44,959
−10%	19,322	+33%	9,500	127,708	+72%	37,166
−5%	20,396	+16%	8,321	134,803	+36%	29,374
Reference case	21,469	0%	7,142	141,897	0%	21,582
+5%	22,542	−16%	5,963	148,992	−36%	13,790
+10%	23,616	−33%	4,785	156,087	−72%	5,998
+15%	24,689	−49%	3,606	163,182	−108%	−1,795
+20%	25,763	−66%	2,426	170,277	−144%	−9,587

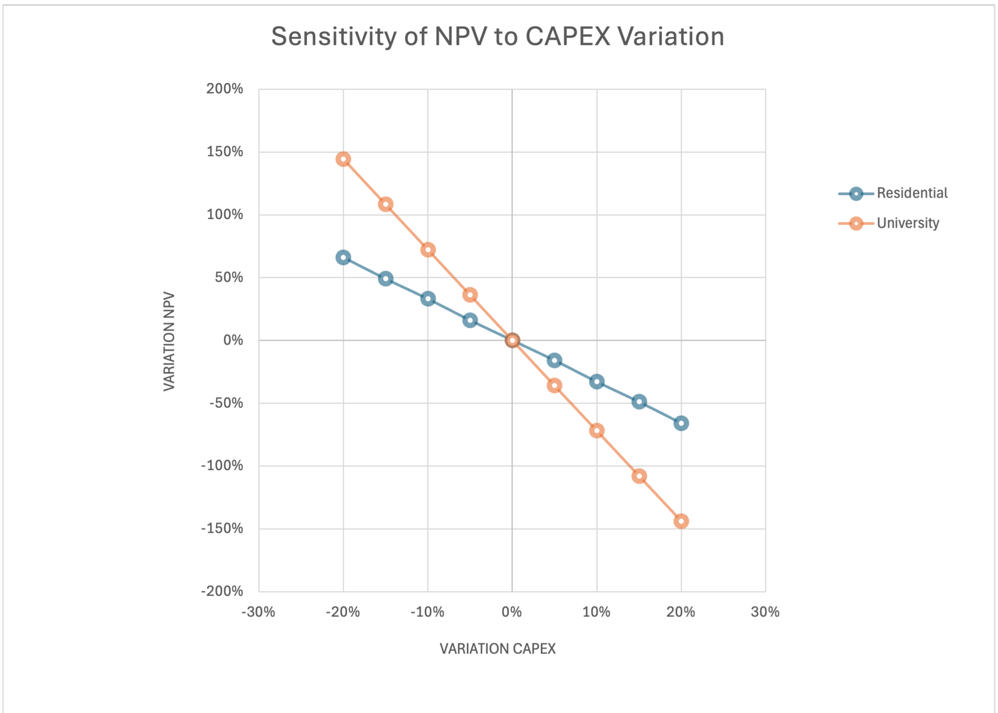

Figure 4.5: Sensitivity of the NPV to CAPEX variations for the university and residential case studies.

As expected, higher CAPEX reduces NPV and lower CAPEX improves it, but the two case studies respond very differently. The university installation is highly sensitive: NPV swings by about ±144% for a ±20% CAPEX change and already turns negative at +15%, reflecting its large absolute investment and limited margin for cost overruns. The residential installation is comparatively robust, remaining positive across the full range (swing of about ±66%), owing to its much lower investment. Balcony-integrated systems therefore appear more financially resilient to cost uncertainty, while façade-scale installations require tighter cost control.

4.5.3 Electricity Price Sensitivity

The results of the electricity price sensitivity analysis are reported in Table 4.12 and illustrated in Figure 4.6.

Table 4.12: Electricity price sensitivity analysis – NPV variation for both case studies.

Electricity price variation	**Residential**			**University**		
	Price [€/kWh]	NPV [%]	NPV [€]	Price [€/kWh]	NPV [%]	NPV [€]
−20%	0.068	−156%	−4,070	0.068	−118%	−3,965
−15%	0.072	−65%	2,516	0.072	−89%	2,422
−10%	0.077	−43%	4,070	0.077	−59%	8,808
−5%	0.081	−20%	5,696	0.081	−30%	15,195
Reference case	0.085	0%	7,142	0.085	0%	21,582
+5%	0.089	+20%	8,588	0.089	+30%	27,969
+10%	0.094	+43%	10,215	0.094	+59%	34,356
+15%	0.098	+65%	11,738	0.098	+89%	40,742
+20%	0.102	+86%	13,287	0.102	+118%	47,129

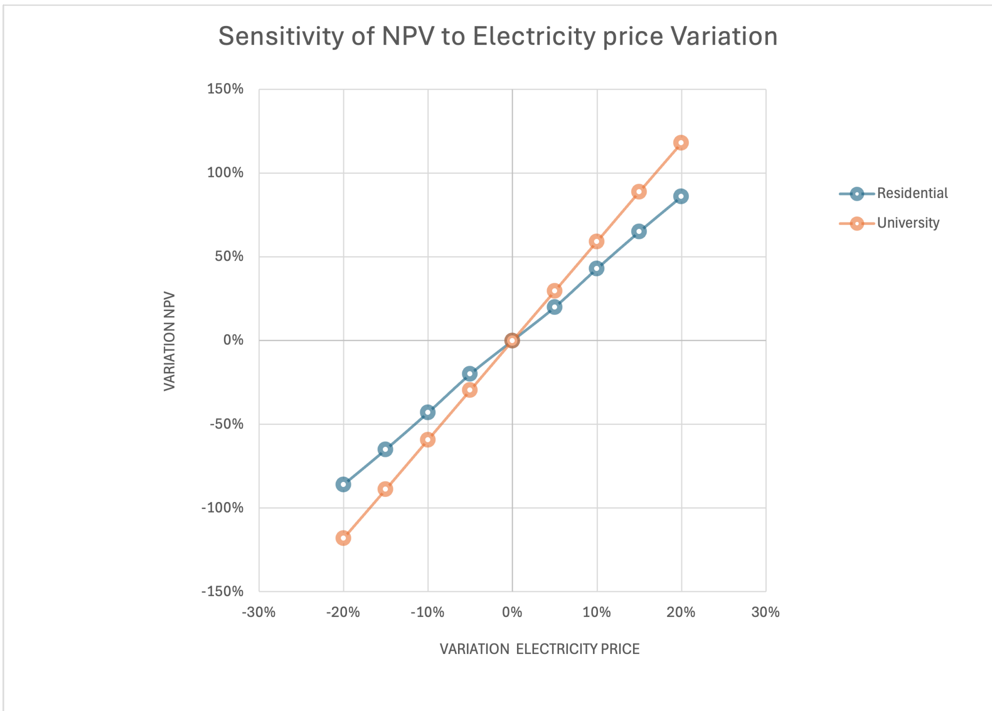

Figure 4.6: Sensitivity of the NPV to electricity price variations for the university and residential case studies.

Higher electricity prices increase NPV for both cases and lower prices reduce it. The university building shows a sensitivity of about ±118% for a ±20% price change, remaining positive across all upward scenarios and turning negative only at −20%. The residential system is comparatively more exposed on the downside, turning marginal already at −15% (about 2,516 €) despite its lower absolute investment. Both case studies therefore treat the assumed price of 0.085 € /kWh as close to a viability threshold, particularly for the residential installation, underlining the importance of conservative long-term price assumptions in BIPV feasibility studies.

4.6 Comparative Discussion

4.6.1 Comparison Between Case Studies

The two case studies differ substantially in building typology, system scale, integration strategy and economic performance, and their comparison provides useful insights into the applicability of BIPV systems across different contexts in the Finnish built environment.

From an energy perspective, both installations achieve a remarkably consistent specific energy yield of approximately 847–848 kWh /kWp/ year, confirming the coherence of the simulation framework across the two configurations. In both cases, annual electricity demand significantly exceeds BIPV production, resulting in a self-consumption ratio of 100% and no grid export, which maximises the economic value of the generated electricity.

From an economic perspective, the two installations exhibit complementary strengths, summarised in Table 4.13. The university building achieves the larger absolute NPV, driven substantially by the thermal savings from heat recovery (about 4,002 € /year), while the residential installation, despite its much smaller scale, achieves a higher IRR and a shorter payback time, reflecting its proportionally lower investment.

Table 4.13: Comparative economic results – university and residential case studies.

Parameter	University	Residential
Installed capacity [kWp]	150	28
CAPEX incl. VAT [€]	141,897	21,469
Annual OPEX [€ /year]	709	107
Specific energy yield [kWh /kWp/ year]	847	848
Self-consumption ratio [%]	100	100
Heat recovery included	Yes	No
NPV [€]	21,582	7,142
IRR [%]	9	10
DPBT [years]	21	19
LCOE [€ /kWh]	0.100	0.08

The sensitivity analysis confirms this trade-off (Section 4.5): the university system is more exposed to CAPEX and electricity price risk, while the residential system is financially more robust, at the cost of a smaller absolute economic benefit.

4.6.2 Comparison with Nordic Literature

The economic results obtained in this work can be contextualised against the Nordic BIPV literature. The most relevant benchmark is the Solsmaragden case study in Drammen, Norway [58], a commercial office building with a 127.5 kWp BIPV façade system at 59.74°N, comparable to the Helsinki location considered here (60.18°N).

The Solsmaragden system achieved a discounted payback time of 22 years and an IRR of 6% with Enova subsidies (exceeding 30 years without), and an LCOE of 1.28 NOK /kWh (approximately 0.11 € /kWh). By comparison, the university case study here achieves a payback time of 21 years, an IRR of 9%, and an LCOE of 0.100 € /kWh, without any subsidies. This more favourable outcome, despite the absence of incentives, reflects three factors: the use of commercially available TOPCon modules (about 26 € /m^2) rather than custom modules, the inclusion of heat recovery as an additional cash inflow not considered at Solsmaragden, and the higher efficiency of the Leapton modules (22.48%) compared to Solsmaragden's (16.6%).

These observations confirm that standard, commercially available modules and the combined electrical and thermal benefits of ventilated bifacial configurations can make

BIPV façade systems financially attractive in Nordic climates even without public incentives.

4.6.3 Role of Bifaciality and Heat Recovery

As shown in Section 4.3, the bifacial gain (368 € /year) is modest compared with the thermal energy savings from heat recovery (4,002 € /year), which is the dominant driver of the bifacial system's economic advantage under the conditions considered here: the primary economic value lies not in the electrical bifacial gain itself, but in the system-level benefit enabled by the ventilated air gap. This is consistent with the broader literature on ventilated BIPV façades [45, 47], which identifies cavity heat recovery as one of the main advantages of this configuration over flush-mounted alternatives.

4.6.4 Limitations and Future Directions

The techno-economic analysis presented in this chapter is subject to a number of simplifying assumptions and limitations that should be considered when interpreting the results.

First, a common CAPEX breakdown was adopted for both case studies, which does not fully reflect the different cost structures of a large façade-mounted installation and a small balcony-integrated system. In practice, substructure and installation costs are likely to differ significantly between the two configurations, and a project-specific cost estimation would be required for a more accurate economic assessment.

Second, the heat recovery assessment relies on several simplifying assumptions. The annual recoverable heat of 56.6 MWh /year is derived from CFD simulations for four representative seasonal benchmark days (Chapter 3), extrapolated from the three-panel CFD model to the full 300-module installation by linear scaling with the installed façade area. This assumes the thermal behaviour of each panel is independent of its position, a reasonable approximation given the uniform south orientation but potentially inaccurate under strong spatial gradients in irradiance or airflow. The scaling of Q_{rec} from peak-hour results to the full daily and seasonal profile uses the hourly irradiance profile as a proportionality factor, assuming that recovered thermal power scales linearly with incident irradiance: this is physically motivated, since cavity heat generation is primarily solar-driven, but it neglects non-linear effects such as variations in the convective regime and air temperature within the gap. The heating season is defined as October to April, when space heating is actively required in Finland [61]; other potential uses of the recovered heat (domestic hot water, ventilation air pre-heating) fall outside the present scope. The recovered heat is valorised at the district heating price of 101 € /MWh [61], the appropriate reference given district heating's dominant role in

Finnish space heating. Finally, since no dedicated heat recovery system is modelled or costed, the thermal savings should be interpreted as an upper bound on the recoverable benefit, subject to the efficiency and cost of the actual recovery system adopted.

Third, the analysis does not consider public subsidies or incentive schemes, which could substantially improve the economic indicators of both case studies, particularly for the university building where the sensitivity analysis shows that even a modest reduction in effective investment cost significantly improves the NPV and shortens the payback time. A comprehensive assessment of available Finnish incentive schemes is identified as an important direction for future work.

Fourth, the self-consumption ratio of 100% was assumed for both buildings based on the large gap between annual electricity demand and BIPV production. While well justified at the annual scale, hourly mismatches between production and consumption profiles may result in occasional grid export, particularly in summer months when solar production is highest and building demand may be lower. A detailed hourly simulation using measured load profiles would provide a more accurate representation of actual system operation.

Finally, the analysis does not account for potential revenues from grid services, demand response or energy sharing mechanisms, which may become increasingly relevant as the Finnish electricity market evolves towards greater decentralisation and prosumer participation. These aspects represent promising directions for extending the present techno-economic framework in future research.

Chapter 5

Conclusions

5.1 Restatement of the Research Problem

This work set out to address a specific gap identified in Chapter 1: bifacial photovoltaic technology and building-integrated façade systems have each been studied extensively, but their combination, a bifacial BIPV façade with a ventilated rear cavity operating under Nordic climatic conditions, has received comparatively little attention, and the optical, thermal and economic dimensions of such a system are rarely modelled within a single, consistent framework. The present thesis developed such a framework for a vertical, south-facing bifacial façade in Helsinki Kumpula (60.18°N), coupling three stages: an optical–electrical model quantifying the position-dependent rear-side irradiance and the resulting bifacial gain (Chapter 2); a conjugate heat-transfer CFD model resolving the buoyancy-driven airflow and the module temperature within the ventilated cavity (Chapter 3); and a techno-economic assessment translating these physical results into two realistic case studies (Chapter 4).The sections that follow are therefore not a chapter-by-chapter summary, but an account of how the three phases connect, and of the conclusions that only emerge from considering them together.

5.2 Central Finding: Heat Recovery, Not Bifaciality, Drives the Economic Value

Taken together, the three modelling stages point to a conclusion that is not stated explicitly in any single chapter: the economic case for this bifacial ventilated façade rests primarily on the ventilated cavity itself, not on the bifacial gain that motivated its inclusion. The optical model of Chapter 2 shows that the rear-side irradiance of a building-integrated bifacial module is dominated by wall reflection (88–96% of the total, depending on the month, Section 2.7.1), not by the open sky or ground view that a free-standing bifacial array would enjoy. This geometric constraint caps the electrical benefit of bifaciality at a modest level: the techno-economic analysis of Chapter 4 quantifies it at approximately 3.5%, corresponding to an additional saving of roughly

368 € per year at the reference electricity price (Section 4.6.3).

The same cavity that limits the bifacial gain, however, is also the source of a substantially larger economic benefit. Because the PV rear surface and the wall face each other across a narrow, buoyancy-driven air channel, the CFD model of Chapter 3 shows that a significant fraction of the absorbed solar power, approximately 27% of the total, is carried away as recoverable thermal energy rather than lost to the front-side convective and radiative exchange (Section 3.12.2). Once valorised at the Finnish district heating price, this recovered heat is worth approximately 4,002 € per year for the university case study (Section 4.6.3), an order of magnitude larger than the value of the bifacial gain itself.

This asymmetry reframes the role of bifaciality in the system as a whole. Bifacial modules are not, on their own, the source of the system's economic advantage; they are the component that makes a ventilated, wall-facing cavity architecturally sensible in a building-integrated context, since a monofacial module would derive no benefit whatsoever from facing a wall at close range. The value of the configuration studied in this thesis is therefore best understood as that of a thermal recovery system with a secondary electrical bifacial benefit, rather than the reverse. This reading is consistent with, and extends, the broader literature on ventilated BIPV façades, which identifies cavity heat recovery as a principal advantage of such systems over flush-mounted alternatives (Section 4.6.3), but it has not, to date, been stated explicitly for a bifacial configuration in a Nordic climate.

5.3 Consistency of the Modelling Chain: Why Gap Selection Required No Trade-off

A second point that only becomes visible across chapter boundaries concerns the internal consistency of the coupled optical-CFD framework, and specifically why the gap-width selection of Section 3.11.3 could be made on thermal grounds alone, without weighing it against an electrical penalty. The optical model of Chapter 2 already suggested this outcome, without stating it as a design conclusion: the annual mean module temperature is identical to within rounding across all three vertical positions on the façade (15.3°C, Table 2.6), indicating that T_{PV} is governed chiefly by the front-side energy balance rather than by the module's position relative to the cavity.

The CFD model confirms and sharpens this observation for the variable that matters most to the present design problem, the air-gap width. Across the full parametric matrix, the mean PV temperature varies by less than 1 K between the narrowest and the widest gap investigated (Table 3.17), even though the cavity airflow velocity and the convective coefficients change substantially over the same range (Section 3.12.1). The underlying mechanism, a solar-chimney flow whose velocity is strongly gap-dependent while the thermal load driving it is not, is what decouples the fluid-dynamic response from the electrical one (Section 3.12.1).

This decoupling is the reason the gap of 10 cm, selected in Section 3.11.3 purely on the basis of maximising heating-season thermal recovery, could be adopted without a compensating loss in temperature-dependent electrical efficiency (Equation (3.4)). Had T_{PV} instead varied strongly with gap width, as it does with front-side irradiance and ambient temperature, the thermal-recovery and electrical-efficiency criteria would have had to be traded off against one another, and the optimal gap would likely have differed from the one identified here. The consistency of the two criteria is therefore not a coincidence of the specific numbers obtained, but a direct consequence of where, physically, the module temperature is actually set.

5.4 Economic Viability in the Nordic Context

The two case studies of Chapter 4 demonstrate that the bifacial ventilated BIPV configuration is economically viable under realistic Finnish market conditions, without recourse to public subsidies. The university building achieves a positive NPV of 21,582 € over a 30-year horizon, an IRR of 9%, and a discounted payback time of 21 years; the residential installation, despite its considerably smaller scale, achieves a higher IRR of 10% and a shorter payback time of 19 years (Table 4.13). Both results compare favourably with the Solsmaragden reference case in Norway, a BIPV façade at a comparable latitude that required government incentives to reach a 22-year payback and a 6% IRR, and whose payback exceeds 30 years without them (Section 4.6.2). The comparison indicates that the combination of commercially available TOPCon modules, a higher module efficiency than the custom panels used at Solsmaragden, and the thermal recovery mechanism discussed in Section 5.2, is sufficient to make this class of system competitive on its own, incentive-free economic merits.

This viability is not, however, uniform across the two configurations. The sensitivity analysis of Section 4.5 shows that the university installation, with its larger absolute investment, is considerably more exposed to cost and price risk: its NPV turns negative for a CAPEX increase above 15% or an electricity price decline beyond 20%. The residential installation remains positive across the full range of CAPEX scenarios tested, and is comparably more resilient to downside risk, if not to electricity price risk. The two case studies therefore represent complementary rather than equivalent propositions: the university-scale façade offers the larger absolute economic benefit and the larger absolute contribution to building decarbonisation, while the smaller residential system offers the more robust, lower-risk investment profile. Neither result should be read as more broadly representative than the other; together, they indicate that the viability of the technology depends materially on system scale and on the buyer's tolerance for cost and price uncertainty, not solely on the underlying physics.

5.5 Cross-cutting Limitations

The individual limitations of each modelling stage are stated in detail within the corresponding chapters (Sections 2.8, 3.13 and 4.6.4) and are not repeated here. Three limitations, however, are structural to the framework as a whole rather than specific to any one stage, and are worth stating explicitly because they bound the interpretation of every result presented in this thesis.

First, none of the three models has been validated against experimental measurements for this specific façade configuration (Sections 2.8, 3.13). The optical, thermal and economic results should accordingly be read as an internally consistent, physically grounded theoretical assessment, not as a validated prediction of the as-built system's performance. The consistency checks performed within the CFD model (Section 3.8) establish numerical correctness, not experimental agreement, and the same caveat applies transitively to the economic results derived from it.

Second, the coupling between the three stages is one-way and sequential: the optical model supplies boundary conditions to the CFD model (Section 3.2), and the CFD model in turn supplies the recoverable heat estimate to the economic assessment (Section 4.6.4), with no feedback in either direction. An error or a simplifying assumption introduced at the optical stage, such as the constant, angle-independent optical properties noted in Section 2.8, therefore propagates unchanged through the thermal and economic results, without any downstream mechanism able to detect or correct it.

Third, the physical core of the analysis rests on steady-state, wind-free, two-dimensional simulations at five representative operating points (Sections 3.6.1, 3.13), rather than on a time-resolved annual simulation. Sub-hourly transients, three-dimensional edge effects, and wind-assisted ventilation are all outside the scope of the results obtained, and each could plausibly shift the optimal gap width identified in Section 3.11.3 in ways that the present framework cannot quantify.

5.6 Recommendations for Future Work

The three cross-cutting limitations of Section 5.5 suggest a corresponding set of priorities for future work, ordered by the extent to which they would strengthen the framework as a whole rather than a single stage of it.

The most consequential extension would be experimental validation, ideally through in-situ monitoring of module and cavity air temperatures on a real or pilot-scale ventilated bifacial façade, which would allow the optical and CFD models to be assessed against measured data rather than only against each other. Closing the one-way coupling between the optical and CFD stages, through an iterative scheme in which the CFD-resolved module temperature feeds back into the optical model's electrical output, would remove the propagation risk identified in Section 5.5 and is a natural next step given that the discrepancy it currently introduces has already been quantified (Section 3.9). Finally, extending the CFD analysis from steady-state representative operating points to a time-resolved annual simulation, and incorporating wind-assisted ventilation, would test whether the gap selection and the thermal-recovery estimate of Chapters 3 and 4 hold under the full range of transient and wind conditions experienced by a real Nordic façade over a full year.

Beyond these three priorities, the techno-economic assessment of Chapter 4 would benefit from project-specific CAPEX estimation in place of the common cost breakdown adopted for both case studies, and from an evaluation of applicable Finnish incentive schemes, both identified in Section 4.6.4 as directions that were outside the scope of the present work. Taken together, this thesis establishes that a bifacial ventilated BIPV façade is both technically coherent and economically viable in a Nordic climate, driven principally by cavity heat recovery rather than by bifaciality itself; the priorities outlined here are the steps required to move that conclusion from a theoretical, internally consistent result to one grounded in measured performance.

Bibliography

[1] Jianmei Zhong, Wei Zhang, Lingzhi Xie, Oufan Zhao, Xin Wu, Xiding Zeng, and Jiahong Guo. Development and challenges of bifacial photovoltaic technology and application in buildings: A review. *Renewable and Sustainable Energy Reviews*, 187:113706, 2023.

[2] International Energy Agency. World Energy Outlook 2024. Technical report, IEA, 2024. Used for: net-zero 2050 scenario, global energy transition context, solar PV manufacturing capacity.

[3] International Energy Agency. Renewables 2024 – Analysis and Forecast to 2030. Technical report, IEA, 2024. Used for: global renewable capacity growth (2.7x by 2030), 430 GW solar PV added in 2023, distributed PV applications = 40% of expansion to 2030.

[4] International Energy Agency. Energy Efficiency 2025 – Buildings. Technical report, IEA, 2025. Used for: buildings = 30% of global final energy consumption, 20% of demand growth since 2019.

[5] International Energy Agency. Global Energy Review 2025. Technical report, IEA, 2025. Used for: solar PV = 7% of global electricity in 2024 (up from 5.4% in 2023), renewables = 32% of world electricity for first time in 2024.

[6] International Energy Agency. Solar PV – IEA Energy System. Technical report, IEA, 2024. Used for: 50% module price drop 2022–2023, NZE scenario requires 28% annual generation growth to reach 9200 TWh by 2030.

[7] European Parliament and Council of the European Union. Directive (EU) 2024/1275 on the Energy Performance of Buildings (recast) – EPBD. Technical report, Official Journal of the European Union, 2024. Used for: zero-emission buildings as new standard, solar-ready requirement for all new buildings, mandatory solar installation deadlines 2026–2029, 16% primary energy reduction target by 2030.

[8] International Renewable Energy Agency. Renewable Power Generation Costs in 2023. Technical report, IRENA, Abu Dhabi, 2024. Used for: solar PV costs fell 85–90% since 2010, now cheapest new electricity source in most countries.

[9] REN21. Renewables 2024 Global Status Report. Technical report, REN21 Secretariat, Paris, 2024. Used for: buildings = 31% of total final energy consumption globally, renewables = 17.7% of buildings energy consumption in 2024.

[10] Liga Zemite et al. The role of renewable energy and storage technologies in sustainable development: simulation in the construction industry. *Frontiers in Energy Research*, 2025. Used for: EU buildings = 40% of energy consumption and 35% of GHG emissions; Green Deal target of -55% emissions by 2030.

[11] United Nations Department of Economic and Social Affairs. World Urbanization Prospects 2018 – Highlights. Technical report, United Nations, 2019. Used for: 56% urban population in 2023, projected 68% by 2050 – urban constraints for land availability.

[12] Zhe Yu, Cuiying Chen, Duo Lou, Jingjing Jiang, and Bin Ye. Energy-economy-environment evaluation of building-integrated photovoltaic considering facade factors for representative megacities in China. *Applied Energy*, 389:125839, 2025. Used for: 3E evaluation of BIPV facade systems; energy, economic and environmental performance.

[13] Silvana Ayala Peláez. Bifacial solar modules system design, modeling, and performance, 2019.

[14] N.R. Avezova, N.A. Matchanov, A.A. Kuchkarov, and A.A. Abduraimov. Bifacial photovoltaic systems: current state of research, modelling, efficiency and development prospects. *Science and Innovation*, 4(9):52–66, 2025. Used for: bifacial PV market share reaching 85% by 2032, 5–20% energy gain vs monofacial, BIPV applications, snow albedo effects at high latitudes, vertical orientation advantages, view factor method overestimates rear irradiance by 6.7%.

[15] M.R. Khan, A. Hanna, X. Sun, and M.A. Alam. Vertical bifacial solar farms: Physics, design, and global optimization. *Applied Energy*, 206:240–248, 2017. Used for: physics of vertical bifacial systems, global optimization at different latitudes, advantages of vertical orientation at high latitudes (>50 N).

[16] S. Wang, O. Wilkie, J. Lam, R. Steeman, W. Zhang, K.S. Khoo, and H. Rostan. Bifacial photovoltaic systems energy yield modelling. *Energy Procedia*, 77:428–433, 2015. Used for: energy yield model for bifacial systems, field validation, installation height effects on rear-side irradiance.

[17] PV Performance Modeling Collaborative. View Factor Models for Bifacial PV Systems. Sandia National Laboratories, 2022. Used for: view factor formula F = 0.5*(1-cos(theta)), Lambertian reflection assumption (A5).

[18] W.F. Holmgren, C.W. Hansen, and M.A. Mikofski. pvlib python: a python package for modeling solar energy systems. *Journal of Open Source Software*, 3(29):884, 2018. Used for: solar position calculation using Reda & Andreas (2004) algorithm, Perez irradiance transposition model for non-horizontal surfaces.

[19] G.M. Tina, F. Bontempo Scavo, S. Aneli, and A. Gagliano. Assessment of the electrical and thermal performances of building integrated bifacial photovoltaic modules. *Journal of Cleaner Production*, 313:127906, 2021. PRIMARY REFERENCE for the modelling framework. Used for: G_wall (Eq.9), G_rear (Eq.10), T_pv thermal-equilibrium model (Eq.15), efficiency-temperature correction (Eq.11), bifacial power P_bif (Eq.13), and heat-loss coefficients U0=25, U1=1.2 (Table 5). NOTE: module optical/electrical parameters (PF, BF, eta_STC, beta0) are NOT taken from Tina but from the Leapton LP182-54 datasheet.

[20] William H. McAdams. *Heat Transmission*. McGraw-Hill, New York, 3rd edition, 1954.

[21] B. Marion, S. MacAlpine, C. Deline, et al. A Practical Irradiance Model for Bifacial PV Modules. 2017. Used for: justification of infinite facade assumption (A1), single-reflection assumption (A6) in view factor models for bifacial PV systems.

[22] D. Faiman. Assessing the outdoor operating temperature of photovoltaic modules. *Progress in Photovoltaics: Research and Applications*, 16(4):307–315, 2008. Used for: original derivation of panel temperature model T_pv = T_air + G/(U0 + U1*v), later adopted by Tina et al. (2021).

[23] Rafaela A. Agathokleous and Soteris A. Kalogirou. Status, barriers and perspectives of building integrated photovoltaic systems. *Energy*, 191:116471, 2020. Used for: BIPV definition and distinction from BAPV, first BIPV installation (Aachen 1991), main barriers (cost up to 20% higher, feed-in tariff, public acceptance), material substitution cost offset, future perspectives.

[24] M. Constantinou et al. A review on technological and urban sustainability perspectives of advanced building-integrated photovoltaics. *Energy Science & Engineering*, 11, 2023. Used for: BIPV = only 1% of total global PV installations, barriers classification (technical, economic, social, policy), thermal management challenges, aesthetic integration.

[25] Zhan Shu et al. Scientometric analysis of building integrated photovoltaics research: development, themes and main trends. *Journal of Asian Architecture and Building Engineering*, 2024. Used for: analysis of 467 BIPV studies 2019–2023, key research themes, architects knowledge gap, need for dedicated BIPV design software.

[26] Erika Saretta et al. BIPV market development: International technological innovation system analysis. *Buildings*, 15(17):3011, 2025. Used for: BIPV dual nature as PV and building product, cost as primary barrier in all 6 countries studied, lack of standards and cross-sector collaboration, BAPV preferred over BIPV due to lower upfront cost.

[27] Grand View Research. Building-integrated photovoltaics market size, share & trends analysis report, 2024. Used for: global BIPV market USD 23.67 billion in 2023, projected USD 89.8 billion by 2030 at CAGR 21.2%, roof segment = 66.9% of market, Europe = 37.1% revenue share.

[28] Rafaela A. Agathokleous and Soteris A. Kalogirou. Double skin facades (DSF) and building integrated photovoltaics (BIPV): A review of configurations and heat transfer characteristics. *Renewable Energy*, 89:743–756, 2016. Used for: ventilated facade air cavity cooling effect, DSF+BIPV configurations, heat transfer characteristics, passive cooling and pre-heating potential.

[29] Carlos D. Rodríguez-Gallegos et al. Monofacial vs bifacial si-based pv modules: Which one is more cost-effective? *Solar Energy*, 176:412–438, 2018.

[30] Thorsten Dullweber, Christopher Kranz, Robby Peibst, Ulrike Baumann, Helge Hannebauer, Alexander Fülle, Stefan Steckemetz, Torsten Weber, Martin Kutzer, and Matthias Müller. Perc+: industrial perc solar cells with rear al grid enabling bifaciality and reduced al paste consumption. *Progress in Photovoltaics: Research and Applications*, 24(12):1487–1498, 2016.

[31] E. Lohmüller, S. Werner, M. H. Norouzi, S. Gutscher, M. Demant, P. Saint-Cast, M. Linse, B. Bitnar, P. Palinginis, H. Neuhaus, and A. Wolf. Low-ohmic contacting of laser-doped p-type silicon surfaces with pure ag screen-printed and fired contacts. *physica status solidi (a)*, 214:1700587, 2017.

[32] W. Cai, S. Yuan, Y. Sheng, W. Duan, Z. Wang, Y. Chen, Y. Yang, P. P. Altermatt, P. J. Verlinden, and Z. Feng. 22.2% efficiency n-type pert solar cell. *Energy Procedia*, 92:399–403, 2016.

[33] Q. Wei, S. Zhang, S. Yu, J. Lu, W. Lian, and Z. Ni. High efficiency n-pert solar cells by b/p co-diffusion method. *Energy Procedia*, 124:700–705, 2017.

[34] A. Stassen, M. König, N. Bay, H. Kühnlein, C. Schmitt, A. H. G. Vlooswijk, P. R. Venema, Y. Zhang-Steenwinkel, K. C. J. J. Tool, D. S. Saynova, M. W. P. E. Lamers, E. J. Kossen, M. Koppes, Y. Komatsu, A. Gutjahr, P. Barton, J. Anker, B. B. Van Aken, and I. G. Romijn. Industrial cost effective n-pasha solar cells with >20% cell efficiency. In *Proceedings of the 28th European Photovoltaic Solar Energy Conference and Exhibition*, pages 736–740, 2013.

[35] G. Galbiati, H. Chu, V. D. Mihailetchi, J. Libal, and R. Kopecek. Presented at the world conference on photovoltaic energy conversion (wcpec-7), 2018. Conference presentation.

[36] V. D. Mihailetchi, A. Halm, C. Comparotto, S. Aulehla, and R. Kopecek. Presented at the 2nd bifi pv workshop, 2014. Workshop presentation.

[37] M. Taguchi, A. Yano, S. Tohoda, K. Matsuyama, Y. Nakamura, T. Nishiwaki, K. Fujita, and E. Maruyama. High-efficiency hit solar cell on thin silicon wafer. *IEEE Journal of Photovoltaics*, 4(1):96–99, 2014.

[38] I. G. Romijn. Presented at the 4th bifi pv workshop, 2017. Workshop presentation.

[39] M. A. Green, E. D. Dunlop, J. Hohl-Ebinger, M. Yoshita, N. Kopidakis, and A. W. Ho-Baillie. Solar cell efficiency tables (version 55). *Progress in Photovoltaics: Research and Applications*, 28(1):3–15, 2020.

[40] Shin Min Jeong, Sungeun Park, and Ahreum Lee. bpv performance of semitransparent ultrathin cu(in,ga)se2 solar cells with front and rear transparent conducting oxide contacts. *Applied Surface Science*, 535:147732, 2021.

[41] Chris Deline et al. Bifacial pv system performance: Separating fact from fiction. Technical report, NREL, 2019.

[42] Robert Siegel and John R. Howell. *Thermal Radiation Heat Transfer*. Taylor & Francis, 4th edition, 2002.

[43] National Renewable Energy Laboratory. Bifacial radiance, 2018.

[44] Greg Ward. The radiance lighting simulation and rendering system. In *Proceedings of the 21st Annual Conference on Computer Graphics and Interactive Techniques (SIGGRAPH '94)*, pages 459–472. ACM, 1994.

[45] R. A. Agathokleous and S. A. Kalogirou. Double skin facades (dsf) and building integrated photovoltaics (bipv): A review of configurations and heat transfer characteristics. *Renewable Energy*, 89:743–756, 2016.

[46] P. Nahani, M. Eslami, and R. Hamzehzarghani. Effects of wind on cooling and performance of photovoltaic arrays: A case study cfd modeling. *Energy*, 293:130596, 2024.

[47] Guohui Gan. Effect of air gap on the performance of building-integrated photovoltaics. *Energy*, 34(7):913–921, 2009.

[48] Guohui Gan. Numerical determination of adequate air gaps for building-integrated photovoltaics. *Solar Energy*, 83(8):1253–1273, 2009.

[49] Mattia Manni, Jacowb Krum Thorning, Sami Jouttijärvi, Kati Miettunen, Marisa Di Sabatino, and Gabriele Lobaccaro. Horizontal-to-tilt irradiance conversion for high-latitude regions: a review and meta-analysis. *Frontiers in Built Environment*, 9:1245223, 2023.

[50] Sami Jouttijärvi et al. Benefits of bifacial solar cells combined with vertical installation at high latitudes. *Renewable and Sustainable Energy Reviews*, 161:112324, 2022.

[51] M. Formolli, T. Kleiven, and G. Lobaccaro. Assessing solar energy accessibility at high latitudes: A systematic review of urban spatial domains, metrics, and parameters. *Renewable and Sustainable Energy Reviews*, 177:113231, 2023.

[52] M. R. Khan, Y. Hanna, J. Sun, R. Alam, et al. Vertical bifacial solar farms: physics, design, and global optimization. *Applied Energy*, 206:240–248, 2017.

[53] Erik Molin, Bengt Stridh, Annica Molin, and Ewa Wäckelgård. Experimental yield study of bifacial pv modules in nordic conditions. *IEEE Journal of Photovoltaics*, 8(6):1457–1463, 2018.

[54] Sami Jouttijärvi, Magda Szarek, Bergpob Viriyaroj, and Kati Miettunen. Solar energy for multi-story apartment buildings – innovative façade solutions and energy sharing enable load-matching. *Energy and Buildings*, 360:117382, 2026.

[55] Eurostat. Eurostat database, 2026.

[56] Shreeyashi Ojha. Premium pv module prices rise again in europe despite softer april demand signals, May 2026.

[57] Sun.store. Pv index – may 2026, may 2026.

[58] Hassan Gholami, Harald Nils Røstvik, Nallapaneni Manoj Kumar, and Shauhrat S. Chopra. Lifecycle cost analysis (lcca) of tailor-made building integrated photovoltaics (bipv) façade: Solsmaragden case study in norway. *Solar Energy*, 211:488–502, 2020.

[59] Paolo Corti, Alberto Follo, and Pierluigi Bonomo. Workflow to support cost-benefits comparison and sensitivity analysis of bipv case studies: Three examples of bipv facades in the south of switzerland. *Energy and Buildings*, 322:114732, 2024.

[60] Qi Xu, Saffa Riffat, and Shihao Zhang. Review of heat recovery technologies for building applications. *Energies*, 12(7):1285, 2019.

[61] Finnish Energy. District heating in finland 2023, 2024. Statistical graphs and presentation.

[62] Vaasan Sähkö. Electricity consumption at your home – what does it consist of?, 2025.

[63] Niina Leskinen, Jussi Vimpari, and Seppo Junnila. Using real estate market fundamentals to determine the correct discount rate for decentralised energy investments. *Sustainable Cities and Society*, 53:101953, 2020.

[64] Alessio Passera, Roberto Lollini, Stefano Avesani, Marco Lovati, Luca Maturi, and David Moser. Bipv facades: Market potential of retrofit application in the european building stock. In *35th European Photovoltaic Solar Energy Conference and Exhibition (EU PVSEC 2018)*, pages 2113–2118, 2018.

[65] Changying Xiang and Barbara Szybinska Matusiak. Façade integrated photovoltaics design for high-rise buildings with balconies, balancing daylight, aesthetic and energy productivity performance. *Journal of Building Engineering*, 57:104950, 2022.

[66] Finnish Meteorological Institute. The finnish meteorological institute's open data. https://en.ilmatieteenlaitos.fi/open-data, 2026.

[67] Leapton Energy Co., Ltd. *LP182*210-M-54-NB N-Type TOPCon Dual Glass PV Module Datasheet*. Leapton Energy Co., Ltd., 2024. Version 2.

[68] Frank P. Incropera, David P. DeWitt, Theodore L. Bergman, and Adrienne S. Lavine. *Fundamentals of Heat and Mass Transfer*. John Wiley & Sons, 6 edition, 2007.

[69] Ministry of the Environment, Finland. Decree of the Ministry of the Environment on the Energy Performance of New Buildings, 2017. Unofficial English translation. Entered into force on 1 January 2018.

[70] Copernicus Climate Change Service. ERA5 hourly data on single levels from 1940 to present, 2026. Copernicus Climate Data Store.

[71] Yusuf Can Demir and Mehmet Azmi Aktacir. Experimental investigation of the bipv system under şanliurfa meteorological conditions. *Applied Sciences*, 13(20):11286, 2023.

[72] W. C. Swinbank. Long-wave radiation from clear skies. *Quarterly Journal of the Royal Meteorological Society*, 89(381):339–348, 1963.

[73] V. Yakhot and S. A. Orszag. Renormalization group analysis of turbulence: I. basic theory. *Journal of Scientific Computing*, 1(1):1–51, 1986.

[74] D. Roeleveld et al. A cfd study of natural convection inside a bipv/t system. In *Proceedings of eSim 2016 Conference*, 2016.